Vrije Universiteit Brussel

Faculty of Engineering Sciences
Department of Electronics and Informatics

Spectral ageing model for the Meteosat First Generation visible band

PhD. thesis submitted in partial fulfillment of the requirements for the degree of Doctor in Engineering Sciences

Ilse Decoster

Promotors:	Prof. J. Cornelis Dr. N. Clerbaux (RMIB)
Examining committee:	Prof. L. Van Biesen Prof. R. Pintelon Prof. H. Sahli Dr. J. Chan Dr. R. Stöckli (MeteoSwiss – Switzerland) Dr. Y. Govaerts (Govaerts Consulting)

January 27, 2014

You, my readers or hearers of my lectures, if you think I have done as much as can fairly be expected of an initial start... will acknowledge what I have achieved and will pardon what I have left for others to accomplish.

Aristotle (384–322 BC)

―

Acknowledgments

Here we are. *Another turning point* in life, another *fork stuck in the road*, and time to recollect the memories of the last time that happened and what it brought to me. A little over 4.5 years ago, a decision had to be made: to do a PhD or not to do a PhD. It was not a difficult question. Before I realised, *time had grabbed me by the wrist* and *directed me where to go.* KMI was the place to be while I made my first steps in the real world. When I look back, making a PhD has not only been about the subject I was working on. These past years have been a learning process, a gentle (and at the end somewhat less gentle) way of preparing me to stand on my own feet, learn to use what's between my ears, and do it with a healthy amount of criticism. I tried to *make the best of this test.* And even though it was hard at times, and at the end I wondered why I was doing this to myself, deep down I knew, I *shouldn't ask why.* Because in fact, *it's not even a question* I was allowed to ask, I knew it was *a lesson learned in time.*

Throughout the years, whenever I got stuck, whenever I had a question or didn't know which direction to choose, Nicolas was there to provide me with even more ideas. He had a very clear roadmap in mind, and he managed to guide me through it until the very end. Thank you for having been an amazing supervisor. I also want to thank my promotor, Jan. Even though I might not have bothered you as often as you would have wanted me to, I hope part of you realised that I was in good hands with Nicolas and that things would turn out fine. Thanks for the trust you gave me in wanting to be my promotor, and for reading my thesis on such short notice. You sent me e-mails with corrections at the latest possible hours of the day, which filled me with a lot of gratitude. Thank you also for helping me reach the finish line perfectly in time when I started to fear I wouldn't make it before the end of the year. The third person I want to thank is someone who has helped me through all of the administration at the VUB in these past years, and especially now in these past weeks. Karin, you made life so much simpler for us, KMI PhD-"students", you are a real gift from heaven. I would also like to thank the members of my jury: Prof. Leo Van Biesen, Prof. Rik Pintelon, Prof. Hichem

Sahli, Dr. Jonathan Chan, Dr. Reto Stöckli and Dr. Yves Govaerts. Thank you for having been a kind jury, for the constructive comments, and for the support.

Life at KMI would not have been so pleasant without all the colleagues. Bert, my emotional support at work. Pieter-Jan, an amazing office mate who understood where I was headed. Edward, who helped me get rid of yet another segmentation fault in one of my programs. Stijn, my travel buddy all the way into the Rocky Mountains, from both East and West sides. Almudena, my listening ear throughout the years. Alessandro, who never minded to read yet another paper or yet another part of my thesis. Justine, providing me with the most welcome relaxing times in the sauna. Els, Lesley, Rozemien en Sepideh, who helped me get some girl power back at the lunch table. Patrick, who realised how important peace of mind was for my physical welfare. And Annette, who makes life so much easier for us at KMI by knowing exactly where to direct us with this or that work issue, but who has also always believed that things would turn out well for me. I would also like to thank all the foreign colleagues who provided me with information, discussions and new ideas during one of the many meetings (CM SAF, GERB, CERES) and conferences (EUMETSAT, WCRP).

When I started out my PhD, I was part of the first group of Master in Astronomy & Astrophysics graduates from KU Leuven. We were only a small group, but we managed to stay in touch and we had some really good times together, both during the Master education and after. Robin, Steven, Michel, Nadia, Peter, Pieter Neyskens, Jona, and Pieter Gruyters, thank you for the many cosy late nights at the institute, for the amazing two years of studying and laughing, for the holidays some of us spent together, for the many drinks and lots of fun. And when I think back to the friends from university that stayed with me all these years, then Greet is the first person that comes to mind. We met during the first week of our first year in Leuven and managed to stay close friends all this time. Thank you for your eternal support, listening ear, and for your amazing taste in movies and television series! I continue along the same trend by showing my gratitude for another amazing friend. Robin, we went through a lot together, traveling through different parts of the world, sharing thoughts, hopes and dreams. Thank you for trusting me, believing in me, and never giving up on me.

Another group of friends I want to mention, are the people from the VUBorkest. For four years in a row, I have had the honor of being part of this hug-loving orchestra. Thank you for all the love, the joy, and the amazing weekends filled with music, games and talks. Thank you also for "allowing" me to skip one year so that I could fully concentrate on finishing this PhD. In this orchestra I also met Euridike, a girl who has been a very close friend these past years, who was next to me while I went through ups and downs, who, at times, was thought to be my sister, and at other times even me. Girl, here’s to many more years to come.

Thank you also to the support team from my home "town". Particularly, Lisa, Chara en Sarah, the girls from high school with whom I went to KU Leuven. Also, to all the people from the fanfare who were always interested to hear how things were evolving. Wendy, you too have been a positive vibe throughout these years. Even though we lost sight of each other during our years at university, we found each other again and picked up where we left off as if we never missed a day.

Mama and papa, thank you for your love, for the warm and comforting home, for the way you let us find our own way in life while at the same time letting us know that we can always count on you. Kristof and Stefan, thank you for being the best two big brothers that I could have imagined, and for being an example I look up to. Tatiana and Ine, thank you for being the best two beautiful sisters my brothers could have picked out, and thank you for having given me an amazing and adorable niece, nephew and god child. Celine, you are a ray of sunshine in my life, you make me want to be a better person. En oma, dankjewel voor de steun die je me gegeven hebt. Ik weet dat je bezorgd geweest bent omdat ik het de laatste maanden zo druk gehad heb, dat je met me meegeleefd hebt naar het einde toe, en dat je nu waarschijnlijk even blij (of misschien nog blijer) bent dan ik dat ik er geraakt ben zonder kleerscheuren. Danku daarvoor.

And how can I not end with the most special thing that has happened to me during this PhD: finding this amazing guy, who has not only given me so much love and happiness, but who also carried me when I thought I couldn't go anymore, who listened when I couldn't hear myself think anymore and who is my eternal source of peace and tranquility in life. I love you, so much more than I can ever tell you..

Ilse

It's something unpredictable, but in the end it's right
I really have had the time of my life

Glossary

Acronyms

ADC Atlantic Ocean data coverage.
ADM angular distribution model.
AOD aerosol optical depth.
ASTER Advanced Spaceborne Thermal Emission and Reflection Radiometer.
AU Astronomical Unit.
AVHRR Advanced Very High Resolution Radiometer.

CALIPSO Cloud-Aerosol Lidar and Infrared Pathfinder Satellite Observation.
CDOP-2 Second Continuous Development and Operations Phase.
CERES Clouds and Earth's Radiant Energy System.
CM SAF Climate Monitoring Satellite Application Facility.
COD cloud optical depth.
CPP cloud physical properties.

DC digital count.
DCP Data Collection Platform.
DCS Data Collection System.
DISORT Discrete Ordinates Radiative Transfer.
DWD Deutscher Wetterdienst.

ECV essential climate variable.
ENVISAT Environmental Satellite.
ERB Earth radiation budget.
ERBE Earth Radiation Budget Experiment.
ERBS Earth Radiation Budget Satellite.
ESA European Space Agency.
EUMETSAT European Organization for the Exploitation of Meteorological Satellites.

FCDR fundamental climate data record.
FOV field–of–view.
FSI filtered solar irradiance.

GACP Global Aerosol Climatology Project.
GCOM-W1 Global Change Observation Mission-Water.
GCOS Global Climate Observing System.
GEO geostationary orbit.
GERB Geostationary Earth Radiation Budget.
GIP GCOS Implementation Plan.
GISS Goddard Institute of Space Studies.
GMS Geostationary Meteorological Satellite.
GOES Geostationary Operational Environmental Satellites.
GOME Global Ozone Monitoring Experiment.
GSICS Global Space-based Intercalibration System.

HIRS High Resolution Infrared Sounder.
HRV high resolution visible.

IASI Infrared Atmospheric Sounding Interferometer.
IGBP International Geosphere / Biosphere Programme.
INDOEX Indian Ocean Experiment.
IODC Indian Ocean data coverage.
IR infrared.
ITCZ InterTropical Convergence Zone.

LDA Land Daily Aerosol.
LEO low-Earth orbit.
LUT look-up table.
LW longwave.

MAP Mesoscale Alpine Programme.
MERIS Medium Resolution Imaging Spectrometer.
MFG Meteosat First Generation.
MODIS Moderate Resolution Imaging Spectro-radiometer.
MOP Meteosat Operational Programme.
MSG Meteosat Second Generation.
MTP Meteosat Transition Programme.
MVIRI Meteosat Visible and Infrared Imager.

NASA National Aeronautics and Space Administration.
NB–to–BB narrowband–to–broadband.
NOAA National Oceanic and Atmospheric Administration.

PARASOL Polarization & Anisotropy of Reflectances for Atmospheric Sciences coupled with Observations from a Lidar.

RMIB Royal Meteorological Institute of Belgium.
RMS root mean square.
RSS Rapid Scanning Service.
RTM radiative transfer model.

SBDART Santa Barbara DISORT Atmospheric Radiative Transfer.
ScaRaB Scanner for Radiation Budget.
Sciamachy SCanning Imaging Absorption spectrometer for Atmospheric CHartographY.
SeaWiFS Sea-viewing Wide Field–of–view Sensor.
SEVIRI Spinning Enhanced Visible and Infrared Imager.
SGA sun glint angle.
SR spectral response.
SSCC SEVIRI Solar Channel Calibration.
SUVI Solar Ultraviolet Imager.
SW shortwave.

TCDR thematic climate data record.
TOA top of the atmosphere.
TOT total.
TRMM Tropical Rainfall Measuring Mission.

UNFCC United Nations Framework Convention on Climate Change.
UTC Universal Time Convention.
UV ultraviolet.

VIS visible.

WMO World Meteorological Organization.
WV water vapour.

X-ADC Extended ADC.

Contents

Introduction

Aristotle was the first to come up with the word "meteorology". In his time (384 – 322 BC), the term covered *"all the affections we may call common to air and water, and the kinds and parts of the Earth and the affections of its parts"* (Aristotle 350 BC). Over the centuries, meteorology became more specifically the study of the weather, of what happens to the atmosphere at any given time. Early climatologists started to recognize historical climate changes in the remnants of past glacial activity, in layers of clay laid down in lake beds and in tree rings. Already at the end of the nineteenth century, the positive feedback effect of CO_2 was discovered (Murat et al. 2008). With increasingly better and more measurements of the radiation from the Earth and the Sun, and of the amount and type of molecules present in the atmosphere, the importance of studying the current climate became obvious. In the second half of the 20th century, climatology was separated from meteorology and became an atmospheric science on its own: the study of the climate, of what the statistics say will happen to the atmosphere at any given time.

Since several decades, the topic of global climate change has caught the attention of policy makers, and is now an important agenda point for governments all over the world. In order to give advice on how the climate will evolve, scientists try to understand why and how it changes by taking measurements of all the processes which play an important role in the Earth's climate. For these studies, long-term data records of at least 25 – 30 years are generated using data from both ground stations, air borne instruments, and space based satellites. The latter become more and more useful due to the fact that instruments in space are able to make continuous observations on a more global scale than ground or air borne instruments.

When creating climatological time series from satellite instruments alone, often, data from several consecutive instruments need to be combined to reach the necessary time length for these studies. At this point, it is important that consistency is maintained in order to compare the output from one satellite to another.

Part of this is accomplished using a consistent calibration over the different instruments. For a lot of satellites, however, degradation processes take place while they are in space, diminishing the quality of the data (and hence the calibration) by decreasing the sensor sensitivity in time. If scientists want to use these specific satellites for long-term climate datasets, corrections need to be made for the degradation.

This study focusses on the ageing process of the imagers on board of the first Meteosat series. Since more than 30 years, the Meteosat satellites of the European Organization for the Exploitation of Meteorological Satellites (EUMETSAT) have been measuring the thermal emitted and visible reflected outgoing radiation of the Earth. Due to their long time period in space, the data from these instruments is very useful for climatological data records, especially because they provide half hourly measurements, allowing to address the full diurnal cycle. However, since the beginning, degradation of the visible (VIS) channel of the imager onboard these satellites, has been causing a decrease in signal in time. At the moment, EUMETSAT proposes a calibration method, which corrects the degradation by letting the calibration coefficient increase in time at the same rate as the signal decreases. Validation of this method has shown, however, that this correction is not perfect, as there is a spectral effect in the degradation, letting the radiation reflected over ocean decrease more rapidly than the radiation reflected over desert. In this work, a semi-empirical model is proposed to correct the VIS images of the first generation of Meteosat satellites (1982 – 2006) for this in-flight spectral degradation. The normalised SR curve, which shows the percentage of incoming radiation that is observed at each wavelength, is modeled in time and wavelength, allowing a stronger degradation rate for the smaller visible wavelengths than for the longer ones.

Chapter 1 gives an overview of the use of meteorological satellites for climate research, focussing in more detail on the Meteosat series. The main topic of this thesis, i.e. the calibration and degradation of the VIS channel of the Meteosat First Generation (MFG) instruments is discussed, together with the reason why this work has been performed. Chapter 2 starts by explaining how the model is able to correct the VIS images. Only specific data is used to find the satellite dependent model parameters, and so the data selection and treatment is also added in Chapter 2. In Chapter 3, the mathematical formula and history of the semi-empirical degradation model is presented, while in Chapter 4, the model is applied to Meteosat-7, the last and most recent of the MFG satellites. Also, in this chapter, the degradation model is compared to the currently official degradation model of EUMETSAT in a theoretical way, based on five important climatological variables. After that, the degradation model from this work is applied, in Chapter 5, to the rest of the MFG satellites. In Chapter 6, a side-track is taken, where the correctness of the Meteosat-7 SR curve at launch is investigated. The work is concluded in Chapter 7, showing some of the future prospects of this thesis work.

Chapter One

Meteorological satellites in support of climate research

This chapter situates the work carried out within the observational part of climatology. In the first section, the necessary scientific background information is given. The three components that make up the Earth radiation budget (ERB) are introduced: the incoming solar radiation, the outgoing reflected visible radiation and the outgoing emitted thermal radiation. An imbalance between the total incoming and outgoing radiation, can lead to climate changes. After that, some radiation definitions are presented, which will be useful later on in this thesis, and a summary is given of contemporary and historical climate research. The second section discusses meteorological satellites in space, used for climatological research. The two most important orbits are briefly discussed, putting most emphasis on the geostationary orbit which is used by the Meteosat satellites. The instruments onboard of the first and second generation of these satellites are discussed next, together with a history of all the Meteosat instruments that have been and are still in space. The final section introduces the exact topic of this thesis, i.e. the calibration and degradation of the Meteosat First Generation (MFG) visible (VIS) channel, summarising studies that have already been performed previously, and explaining the necessity of the work described in the remainder.

1.1 SCIENTIFIC BACKGROUND

1.1.1 RADIATION AND EARTH SYSTEM

When the Earth is in a perfect state of radiative equilibrium, the same amount of radiation comes into the Earth system at the top of the atmosphere (TOA) as the amount that goes out of it, and there is, per definition, no radiative forcing.

In this equilibrium state, the incoming and outgoing energy of the Earth are in balance. The dominant source of incoming radiation is the Sun. Part of its radiation is absorbed by the Earth's surface and atmosphere and re-emitted as thermal radiation, and part is reflected back into space. These three radiation types (incoming solar radiation, outgoing emitted radiation, and outgoing reflected radiation) can be measured separately, and together they make up the ERB. Any difference between the incoming and total outgoing radiation, causes an energy imbalance, and can have effects on the whole Earth system. For example, the Earth surface temperature might increase when more radiation comes into the system than goes out of it (i.e. a positive radiative forcing), or decrease when more radiation leaves the system than comes in (i.e. a negative radiative forcing), it can melt the ice caps at the North Pole or in the other case even increase the amount of ocean ice, etc. The three components that balance the ERB are discussed in a bit more detail now.

Three ERB components

Every body with a temperature above 0 K emits radiation. Following Planck's law, the temperature of a black body[1] determines how much and in which wavelength region this radiation is emitted. The Stefan-Boltzmann law states that the integrated flux F ($\mathrm{W\,m^{-2}}$) emitted by such a black body is proportional to the fourth power of its absolute temperature T (K),

$$F = \sigma T^4$$

where σ is the Stefan-Boltzmann constant ($5.670\times10^{-8}\ \mathrm{W\,m^{-2}\,K^{-4}}$). Wien's displacement law states that the wavelength λ_m (μm) at which a black body radiates its maximum amount of energy, is inversely proportional to its absolute temperature T (K),

$$\lambda_m = \alpha T^{-1} \tag{1.1}$$

where α is Wien's displacement constant ($2.898\times10^3\ \mathrm{\mu m\,K}$). Figure 1.1 shows, as a function of wavelength, the flux a black body with a temperature of 5780 K emits following Planck's law, which matches the general structure of the observed solar spectrum, and the flux a black body with a temperature of 255 K emits, which approximates the Earth's emission spectrum as viewed from space. This figure shows that the Sun emits part of its energy in the ultraviolet (UV) region (< 0.4 μm), part in the VIS (0.4 – 0.7 μm), and part in the infrared (IR) (> 0.7 μm), while the Earth emits all its energy in the IR wavelength range (0.7 – 1000 μm).

[1] A black body is a body in thermal equilibrium with its surroundings, which absorbs all incident radiation and thus reflects none, i.e. the emissivity is equal to 1 at all wavelengths.

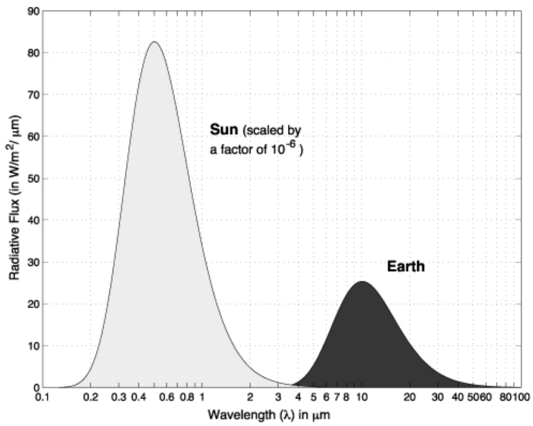

Figure 1.1: Black body flux of the Sun (left and scaled by a factor of 10^{-6}) and the Earth (right). Adapted from European Economic and Social Committee Spring Lectures 2007.

Filling in the black-body temperature values of the Sun and the Earth into Wien's displacement law (Eq. (1.1)), confirms the wavelengths at which the spectral flux is at its maximum in Figure 1.1: $\lambda_m = 0.50\,\mu\text{m}$ for the Sun and $\lambda_m = 11.36\,\mu\text{m}$ for the Earth.

The two spectra shown in Figure 1.1, represent the radiation emitted by the Sun (incoming solar radiation component), and the thermal infrared radiation emitted by the Earth (outgoing emitted radiation component). When observing the Earth from space, it is clear, with the bare eye, that there is also a component in the visible wavelength range. This is the third component of the ERB: the solar incoming radiation that is reflected by the Earth's surface and atmosphere, i.e. the outgoing reflected radiation component. When seen from space, the Earth has many colours, which means that it does not uniformly reflect the solar radiation, but that some parts of the Earth's surface and atmosphere reflect more than others. The amount of radiation that is reflected depends on the type of surface (ocean, vegetation, desert or snow), and can range from less than 5% for ocean to 90% for snowy surfaces. The reflectance of clouds is roughly proportional to the cloud thickness with thin cirrus clouds reflecting as little as 20% of the incoming flux and big convective clouds reflecting almost all incident solar radiation.

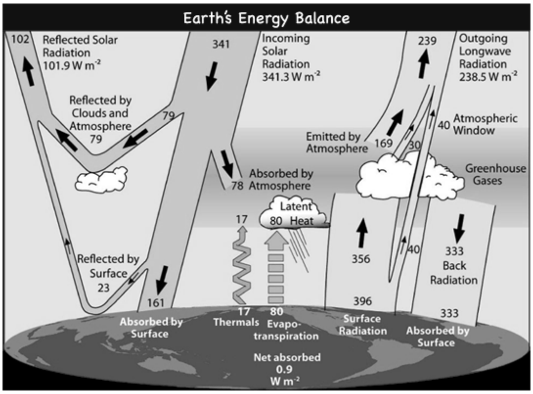

Figure 1.2: Radiation Balance of the Earth. From Trenberth et al. (2009).

Earth in radiative balance

The amount of solar radiation reaching the Earth has been extensively measured and the daily average is currently agreed to be about 341 $\mathrm{W\,m^{-2}}$ (Trenberth et al. 2009). Calculating the other two components is somewhat more complicated as there are several surfaces reflecting solar radiation and several sources emitting thermal infrared radiation, i.e. the clouds, aerosols, atmospheric molecules, and the Earth's surface. The Earth's energy balance is summarised in Figure 1.2. About 30% of the total incoming solar radiation is reflected by either the Earth's surface, clouds, atmospheric molecules or aerosols. Each type of terrestrial surface has its own properties of reflecting radiation, both in the ratio of reflected to absorbed radiation as in the direction into which the radiation is reflected. The same is valid for clouds, which can have very curvy tops, reflecting solar radiation in different directions, and can consist of water vapour and ice crystals, both with very different physical properties. Also aerosols and other atmospheric particles can, depending on their composition, shape and size, reflect different amounts of radiation, in a non-uniform way.

The remaining 70% of solar radiation that enters the Earth is absorbed by the Earth's surface and atmosphere, with the majority (almost half of the total solar flux) being absorbed by the surface. Both Earth's surface and the atmosphere reradiate this absorbed solar energy as infrared radiation. Only 20% of the reradiated surface energy leaves the Earth directly, the remainder is absorbed by the atmosphere and the clouds, and is reradiated again towards space and towards the Earth. Apart from their reflecting properties, clouds are also very good absorbers and emitters of infrared radiation. Covering roughly two-thirds of the Earth's surface, more than 90% of the radiation emitted by the surface and absorbed by the clouds, is reradiated towards the Earth and reabsorbed[2]. Even though it is difficult to measure all these processes, scientists have already been able to draw certain conclusions about the current climate evolutions (see Yang et al. (2013) for more on this). Before continuing, some radiation definitions need to be given, in order to simplify the explanation of the rest of this work.

1.1.2 Radiation definitions

Flux F (Wm^{-2}) – Spectral flux F(λ) (Wm^{-2} μm^{-1})

The amount of radiation coming from an object is most often expressed as **radiative flux** F ($\mathrm{W\,m^{-2}}$), i.e. the total amount of radiated energy per unit of time that comes perpendicularly through a unit of surface area[3]. As this flux is the total energy in a certain wavelength range, the **spectral flux** $F(\lambda)$ is defined as the flux per unit of wavelength ($\mathrm{W\,m^{-2}\,\mu m^{-1}}$). The flux coming from the Sun is called the **solar irradiance** S when it is integrated over a range of wavelengths, or **spectral solar irradiance** $S(\lambda)$ when it is expressed per unit of wavelength. The solar irradiance spectrum is shown in Figure 1.3, observed from both the Earth's surface (where the atmosphere accounts for a lot of absorption) and the TOA. The black-body curve is also given in the figure for comparison.

Radiance L (Wm^{-2} sr^{-1}) – Spectral radiance L(λ) (Wm^{-2} sr^{-1} μm^{-1})

In nature, radiation always comes from a certain direction. To take this dependency into account, the **radiance** L is defined as the flux per unit solid angle ($\mathrm{W\,m^{-2}\,sr^{-1}}$) and the **spectral radiance** $L(\lambda)$ as the spectral flux per unit solid angle ($\mathrm{W\,m^{-2}\,sr^{-1}\,\mu m^{-1}}$). The solid angle Ω of an object is defined as follows. Take a sphere of radius one centered at the origin of the coordinate system (the unit sphere), and draw lines from the center of the sphere to every point on the radiating object. This way, the surface of the object is projected onto the unit sphere. This projected surface area is called the solid angle of that object. As reference, the solid angle of an object that completely surrounds a point is 4π sr.

The most basic satellite instrument, the radiometer, has detectors whose output is proportional to the amount of energy per unit time reaching it. Such a detector has a fixed surface area, the radiation beam always reaches it from a certain solid angle, and band pass filters and the material the detector is made of regulate which wavelength range of the radiation is measured by the detector.

[2] More information on the whole energy balance of the Earth and how the atmosphere and oceans redirect heat internally, can be found in Chapter 2 of Burroughs (2007).

[3] This definition of flux is in the literature also often called flux density, distinguishing it from flux which then represents the amount of energy per unit of time (W).

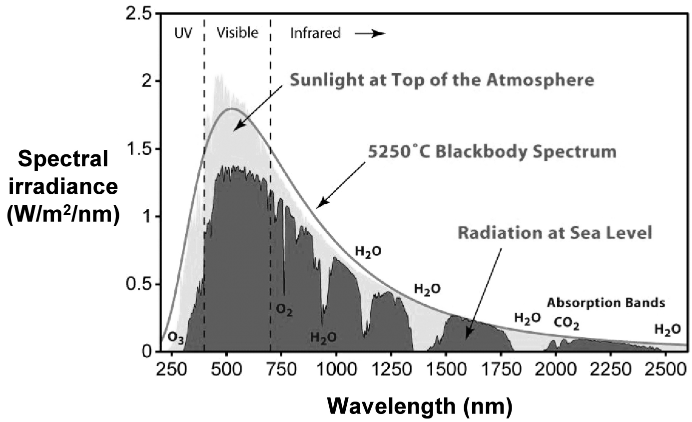

Figure 1.3: Solar irradiance spectrum at sea level (dark grey surface), at the TOA (light grey surface), and the black-body spectrum (grey full line). Adapted from Pagliaro et al. (2008).

For that reason, the radiance is the most fundamental satellite radiation quantity used. This is further discussed in Section 1.3 where it is described how the calibration of instruments happens.

Spherical coordinate system

Figure 1.4 shows a typical Sun-Earth-Satellite geometry where the radiation coming from a target on the Earth's surface (either reflected solar or emitted thermal) is observed by a satellite and the whole system is irradiated by the Sun. The zenith is the imaginary point directly above the target, perpendicular to the surface. The angle between the zenith and the Sun is called the solar zenith angle θ_0, while the angle between the zenith and the satellite is called the viewing zenith angle θ. The plane that runs through the target and is perpendicular to the vertical through the target and the zenith, is called the azimuth plane. The direction of forward scatter in the azimuth plane on Figure 1.4 is the direction of the component of the Sun's reflected radiation in the azimuth plane if the Earth's surface would be a perfect mirror. The relative azimuth angle ψ is defined as the angle between this forward scattering direction and the projection of the satellite position on the azimuth plane. If ψ would be equal to zero, and $\theta_0 = \theta$, a perfect mirror would reflect all radiation from the Sun right back in the direction of the satellite (specular reflection).

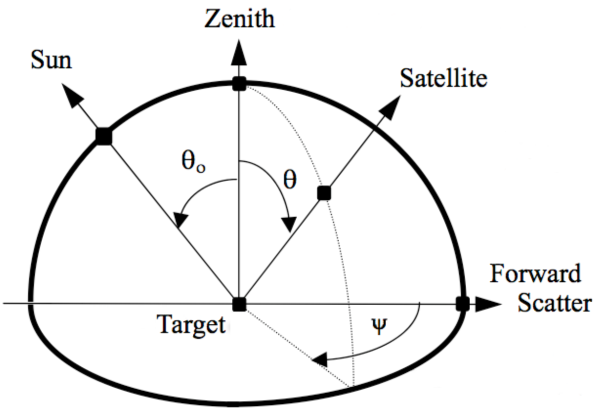

Figure 1.4: The upper hemisphere, showing the definition of the geometry angles θ_0, θ and ψ. Adapted from the CERES home page.

Lambertian reflector

As mentioned, part of the radiation from the Sun is reflected by the Earth's surface and atmosphere. Even though the beam of solar radiation comes from a specific direction, the Earth is not a perfect mirror and so the radiation is reflected in more than one direction, depending on the type of reflecting surface. A Lambertian surface is a special case, which reflects the incoming radiation uniformly in all directions. As the reflected spectral flux $F(\lambda)$ is equal to the reflected spectral radiance $L(\lambda,\theta,\psi)$ integrated over all angles in the upper hemisphere,

$$F(\lambda) = \int_{\Omega} L(\lambda,\theta,\psi)\cos\theta\, d\Omega$$

where $\cos\theta$ accounts for the amount of energy reflected perpendicular to the surface. The reflected spectral radiance $L(\lambda,\theta,\psi)$ is not angle dependent as it reflects uniformly in all directions, so $L(\lambda)$ comes out of the integral,

$$F(\lambda) = L(\lambda)\int_{\Omega} \cos\theta\, d\Omega. \tag{1.2}$$

For an infinitesimal solid angle $d\Omega$ in the direction of zenith angle θ and azimuth angle ψ,

$$d\Omega = \sin\theta\, d\theta\, d\psi.$$

Filling this in into Eq. (1.2), leads to

$$\begin{aligned} F(\lambda) &= L(\lambda) \int_{\theta=0}^{\pi/2} \int_{\psi=0}^{2\pi} \cos\theta \sin\theta \, d\theta \, d\psi \\ &= 2\pi \, L(\lambda) \int_{\theta=0}^{\pi/2} \cos\theta \sin\theta \, d\theta \\ &= \pi \, L(\lambda). \end{aligned} \tag{1.3}$$

This shows that, for a perfect Lambertian surface, the ratio of reflected flux to radiance is equal to π sr.

Reflectance ρ ***– Spectral reflectance*** $\rho(\lambda)$

The **spectral reflectance** $\rho(\lambda)$ is a unitless variable, which represents the ratio of outgoing spectral radiance to incoming spectral radiance

$$\rho(\lambda) = \frac{L_{\text{out}}(\lambda)}{L_{\text{in}}(\lambda)} = \frac{L(\lambda, \theta_0, \theta, \psi)}{\frac{S(\lambda)\cos\theta_0}{\pi \, d^2}} \tag{1.4}$$

where the incoming spectral radiance $L_{\text{in}}(\lambda)$ is written as a function of the known spectral solar irradiance $S(\lambda)$, assuming a uniform Lambertian distribution. $L_{\text{in}}(\lambda)$ decreases with increasing θ_0 and with increasing Earth-Sun-distance d. The angle dependency is shown by the added $\cos\theta_0$ in the denominator of Eq. (1.4), and the distance dependency by the $1/d^2$. The solar spectrum $(S(\lambda))$ from Figure 1.3 is measured at a fixed distance of 1 Astronomical Unit (AU) = 149 597 871 km, which is the mean distance between the Earth and the Sun. As the orbit of the Earth around the Sun is not a perfect circle, the distance between both does not stay the same all year, and so the d^2, expressed in AU, is added to Eq. (1.4) to correct for the elliptic orbit.

When both outgoing and incoming spectral radiances are integrated over the same wavelength region, the **reflectance** ρ is defined as the ratio of outgoing to incoming radiance.

Albedo A ***– Spectral albedo*** $A(\lambda)$

Compared to the reflectance, which is a ratio of radiances, the **spectral albedo** $A(\lambda)$ is defined as the ratio of outgoing to incoming spectral flux,

$$A(\lambda) = \frac{F_{\text{out}}(\lambda)}{F_{\text{in}}(\lambda)} = \frac{F(\lambda)}{\frac{S(\lambda)\cos\theta_0}{d^2}}. \tag{1.5}$$

When integrating over a fixed wavelength region, the **albedo** A is the ratio of outgoing to incoming flux.

1.1.3 Monitoring the climate

Climate changes have always been part of the Earth's history. Enough evidence is available to confirm that (Burroughs 2007). Between 1950 and 2011, a global near-surface temperature increase has been observed of about 0.6°C (Brohan et al. 2006), with a slightly higher temperature rise in the northern than in the southern hemisphere. As was already clear from Figure 1.2, due to the many sources reflecting and emitting radiation, it is not easy to perfectly identify the cause of this energy imbalance. It is even more difficult to know how much of it is human caused (due to the emission of greenhouse gases[4], desertification and deforestation, etc.) and how much is the result of naturally occurring phenomena (volcanoes, solar activity, etc.)[5]. For decades now, climatologists have been trying to understand all the mechanisms and how big the influence of these climate forcings exactly are.

Global Climate Observing System

In 1992, the Global Climate Observing System (GCOS) was established. It is an international initiative of the World Meteorological Organization (WMO) with the goal to organise a global network of observing systems to provide the minimal information on the global climate needed to observe, understand, predict and assess the impact of climate changes. GCOS provides recommendations for the delivery of long-term data records, called fundamental climate data records (FCDRs) and thematic climate data records (TCDRs). The FCDRs contain fluxes or radiances that have been derived directly from a series of different instruments, preferably with overlaps, and which have been extensively tested and calibrated[6] to ensure consistency over the entire record. Ground (in situ), airborne and space-based measurements are combined to provide global observations for the so-called essential climate variables (ECVs). All the GCOS ECVs are shown in Table 1.1, where the ones that can be measured from satellite observations, are indicated in bold. Specific geophysical variables, important for climate change, are derived from these ECVs and data records are created for them from the long-term FCDRs, creating the TCDRs. Accuracy and stability requirements for the FCDRs and TCDRs were written down in the GCOS Implementation Plan (GIP) for the global observing system for climate in support of the United Nations Framework Convention on Climate Change (UNFCC) (WMO 2006). These

[4]Greenhouse gases are gases in the Earth's atmosphere, which absorb radiation, both from the Sun and the Earth, and in their turn emit infrared emission, both back to the Earth and into space, with the net effect of warming up the lower atmosphere and cooling down the upper layers.

[5]For the interested reader, more information on these different sources of climate change can be found in Chapters 6 and 7 of Burroughs (2007).

[6]Section 1.3 discusses the calibration of instruments.

Table 1.1: Table of all GCOS ECVs. The ones that can be measured through satellite observations are indicated in bold.

Domain	GCOS Essential Climate Variables (ECVs)
Atmospheric (surface)	Air temperature, **wind speed and direction**, water vapour, air pressure, **precipitation**, **surface radiation budget**
Atmospheric (upper-air)	**Temperature**, **wind speed and direction**, **water vapour**, **cloud properties**, **Earth radiation budget**[1]
Atmospheric (composition)	**Carbon dioxide**, **methane and other long-lived greenhouse gasses**, **ozone and aerosol**, **precursors**[2]
Oceanic (surface)	**Sea-surface temperature**, **sea-surface salinity**, **sea level**, **sea state**, **sea ice**, surface current, **ocean colour**, carbon dioxide partial pressure, ocean acidity, phytoplankton
Oceanic (sub-surface)	Temperature, salinity, current, nutrients, carbon ocean acidity, oxygen, tracers
Terrestrial	River discharge, water use, groundwater, **lakes**,[3] **snow cover**, **glaciers and ice caps**, **ice sheets**, permafrost and seasonally frozen ground, **albedo and reflectance anisotropy**, **land cover**,[4] **fraction of absorbed photosynthetically active radiation (FAPAR)**, **leaf area index (LAI)**, **above-ground biomass**, soil carbon, **fire disturbance**, **soil moisture**, **land surface temperature**

[1] Including solar irradiance
[2] Supporting the aerosols and ozone ECVs
[3] Water level in lakes and reservoirs, water storage
[4] Including vegetation type

requirements were based on the expected variability of the ECVs on different timescales and were meant mostly as a starting point for discussions. International data centers work together to create these climate data records and assure the best possible accuracy and stability.

Climate Monitoring Satellite Application Facility

The European Space Agency (ESA) launched the first European weather satellite in 1977. Soon, more instruments followed and it was recognised it would be useful to create an organisation which would focus on the operation of the meteorological satellites alone. On 19 June 1986, the European Organization for the Exploitation of Meteorological Satellites (EUMETSAT), based in Darmstadt, Germany, was created to take over the operations of the meteorological space instruments from ESA. EUMETSAT was formed with the primary objective to establish, maintain and exploit European systems of operational meteorological satellites. Later on, the member states recognised the increasing need for climatological research and responded by extending EUMETSAT's mandate in 2000. Next to governing the operations of meteorological satellites, this extended mandate allowed also to contribute to the operational monitoring of the climate, as well as the detection of climate changes. This enabled a shift from a single focus on operational meteorology toward involvement with European partners in climate and environmental monitoring.

To participate with GCOS, EUMETSAT created in 1999 the Climate Monitoring Satellite Application Facility (CM SAF) (Schulz et al. 2009). It is a joint activity of 6 European national meteorological and hydrological services, under the supervision of the Deutscher Wetterdienst (DWD), including the Royal Meteorological Institute of Belgium (RMIB). As required by the GIP, the CM SAF provides long-term datasets of ECV products using satellite data (e.g. Roebeling et al. (2006), Peltoniemi et al. (2010), Reuter et al. (2010), Bugliaro et al. (2011), Mueller et al. (2011), Posselt et al. (2012)). RMIB has been involved since the beginning in the generation of climate data records for the TOA ERB (Dewitte et al. 2008), and, more recently, also in aerosol optical depth (AOD) (medium and) long-term data records (De Paepe & Dewitte 2009). Currently, CM SAF is in its Second Continuous Development and Operations Phase (CDOP-2), which runs from 2012 until 2017, containing a series of datasets which will be delivered during the course of this project. The work explained here supports EUMETSAT in the delivery of a TCDR for the TOA outgoing radiation within this CDOP-2, using the observations from the MFG imagers.

Satellite measurements

To do climate research, global observations are necessary, and for this, satellite data have been extremely useful (Yang et al. 2013). The first instrument in space measuring the ERB was called the ERB instrument, and was observing onboard the National Aeronautics and Space Administration (NASA) satellites Nimbus-6 and -7. These instruments measured both solar and Earth radiances in the UV, VIS, and IR wavelengths, from 1975 onwards. An improved generation of ERB instruments came with the Earth Radiation Budget Experiment (ERBE), also measuring both Sun and Earth radiation, where the first two instruments were put onboard the Earth Radiation Budget Satellites (ERBSs) in 1984, and more followed on the NOAA-9 and -10 satellites in 1984 and 1986. In 1994, the Scanner for Radiation Budget (ScaRaB) cooperative project between France, Russia and Germany was launched onboard of the Russian Meteor-3/7 satellite, and took measurements of the Earth in four channels (VIS, solar, total and IR window). NASA made sure there was a follow-up of the ERBE instruments when they created the Clouds and Earth's Radiant Energy System (CERES) instruments. The first was onboard of the Tropical Rainfall Measuring Mission (TRMM), launched in November 1997, and more followed on the Terra, Aqua and NPP satellites, with the more recent ones still in space. The CERES instruments also take measurements of the Earth's reflected and emitted radiation. EUMETSAT added the Geostationary Earth Radiation Budget (GERB) instrument to the Meteosat Second Generation (MSG) satellites, with the first one launched onboard Meteosat-8 in August 2002, which measures the outgoing Earth radiation in the VIS and IR bands.

All of these instruments were made to measure explicitly two or three of the ERB components, through spectrally flat and broad channels in the VIS, IR, and/or UV parts of the wavelength region. However, many more instruments were launched in the meantime, meant to do measurements for climate research. A few examples are summed up here. The Advanced Very High Resolution Radiometer (AVHRR) instruments of the National Oceanic and Atmospheric Administration (NOAA) measure the radiation coming from the Earth in 4 to 6 narrow VIS and IR channels, where each channel is used for different purposes (daytime cloud and surface mapping, snow and ice detection, sea surface temperature, etc.). The High Resolution Infrared Sounder (HIRS) instruments, provided by NOAA and onboard EUMETSAT's Metop-A and -B and NOAA's NOAA-18 and -19, measure the Earth's temperature profile, moisture content, cloud height and surface albedo through 19 IR channels and 1 VIS channel. Onboard the American Geostationary Operational Environmental Satellitess (GOESs), the Solar Ultraviolet Imager (SUVI) measures the solar irradiance in the extreme-UV region through 6 bands. The Global Ozone Monitoring Experiment (GOME) covers the UV and VIS ranges to measure stratospheric ozone and other types of aerosols and atmospheric molecules for climate studies, atmospheric pollution, etc. EUMETSAT's Metop satellites also carry the Infrared Atmospheric Sounding Interferometer (IASI). Apart from very accurate measurements used for medium range weather forecasting, IASI was also designed to monitor atmospheric gasses like ozone, methane and carbon monoxide. CloudSat and the Cloud-Aerosol Lidar and Infrared Pathfinder Satellite Observation (CALIPSO) were launched together by NASA to study clouds and aerosols and their role in the weather and climate system.

Section 1.2 goes into more detail into the type of orbits these meteorological instruments are in, focussing more specifically on EUMETSAT's geostationary Meteosat series of satellites.

1.2 METEOROLOGICAL SATELLITES

In the second half of the 20th century, the launch of artificial satellites around the Earth led to a new era for the geophysical scientists. The first satellite which was successful in observing the Earth was the Explorer 7, with the Suomi radiometer onboard, which was launched in October 1959. This was the real start of Earth observations from space. These first meteorological satellites took low resolution pictures to observe weather, ocean and land. Over the years, the resolution improved and at the same time also the possibilities to use the data for forecasting purposes. Only by the end of the 20th century, instruments were put onboard to specifically make measurements needed to monitor the Earth's climate. The two typical orbits in which meteorological satellites observe the Earth are explained in the next section.

1.2.1 SATELLITE ORBITS

Low-Earth orbits

The low-Earth orbits (LEOs) are defined as orbits with an altitude between 160 km[7] and 2000 km. The inclination angle of the orbit with respect to the equator, can range from close to 0° to close to 90°. An often used LEO is the (near) polar orbit, when the satellites fly close to the poles, and cross the equator at an (inclination) angle close to 90°. Because the Earth is not a perfect sphere, but instead has an equatorial bulge, the orbital plane of the satellites does not stay fixed with respect to the rotation axis of the Earth. This allows meteorological satellites, for example, to fly in sun-synchronous orbits. In this type of LEO, the satellite passes the equator every time at a different place (as the Earth turns), but every time at the same local time. This is possible by combining the flight altitude and inclination angle in such a way that the angle between the orbital plane and the Sun always remains constant, and so the satellite orbit precesses exactly one time per year around the rotation axis of the Earth. A typical altitude for this type of satellites is 600–800 km with a period of 96–100 minutes and an inclination of about 98°. This way the satellite orbits the Earth roughly 16 times a day. Examples of meteorological satellites in these sun-synchronous orbits, are the NOAA satellites, the EUMETSAT Polar System Metop satellites, NASA's Terra and Aqua satellites, CALIPSO, CloudSat, the Polarization & Anisotropy of Reflectances for Atmospheric Sciences coupled with Observations from a Lidar (PARASOL), and the Japanese Global Change Observation Mission-Water (GCOM-W1). Each of these satellites carries its own instruments onboard, useful for all different kinds of climatological measurements.

Apart from the sun-synchronous LEOs which precess about 1°/day, a whole range of inclination angles and precession rates are possible. For example, TRMM flew at an altitude of 350 km, an inclination angle of 35°, and a precession rate of about 6.6°/day. This way, TRMM passed above a certain location on the Earth's surface at a different local time each day, allowing to observe that location from different angles. The ERBS observed the Earth between 1984 and 2003, flying at an altitude of 585 km and inclination angle of 57°.

---

[7] Orbits lower than this would circle inward too fast due to the atmospheric air resistance.

Table 1.2: The advantages and disadvantages of the sun-synchronous LEOs, precessing LEO, and GEOs for climatological purposes.

Orbit	Advantages	Disadvantages
Sun-synchronous LEO	Full Earth coverage, higher spatial resolution, possibility of active instruments (lidar, radar, scatterometer), observations from different viewing geometries	Lower revisit time, observation at fixed solar time, subject to orbital drifts
High precessing LEO	Observation of the diurnal cycle, higher spatial resolution, possibility of active instruments (lidar, radar, scatterometer), observations from different viewing geometries	Lower irregular revisit time, limited Earth coverage
GEO	Higher observation frequency, Observation of the diurnal cycle	Limited Earth coverage (±40%), lower spatial resolution, each part of the field–of–view (FOV) is observed from the same viewing geometry, needs powerful optics, no observations of polar regions, no active instruments onboard (lidar, radar, scatterometer)

Geostationary orbits

A geostationary orbit (GEO) is a circular orbit in the plane of the equator which follows the rotation of the Earth. This means that the satellite always looks at the same part of the Earth (about 40% of the Earth surface) and so has a period of one sidereal day (≈ 23 hours 56 minutes and 4 seconds). To be able to accomplish this exact orbital period, the satellite needs to be at an altitude of 35 786 km above the equator, so much higher than the LEOs. Table 1.2 compares the advantages and disadvantages of the LEOs and the GEO from climatological point of view. This shows why the LEOs are more often used to put instruments in space which are useful for climatological research.

Compared to the LEOs, for which there can be lots of different possible orbits depending on the altitude and inclination, there is only one GEO, also called the geostationary belt. ESA launched its first satellite in 1977 in a GEO and called the satellite Meteosat. In the years that followed, more and more satellites in the Meteosat series were sent into space, with the most recent one, Meteosat-10, launched in 2012. All satellites were operationally exploited close to 0° longitude. Some of them were moved to the west or to the east of the geostationary belt when their successor became the operational satellite at 0° longitude. Since the late nineties, the full belt is covered by geostationary instruments taking mea-

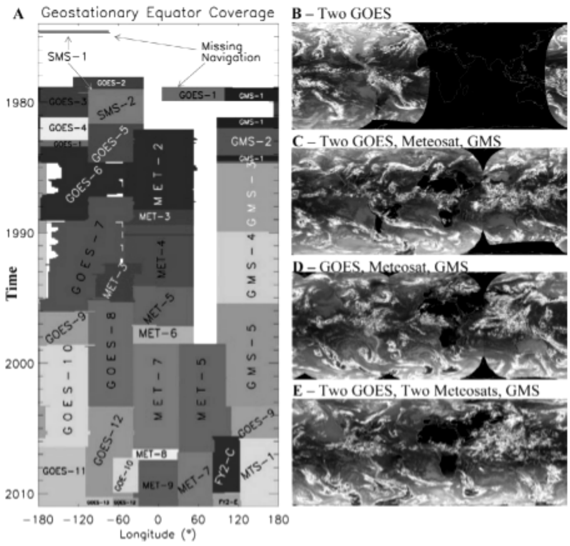

Figure 1.5: The occupation of the geostationary belt by meteorological satellites between 1974 and 2011. From Knapp et al. (2011).

surements of the Earth. As shown in Figure 1.5, initially this was done only by NASA with the GOES satellites, EUMETSAT with the Meteosat instruments, and Japan with the Geostationary Meteorological Satellite (GMS). More recently, Russia, China and India added their own instruments to the geostationary ring.

In the next two sections, EUMETSAT's geostationary satellites are described, giving more information about the instruments onboard of the Meteosat satellites, and showing a historic overview of these instruments in space.

1.2.2 Meteosat First Generation

The MFG programme consists of 7 spin-stabilised geostationary satellites, called Meteosat-1 till -7, for which the timelines are shown in Figure 1.6. The first three satellites were part of the pre-operational phase. The imager of Meteosat-1 failed after two years due to a design fault (EUMETSAT 2011), and as its images were never transcribed into the archive, it is not used here. The Data Collection System (DCS) onboard Meteosat-1[8], however, con-

[8] The Meteosat satellites carry a DCS, through which they provide a relay service to the Meteosat ground station for observations from about 1000 Data Collection Platforms (DCPs) carried by ships,

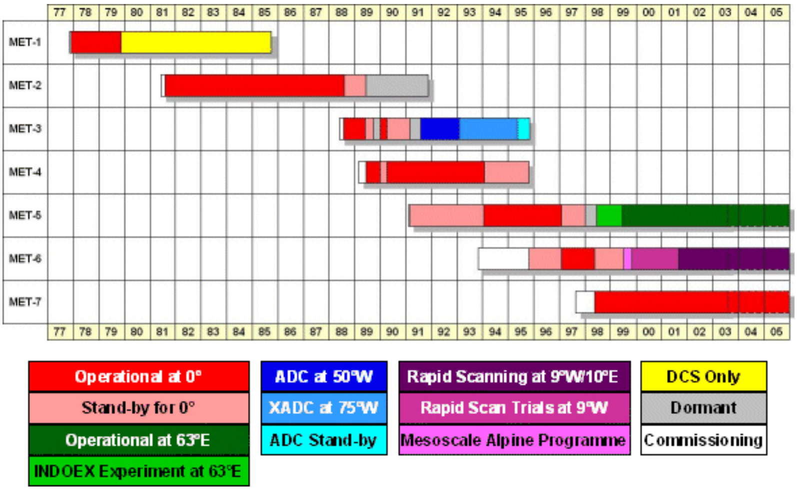

Figure 1.6: The timeline of all 7 MFG satellites in their different operational modes.

tinued relaying signals to the ground station until 1984. With Meteosat-4, the Meteosat Operational Programme (MOP) started, also launching Meteosat-5 and -6 into space. The last of the MFG instruments was part of the Meteosat Transition Programme (MTP) to the second generation of Meteosat satellites, and was called Meteosat-7. All 7 instruments mainly worked at the nominal position at 0° longitude, but some were also used in other programs, covering other parts of the geostationary ring. For example, Meteosat-3 was used over the Atlantic Ocean, providing data to NOAA in the Atlantic Ocean data coverage (ADC) and Extended ADC (X-ADC), to bridge a gap of GOES-East data. Meteosat-5, -6 and -7 were operational over the Indian Ocean to support the Indian Ocean Experiment (INDOEX) in the Indian Ocean data coverage (IODC). Meteosat-6 was also part of the international Mesoscale Alpine Programme (MAP) for a short period of time, where it scanned the alpine region at five-minute intervals, and in the Rapid Scanning Service (RSS) afterwards. Table 1.3 shows the time period and position while each of the satellites was operational.

The imager onboard of the MFG satellites is called the Meteosat Visible and Infrared Imager (MVIRI), which scans the Earth in three spectral channels: the VIS, the water vapour (WV), and the IR band. The normalised spectral response (SR) curve of a channel shows for each wavelength the percentage of incoming

aircrafts and other mobile platforms.

Table 1.3: Timeline of the MFG satellites, showing the time period when and the longitude where each instrument was operational.

Satellite	Launch – graveyard	Status
Meteosat-1	23/11/1977 – 12/1984	0°: 12/1977 – 11/1979
Meteosat-2	10/06/1981 – 12/1991	0°: 08/1981 – 08/1988
Meteosat-3	15/06/1988 – 05/1995	0°: 08/1988 – 01/1991 50° W (ADC): 08/1991 – 01/1993 75° W (X-ADC): 02/1993 – 05/1995
Meteosat-4	19/04/1989 – 11/1996	0°: 06/1989 – 02/1994
Meteosat-5	02/03/1991 – 02/2007	0°: 02/1994 – 02/1997 63° E (IODC): 07/1998 – 02/2007
Meteosat-6	20/11/1993 – 04/2011	0°: 02/1997 – 06/1998 9° W (MAP): 08/1999 – 11/1999 10° E (RSS): 11/1999 – 01/2007
Meteosat-7	03/09/1997 – TBD	0°: 06/1998 – 07/2006 57.3° E (IODC): 11/2006 – TBD

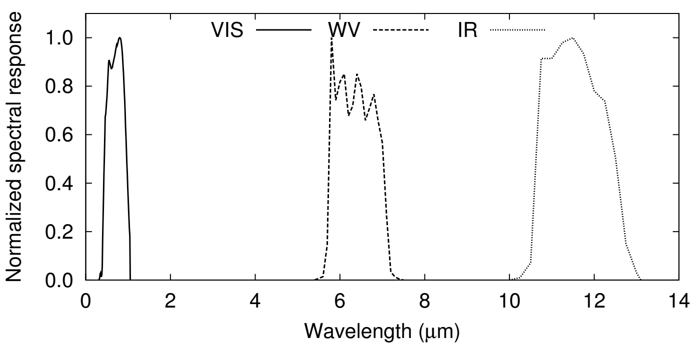

Figure 1.7: The normalised SR curves of the VIS, WV, and IR channels of Meteosat-7.

radiation that is actually observed by the telescope and detectors. For a perfect instrument, this would be equal to 1 over the whole range. In reality, however, this is not the case. The SR curves of the three MVIRI channels are shown as a function of wavelength in Figure 1.7 for the last of the MFG series, Meteosat-7, while Table 1.4 summarises their most important characteristics. The radiation observed by MVIRI is first captured by the tilting and rotating section (made of

Table 1.4: Characteristics of the three MVIRI channels.

Property	VIS	WV	IR
$\lambda_{min} - \lambda_{max}$	$0.5 - 0.9\mu m$[1]	$5.7 - 7.1\mu m$	$10.5 - 12.5\mu m$
Temporal frequency	25 minutes scanning + 5 minutes retracing scan mirror		
Pixel resolution[2]	2.5×2.5 km	5×5 km	5×5 km
Spinning speed	100 rotations per minute, from East to West		
Scanning speed	1.25×10^{-4} radians per rotation, from South to North		
Number of detectors	2	1	1
Detector material	Si	HgCdTe	HgCdTe
Number of bits	6/8[3]	6/8[3]	8
Level 1.5 image size[4]	5000×5000 pixels	2500×2500 pixels	2500×2500 pixels
Field of view (FOV)	18° (0.314 rad)		

[1] This is the bandwidth for which the pre-launch characterisation was done. Afterwards, an extrapolation was performed increasing the bandwidth to $0.3 - 1.3\mu m$

[2] The resolution is at nadir, which is the point right below the observer, the point opposite the zenith.

[3] 6 bits for Meteosat-1, -2, -3 and 8 bits for Meteosat-4, -5, -6 , -7.

[4] The Level 1.5 images are geolocated and rectified.

3 mirrors) which allows to observe the full Meteosat FOV from South to North and from East to West. The rotating section contains a Ritchey-Chrétien telescope, shown at the right side of Figure 1.8. This type of telescope consists of a hyperbolic primary mirror with a diameter of 400 mm and a hyperbolic secondary mirror with a diameter of 140 mm. Through a series of smaller mirrors, the radiation is focused onto the detectors of the different channels (towards the left side of Figure 1.8). A black body is present on the Meteosat-7 satellite alone, used for calibration purposes of the IR and WV detectors. Right in front of all detectors, a field stop aperture makes sure that the radiation that falls onto the detector always comes from the same size of rectangular spot on the Earth.

MVIRI VIS channel

The VIS detectors, which convert the observed VIS radiation into electrical currents, are silicon photodiodes. Darmont (2009) explains with Figure 1.9 the workings of these types of diodes, showing the amount of electrical current coming from each region in the semi-conductor, for incoming radiation with different wavelengths. Silicon has a natural wavelength range of absorption, which runs

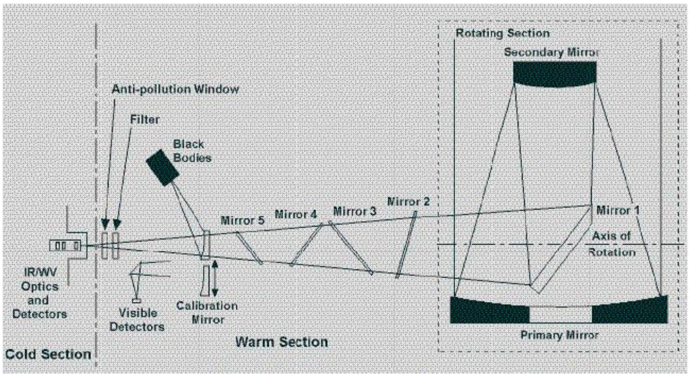

Figure 1.8: MVIRI optics, showing at the right the Ritchey-Chrétien telescope, which redirects the radiation, through a series of mirrors, to the three types of detectors (at the left side). Image from EUMETSAT.

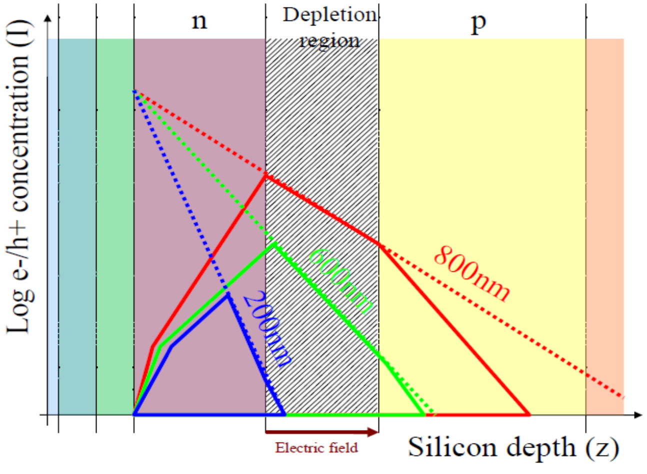

Figure 1.9: A silicon photodiode with several oxides at the surface (shades of blue) at the left, going deeper into the material when moving to the right. The surface beneath the curves show the amount of current retrieved when the material is radiated by wavelength beams of 200, 600 and 800 nm. Figure from Darmont (2009).

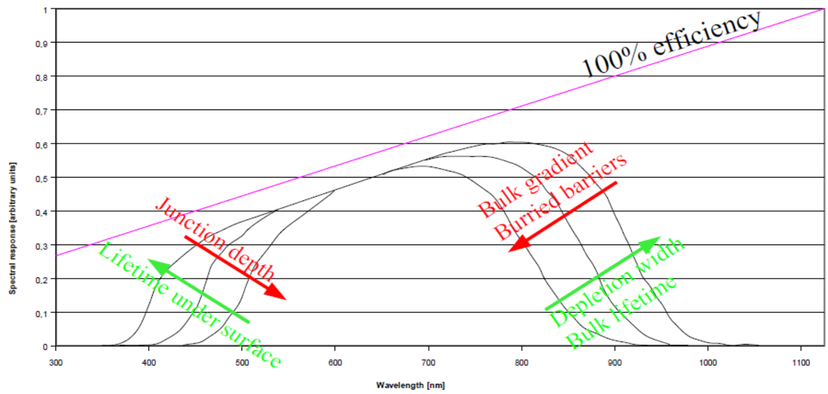

Figure 1.10: The dependencies of the SR curve of a silicon detector to different photodiode properties. Figure from Darmont (2009).

up to 1.1 μm, covering the VIS wavelength range. Even though the diode material of the detector can stay the same, and a similar optical system can be used, the SR of a channel changes from instrument to instrument. Darmont (2009) shows with Figure 1.10 the dependencies of the shape of the SR of such silicon detectors to different parameters (how far the junction is from the surface, how long it takes before recombination occurs, etc.). Apart from these different properties of the photodiode itself, the paper also explains the optical effects that can occur when the incoming light needs to cross boundaries between stacked layers in the detector. Part of the light will be reflected back, and part will be refracted. The reflected ray will partly be reflected on the boundary with the previous layer, and will interfere with the original light beam. They show how this affects the SR of the detector, and how this results in a dependency on the angle of the incoming light with respect to the detector surface. No filter was used for the VIS channel of the MVIRI instruments, so the shape of the SR is determined mainly by the silicon detectors.

Apart from the SR of the detectors, the mirrors, which direct the incoming radiation to the detectors, also have a specific SR. Either the SR of each of these individual components is measured by the instrument manufacturers, or the total summated SR curve of the instrument is calculated at once. These measurements are done by illuminating the instrument with light at different wavelengths. As, at the time the SR of the MVIRI instruments were characterised no lasers were available yet, the light beams used for this characterisation were not monochromatic, but usually had a gaussian shape around a central wavelength. This is an extra source of uncertainty on the SR curves.

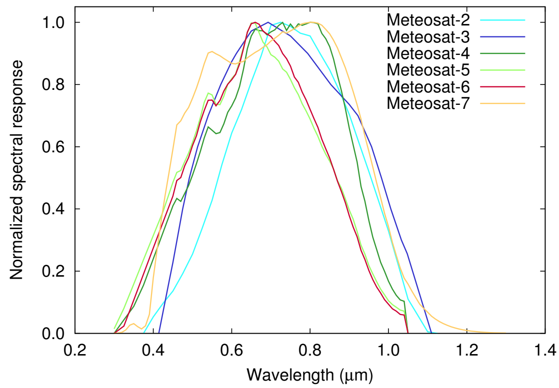

Figure 1.11: The VIS SR curves of the MVIRI instruments onboard of the Meteosat-2 till -7 satellites.

The pre-launch characterisations of the VIS channels of the MVIRI instruments of Meteosat-2 till -7 are shown in Figure 1.11. Although the SR curves that have been made available to the public on the EUMETSAT webpage (www.eumetsat.int) range from at least 0.3 – 1.3µm, they were only characterised between 0.5 – 0.9µm. The rest has been empirically extrapolated by hand. Govaerts et al. (2004) show the uncertainty on the SR curves of Meteosat-2 till -7. Next to the extrapolation, a part of the uncertainty comes from the use of non-monochromatic light beams (as explained before), and another part comes from the errors on the instruments used to do the SR measurements. Govaerts et al. (2004) computed a total uncertainty that varies between 0 and 20% of the SR, depending on the wavelength range.

After the detectors convert the incoming radiation into electrical currents, this electrical current is digitised, through either 6 or 8 bits. The 6-bit digitisation transforms the signal into a value between 0 and 63, the 8-bit digitisation into a value between 0 and 255. For Meteosat-1, -2, and -3, the digitised signal of the VIS channel was multiplied by 4 to get a number in the same 0 – 255 range as the other 8-bit channel. To optimise this digital range, for each satellite, an electronic gain level can be selected between 0 and 15. This way, saturation can be avoided by lowering the gain, or the gain can be increased when the highest measured value at local noon is less than 212[9]. This digitised and optimised sig-

[9]The gain steps have an approximate ratio of 1.2. Because of this, an increase in gain level can only be done when the maximum daily value becomes less than 212, so that after the gain change the maximum value is still less than 255 (i.e. 212×1.2).

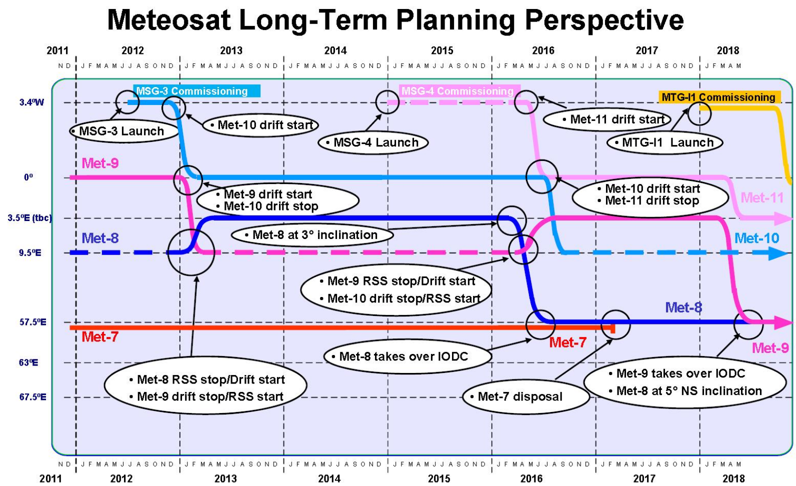

Figure 1.12: Long-term planning of the positions of the current and future MFG and MSG satellites in space.

nal is then sent to Earth to create the images, expressed in so-called digital count (DC), which can be retrieved from the EUMETSAT Portal.

1.2.3 METEOSAT SECOND GENERATION

The MTP was established to ensure the operational continuity between the end of the MOP (Meteosat-4, -5 and -6) and the MSG (Schmetz et al. 2002), where the latter has brought three satellites (Meteosat-8, -9, and -10) into orbit so far, and is planning on launching the last, Meteosat-11, in 2015. All four MSG instruments start their operational period around the nominal position of 0° longitude, as did the MFG satellites. Figure 1.12 shows the planning (from 2011 onwards) of the positions of the current and future operational Meteosat satellites.

Onboard of these satellites are two important instruments. The Spinning Enhanced Visible and Infrared Imager (SEVIRI) is the successor of MVIRI, scanning the Earth through 12 channels: 11 narrow channels and one broader high resolution visible (HRV) channel. Their SR curves are shown in Figure 1.13 for Meteosat-8, while some important characteristics of the channels are given in Table 1.5. The HRV channel of Meteosat-8 is used later on in this work in Chapter 6, in a validation study of the Meteosat-7 VIS SR curve at launch. The second instrument onboard the MSG satellites is called the GERB instrument

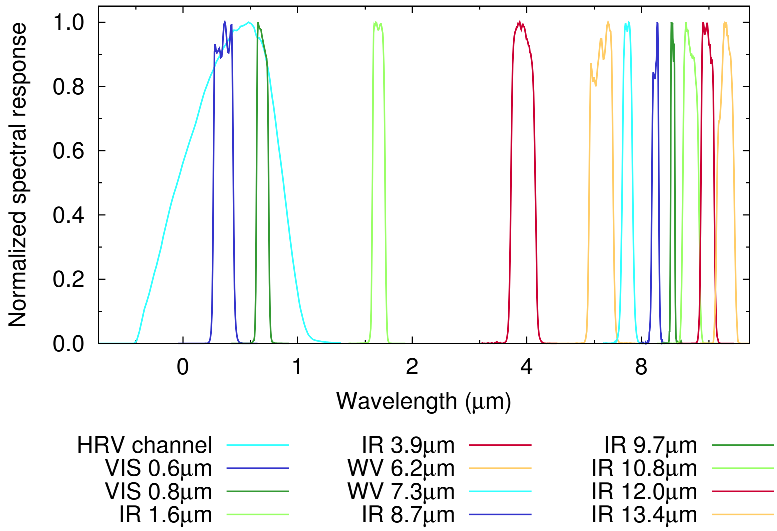

Figure 1.13: The SR curves of the 12 SEVIRI channels of Meteosat-8.

Table 1.5: Characteristics of the twelve SEVIRI channels.

Property	HRV	11 narrow channels
$\lambda_{min} - \lambda_{max}$	0.45 – 1.05μm[1]	0.6, 0.8, 1.6, 6.2, 7.3, 3.9, 8.7, 9.7, 10.8, 12.0, and 13.4μm
Temporal frequency	15 minutes	
Pixel resolution[2]	1×1 km	3×3 km
Spinning speed	100 rotations per minute, from East to West	
Scanning speed	1.25×10^{-4} radians per rotation, from South to North	
Number of detectors	9	3
Number of bits	10	
Image size	11136×5568 pixels	3712×3712 pixels
Field of view (FOV)	18°	

[1] This is the bandwidth for which the pre-launch characterisation was done. Afterwards, an extrapolation was performed increasing the bandwidth to 0.3 – 1.3μm
[2] The resolution is at nadir, which is the point right below the observer, the point opposite the zenith.

(Harries et al. 2005). It monitors the Earth through a shortwave (SW) channel and a total (TOT) channel. The longwave (LW) measurements are obtained from subtracting the shortwave from the TOT channel.

1.3 CALIBRATION AND DEGRADATION

In order to use data from different satellites to create long-term climate data records, a consistent calibration is needed between the different instruments. Calibrating data means converting the digital output of the imager into physical values[10]. As mentioned in Section 1.1.2, the digital output of a radiometer is proportional to its radiance. As a radiometer is constructed to respond linearly to the incoming radiance intensity, a linear relation is used between the original values v in DC and the radiances L, which should be the same for all scene types at launch,

$$L = C\,(v - O) \tag{1.6}$$

where C is the calibration coefficient and O the offset.

For some instruments, devices are present in space to calibrate the instruments on a regular basis. This is often the case for the IR channels, making use of a black body at a controlled temperature. If there is, however, nothing onboard the satellite to do the calibration, as is the case for the MFG satellites (except for the black body onboard Meteosat-7), other ways need to be found. These substitute calibration techniques are called vicarious calibrations. As this thesis only works with the VIS data, the next section will only discuss vicarious calibration techniques used for the VIS channels of space instruments.

1.3.1 VICARIOUS CALIBRATION

There are several ways to do vicarious calibration of VIS images, with the majority being either intercalibrations with well calibrated instruments, or calibrations using radiative transfer models. Concerning Meteosat, among the intercalibration studies, Brooks et al. (1984) did an intercomparison study between the Meteosat-1 and GOES-2 VIS data for calibration purposes. Kriebel & Amann (1993) used an airborne radiometer which viewed stable Earth targets simultaneously with the Meteosat-1, -2 and -4 satellites. In the work of Cabot et al. (1994), Meteosat-4 VIS data were compared with AVHRR to calibrate it. In these studies, the calibration of the Meteosat imager is always relative to

[10] As the digital output depends on the gain settings, the calibration changes when the gain level is adjusted during the lifetime of an instrument in space.

the other instrument, of which the assumption is made that it is stable in time and has been calibrated well enough to use as a reference. In 2005, the Global Space-based Intercalibration System (GSICS) was founded from an international idea to create a worldwide intercalibrated system of observations (Goldberg et al. 2011). This consistent calibration among space-based observations worldwide would improve climate monitoring, weather forecasting and environmental applications. In a first step, the main focus is on the intercalibration of IR channels worldwide, with an increasing interest and contribution to the VIS images.

The other type of vicarious calibration makes use of modelled radiances. Here, the digital output of the radiometer over certain well known sites (often bright desert, clear ocean, and/or convective clouds) is compared to simulated radiances L of these types of sites, taking into account the specific SR curve $\phi(\lambda)$ of the instrument through

$$L = \int_{\mathrm{VIS}} L(\lambda)\,\phi(\lambda)\,d\lambda$$

where $L(\lambda)$ is the simulated spectral radiance at the TOA at wavelength λ. For each site, the linear relation of Eq. (1.6) can be measured between the simulated radiance and the measured digital output. The slope of the regression through a whole series of such site comparisons, then leads to the calibration coefficient C. The offset O can be derived from night time observations. In preparation of the MSG satellites, EUMETSAT developed this type of vicarious calibration for the VIS bands of SEVIRI, called the SEVIRI Solar Channel Calibration (SSCC), which is based on radiative transfer model computations over bright desert and clear ocean targets with relatively well known spectral reflectances (Govaerts et al. 2001). The method was also applied to the MFG VIS archive (Govaerts et al. 2004) and proved to be successful in increasing the precision of the initial vicarious calibration. The full MFG archive has been reprocessed to derive this new calibration, and the SSCC method is now the official one, published on the EUMETSAT website. Other examples of vicarious calibration of the Meteosat instruments are shown in Koepke (1982*a*), Koepke (1982*b*), Moulin et al. (1996), and Arriaga & Schmetz (1999).

1.3.2 Degradation

Already in the early years of Meteosat's operational program, it was clear that, when performing the vicarious calibration, there was a drift in time in the data of Meteosat-2 due to degradation of the instrument's optics and detectors (Koepke 1982*a*). This ageing process can be explained as a decrease of the SR of the instrument, uniformly over the spectrum of the channel, so that, in time, less and

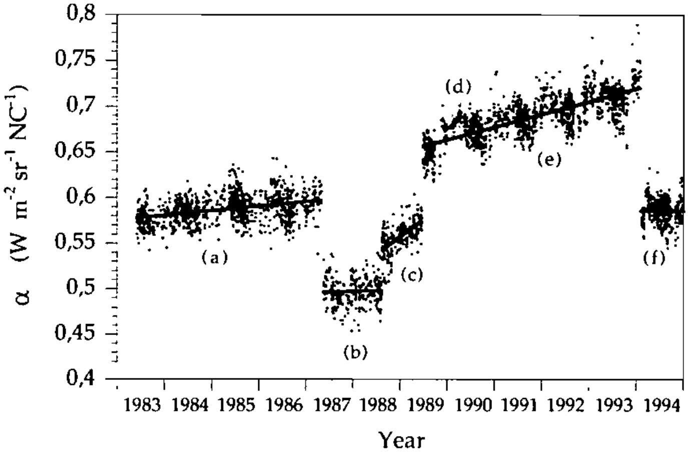

Figure 1.14: The time dependent calibration coefficients for Meteosat-2 (parts (a) and (b)), Meteosat-3 (parts (c) and (d)), Meteosat-4 (part (e)) and Meteosat-5 (part (f)). From Moulin et al. (1996).

less of the incoming radiation is actually captured by the detectors. It seemed possible to correct for this decreasing response by allowing the calibration coefficient to increase in time in a linear way. Moulin et al. (1996) calculated these time dependent calibration coefficients for Meteosat-2 till -5. This was done through vicarious calibration based on radiative transfer models, making use of four spectrally well known African sand desert targets. The calibration coefficients are shown in Figure 1.14 for these four instruments. Parts (a) and (b) represent Meteosat-2, where different gain levels were used for part (a) than for part (b). Parts (c) and (d) show the values for Meteosat-3, again for 2 different gain settings. Part (e) gives the Meteosat-4 calibration coefficients and part (f) shows the ones for Meteosat-5. Moulin et al. (1996) calculated a low linear drift for Meteosat-2 and -5 of about 0.5% per year, about 2% per year for Meteosat-4 and around 10% per year for Meteosat-3, although it is important to take the significant uncertainty into account for the latter. Also for other instruments degradation effects have been measured. Through vicarious calibration of Libyan desert scenes, Staylor (1990) measured 6% degradation per year for the VIS channel of NOAA-9. An exponential decay rate was measured by Bremer et al. (1998) for both the imager and sounder onboard the GOES-8 and -9 satellites, through measurements of approximately 30 stars. For GOME, ageing was measured by Snel (2001) using the Sun and the Moon as stable radiation sources. Even though

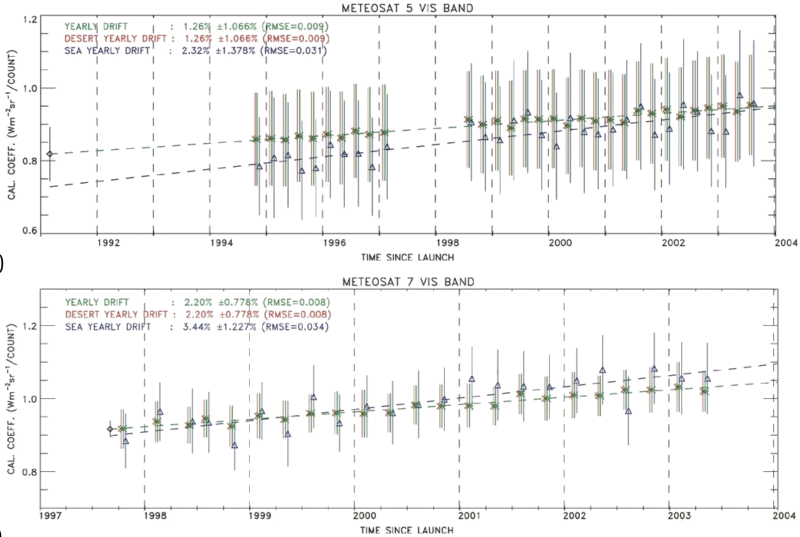

(a)

(b)

Figure 1.15: Figure from Govaerts et al. (2004) showing the linearly increasing calibration coefficient in time for (a) the Meteosat-5 VIS band, and (b) the Meteosat-7 VIS band data. The blue dashed line corresponds to the linear fit through the coefficients computed for the sea, the red line is for the desert and the green one for both scene types.

this is only a short list of instruments for which the decrease in response has been reported, in reality the majority of space instruments suffers from in-flight (or some even pre-flight) degradation effects.

The ageing of the 6 MVIRI instruments was also taken into account with the SSCC method. For each imager, the observed drift can be found on the EUMETSAT website, allowing the user to let the calibration coefficient increase linearly in time to correct for the degradation. Figures 1.15(a) and (b) show the calibration coefficients for Meteosat-5 and Meteosat-7 respectively, as deduced using the SSCC method.

1.3.3 Spectral degradation

Validation of the SSCC calibration method, which was also done by Govaerts et al. (2004), showed that the in-flight change of the SR is stronger for the short VIS wavelengths than for the longer ones. This was concluded from the following. In Figures 1.15(a) and (b) it can be seen that the calibration coefficients de-

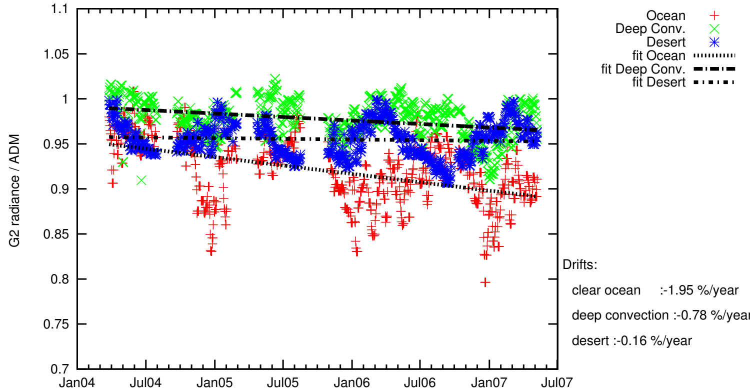

Figure 1.16: Spectral degradation for the GERB instrument onboard Meteosat-8 (unpublished results).

rived for the sea targets increase more strongly than for the desert targets, compensating for the stronger drift in the signal observed over sea than over desert. As the ocean reflectance spectrum is centered in the blue part of the VIS spectrum (shortest wavelengths), while the desert targets reflect more energy in the red part of the VIS spectrum (longer wavelengths), it is clear that the degradation has a spectral character. Resulting from this, it seems that the SR of the instrument does not decrease uniformly over the spectrum, as was initially assumed, but that it decreases stronger in the shorter wavelengths of the VIS channel than in the longer ones. Apart from the spectral degradation, the validation work of Govaerts et al. (2004) also showed a saturation of the drift in time. This means that the decrease of the signal starts linearly, but becomes less after a certain amount of time. This makes one believe the ageing is not fully captured by a linear model, but might be better modelled adding an exponential change in time.

The spectral degradation has also been observed for other instruments. It was reported by Matthews et al. (2005) for the CERES instruments (Wielicki et al. 1996), where different drifts were measured for clear-sky ocean scenes than for the other scenes. Hints of this spectral degradation are also visible in the data of the GERB instrument onboard of the MSG satellites (see Figure 1.16). Additional proof of spectral degradation was given by Delwart et al. (2006) for the Medium Resolution Imaging Spectrometer (MERIS) on-board the Environmental Satellite (ENVISAT), where a stronger modification of the SR was needed over time for the blue end of the spectrum than for the red end. Also the Moderate Resolution Imaging Spectro-radiometer (MODIS) and the Sea-viewing Wide Field–of–view Sensor (SeaWiFS), which are both narrowband instruments, suffer from a spectral on-orbit degradation. Doelling et al. (2010) and Xiong et al. (2009) report a higher degradation rate for the blue channels of these instruments than for the ones with a larger central wavelength. For narrowband detectors, however, it is sufficient to change the calibration coefficient for each channel independently, as the channels are small enough for the degradation to stay more or less constant over its spectral range.

It is already well known that self-contamination of instruments due to outgassing of lightweight molecules coming from moisture, lubricants, adhesives, etc., can lead to a decreasing SR of the instrument. It was also already known that the combination of ultraviolet light and large organic molecules can result in the deposition of tenacious films on, for example, the mirrors of the telescope, an effect called photo-deposition. More work was done to characterise the satellite contamination by e.g. Stewart et al. (1990), Frink et al. (1992), and Tribble et al. (1996). They show that typically, degradation that is induced by self-contamination, decreases exponentially as a function of time. On top of that, they prove that photo-deposition of contamination onto sensitive surfaces (detectors, mirrors), is a true source of spectral degradation. When the contaminants condense onto these surfaces and are then exposed to solar UV radiation, they will be photo-deposited. The high-energy UV radiation from the Sun also seems to polymerise the deposited material and thus change its optical properties so that it absorbs more radiation in the shorter wavelengths (UV and blue VIS) than in the longer (red VIS and near IR), explaining the effects reported by Govaerts et al. (2004).

1.4 CONTEXT OF THIS WORK

As mentioned before in Section 1.1.3, the CM SAF provides long-term datasets of ECVs from, among others, the Meteosat satellite data. RMIB is involved in creating a TCDR of the TOA outgoing GERB-like radiation from the MFG database. This climate data record will be created based on the overlap period of 2 years (2004 – 2006) between the Meteosat-8 GERB SW and the Meteosat-7 MVIRI VIS datasets. Empirical regressions will be computed for different scene types and Sun-Earth-satellite geometries, which can be used to convert these two years of Meteosat-7 VIS data into so-called GERB-like SW data. To do this regression correctly, however, it is important to use Meteosat-7 VIS images which have been corrected for spectral degradation effects. Also, in order to convert the rest of the Meteosat-7 database, and the VIS images of the previous satellites (Meteosat-2 till -6) based on these two years of GERB-like images, it is important to correct for the spectral ageing effects, and this way, improve the calibration consistency between the different Meteosat instruments.

For that reason, in this work, a semi-empirical model $\phi(\lambda, t)$ is created which incorporates the spectral effect discussed in the previous section. It models the way the pre-launch SR curve $\phi(\lambda, 0)$ of the VIS channel of the MVIRI instruments changes in time over its wavelength range, as seen in the rectified Level 1.5 images. The mathematical formula of the model is presented in Chapter 3 without the possibility of giving a full physical justification. The reason for this is that during the whole MFG history, real physical modeling of the degradation of the MVIRI instruments has never been carried out due to a lack of knowledge of the instrument characteristics and their behavior in space. As mentioned before, these instruments had already been designed by 1970, and have only been characterised with the accuracy permitted at that time. On top of that, these instruments were not meant to be used quantitatively at the moment they were built. Their primary goal was to take images of the clouds, the Earth's surface and atmosphere for forecasting purposes.

The fact that this work is based on the SR curve as it was characterised before launch, and there is serious doubt about the accuracy of these curves, poses a limitation to the generation of a FCDR from the corrections proposed in this work. It would have been possible to start this work on a more basic level, and try to model the sensor degradation based on the non-rectified non-geolocated Level 1.0 data. As the goal of the work, however, was to improve the consistency between the different satellites in order to generate the GERB-like database, it was sufficient to correct the Level 1.5 images at this point. On top of that, at the beginning, it was not clear which problems would be encountered along the way. Only at the end of this work, it was clear that there are other issues that need to be dealt with in order to generate the FCDR of visible reflectance for the MFG satellites, in particular a more thorough study of the sensor behavior is needed (i.e. before any image processing like the image linearization and rectification have been done). However, this is not a mandatory step when generating the TCDR of TOA outgoing radiation.

Chapter Two

Data selection and processing

The spectral ageing model, developed in this work, depends on three satellite dependent model parameters. In order to find these parameters, and this way characterise the shape of the ageing process for each satellite independently, time series are needed which show how the Meteosat visible (VIS) images change in time due to the in-flight degradation. In order to see the decreasing sensitivity clearly, the time series need to have as little variability[1] as possible. For that reason, the data used in this work to generate the spectral ageing model, is only a selection of the data available. This chapter explains how targets with a low variability in time are selected in the Meteosat field–of–view (FOV), how their time series are converted from digital count (DC) into so-called reflectance ratio values, and how these reflectance ratio time series are then grouped according to scene type to be of maximum use in this thesis.

2.1 METHOD

As explained in Chapter 1, the observed signal of the Meteosat VIS channel decreases in time due to the degradation. The spectral ageing model estimates how the instrument's spectral response (SR) curve changes due to this ageing process. As the observations have already been filtered by the real degrading SR, the model cannot be directly applied to the images. Instead, the incoming radiation is simulated and filtered by the modelled degrading SR to be able to compare observed degrading time series with the modelled ones. The images are then corrected using a reference which does not degrade in time, i.e. the unfiltered reflectance. This is the reflectance that would be observed by a non-degrading instrument with a perfect SR equal to 1 over the full wavelength range. The reason

[1] The variability refers to signal changes in time due to sources different than the ageing of the instrument.

why the full wavelength range is chosen for this simulated perfect instrument instead of the Meteosat Visible and Infrared Imager (MVIRI) VIS range, is partly to be able to see if it is possible to apply the model and create broadband observations, similar to the future Geostationary Earth Radiation Budget (GERB)-like data, and partly for reasons further on explained in Section 2.6. A linear relation exists between filtered and unfiltered reflectances. If the degradation in the observations is estimated correctly by the model, and so the right model parameters have been found, the same relation which converts the simulated degrading filtered reflectances into simulated non-degrading unfiltered reflectances, is able to convert the observed degrading reflectance time series into ageing corrected unfiltered reflectance time series.

As the search towards this best set of satellite dependent model parameters is based on how strongly the observed time series are still decreasing after adjusting the parameters, it is important to decrease the variability in the time series as much as possible. This way the residual trend in the data will be more clear and the model parameters can be better tuned with smaller uncertainties. For this reason, only a selection of sites in the Meteosat FOV is used. In the rest of this chapter, the data selection and the way the time series are processed in order to decrease the variability, is explained.

2.2 INPUT DATA

The data from the MVIRI used in this work, are the Level 1.5 VIS images. They have been generated by correcting the original (Level 1.0) images for unwanted geometric effects (i.e. rectification), and by geolocating them using the rectified fixed reference projection. First of all, only one VIS image a day is selected, i.e. the one at 1200 Universal Time Convention (UTC) when a maximum of pixels in the Meteosat FOV are in daylight. This image is reduced from the original size of 5000×5000 pixels to 2500×2500 pixels, mainly to average the output of the two detectors (see Table 1.4), but also to reduce the processing time. Whenever this image was corrupted or unavailable, nothing is used for this date. Secondly, not all pixels in the FOV are useful. The sun glint region is removed to avoid saturation. This is the region over ocean for which the angle between the direction of the solar specular reflection and the direction of observation is too small[2], i.e. in this study less than 25°. On top of that, some other sites are not stable enough in time for the study of the instrument degradation effects. This instability can be due to a change in land use over the years, like the deforestation of the Amazon

[2]This so-called sun glint angle (SGA) is computed as $\cos(\mathrm{SGA}) = \cos(\theta_0)\cos(\theta) + \sin(\theta_0)\sin(\theta)\cos(\psi)$, where the angles θ_0, θ and ψ were defined in Section 1.1.2.

rainforest or the urbanisation of land adjacent to cities that was previously used for agriculture (Lambin et al. 2001, 2003). Another reason can be dust in the atmosphere coming from e.g. the Sahara, which can cover parts of Europe and the Atlantic Ocean (Prospero & Carlson 1972, Papayannis et al. 2008), or other types of aerosols in the atmosphere (Chin et al. 2004, Edwards et al. 2004). As the intention is to see how the Meteosat data vary in time due to the degradation, it is necessary to reduce the noise on the time series as much as possible, and so only select a specific set of targets with a low variability in time to work with.

2.3 CONVERSION FROM DIGITAL COUNTS TO REFLECTANCE

Instead of using the original images expressed in DC to search for the targets with the lowest noise level, all useable 1200 UTC images are first converted into reflectance. The main reason for this is that values expressed in reflectance are not dependent anymore on the variable solar incoming radiation.

First, the original values v are converted into radiances L using a fixed calibration coefficient C and offset O

$$L = C\,(v - O). \tag{2.1}$$

The calibration coefficients and offsets used here, are the ones that were calculated using the SEVIRI Solar Channel Calibration (SSCC) at launch. These values are given on the webpage of the European Organization for the Exploitation of Meteorological Satellites (EUMETSAT) and are shown here in Table 2.1 for each of the 6 Meteosat First Generation (MFG) satellites. The calibration coefficient C is kept fixed at the value at launch, which means that the SSCC daily drift is not used. The offset O was measured by EUMETSAT for different periods in time by . The value given in Table 2.1 is the time average of all these offsets over the full life time of each satellite. The standard deviation on O that results from this averageing, is added in the table. This value is as small as 0.003 for the second part of Meteosat-3 due to the fact that only a limited amount of data are available, with offsets almost all equal to 4, and as high as 0.484 for Meteosat-4 where offset values were measured ranging from 4 up to 5.

Next, the radiances L are transformed into reflectances ρ through

$$\rho = \frac{L}{\frac{\mathrm{FSI}\,\cos\theta_0}{\pi\,d^2}}, \tag{2.2}$$

which is Eq. (1.4), but where the spectral radiance $L(\lambda)$ is multiplied with the instrument's SR $\phi(\lambda)$ and integrated over all wavelengths of the VIS MVIRI channel,

satellite	launch date	data period used at 0°	gain level	calibration coefficient	offset	drift per day	FSI
Meteosat-1	23/11/1977	09/12/1977 - 25/11/1979	/	/	/	/	/
Meteosat-2a	19/06/1981	12/02/1982 - 11/05/1987	0	0.652	3.729 ± 0.089	2.322	499.9
Meteosat-2b		12/05/1987 - 09/08/1988	1	0.545	3.686 ± 0.017	1.493	499.9
Meteosat-3a	15/06/1988	11/08/1988 - 18/06/1989	1	0.628	3.712 ± 0.049	3.547	602.2
Meteosat-3b		24/01/1990 - 09/12/1990	0	0.757	4.001 ± 0.003	3.928	602.2
Meteosat-4	06/03/1989	19/06/1989 - 03/02/1994	4	0.732	4.661 ± 0.484	5.239	599.5
Meteosat-5	02/03/1991	20/01/1994 - 03/02/1997	5	0.814	4.460 ± 0.126	2.992	690.6
Meteosat-6	20/11/1993	29/01/1997 - 13/06/1998	5	0.838	5.542 ± 0.081	3.944	691.4
Meteosat-7	02/09/1997	03/06/1998 - 11/07/2006	6	0.918	4.837 ± 0.136	5.351	690.8

Table 2.1: Table showing for each satellite the launch date, the used observation period at 0°, the gain level, the calibration coefficient at launch (in $\mathrm{W\,m^{-2}\,sr^{-1}}$ / DC), the time averaged offset value (in DC), the daily drift coefficient from the SSCC method (in $\mathrm{W\,m^{-2}\,sr^{-1}}$ / DC $\mathrm{day^{-1}}$ 10^5) and the filtered solar irradiance (in $\mathrm{W\,m^{-2}}$), as all found on the EUMETSAT webpage.

resulting in

$$L = \int_{\mathrm{VIS}} L(\lambda)\phi(\lambda)\mathrm{d}\lambda. \tag{2.3}$$

Similarly, $S(\lambda)$ is multiplied with $\phi(\lambda)$, resulting in the filtered solar irradiance (FSI) when integrated over all VIS wavelengths. The FSI values used here are the ones calculated by EUMETSAT using the fixed $\phi(\lambda)$ as it was characterised before launch (see Table 2.1 for the FSI values). As the radiances and reflectances from Eqs. (2.1) and (2.2) are filtered by the instrument's SR, they are sometimes referred to as filtered radiances and reflectances in the rest of this thesis.

The reflectance images are now used to select sites that have a low noise level in time. As the degradation of the VIS channel has proven to be spectrally dependent, it is useful to have sites with different spectral characteristics, which reflect the incoming solar radiation in different parts of the VIS spectrum. Comparing the degradation of each type of site should then show how the degradation spectrally evolves in time. The next two sections explain how the selection was done, making a distinction between the search for cloudy and clear-sky targets.

2.4 SELECTION OF CLOUDY TARGETS

As only clouds with a relatively high albedo can be detected in the VIS images, and the selected clouds need to have a low variability in time, the selection process is limited to either the low thick marine stratus and stratocumulus clouds or the deep convective clouds. For the following reasons, the convective clouds prove to be more suitable targets than the stratocumulus clouds. First of all, deep convective clouds have much higher and more stable reflectance values (close to 1) than the stratocumulus clouds (0.3 – 0.4), making the former easier to detect. Secondly, the tops of the deep convective clouds are at the tropopause level[3], reducing the effects of water vapour and tropospheric aerosol absorption, compared to the lower stratocumulus clouds. Finally, Eastman et al. (2011) observed a decrease in the amount of persistent marine stratocumulus clouds over several different regions during the past sixty years, presuming a positive feedback system with the increasing sea surface temperature. This makes these clouds bad study targets for this degradation work. Deep convective clouds were also used to calibrate instruments like the Advanced Very High Resolution Radiometer (AVHRR) and the Moderate Resolution Imaging Spectro-radiometer (MODIS) (Doelling et al. 2004).

[3]The tropopause is the boundary in the Earth's atmosphere between the troposphere and the stratosphere where a temperature inversion occurs. The part of the atmosphere that ranges from the Earth's surface up to the tropopause is called the troposphere, while the stratosphere is the region right above the tropopause.

The selection process for the convective clouds starts by replacing each pixel in the reflectance images with a local mean of the values in a box of 7×7 pixels around it. The reason why this is done, is the following. The surface of the top of the convective clouds is not always parallel to the Earth surface. This means that the $\cos\theta_0$ in Eq. (2.2) becomes too large when the angle between the incoming radiation beam and the cloud surface $\theta_{0,\mathrm{cloud}}$ is larger than the angle between the incoming radiation and the Earth surface θ_0. In the opposite case, $\cos\theta_0$ is too small. These two situations often happen next to each other, e.g. for a cloud lobe where the effect of the bright side faced to the Sun is canceled by the shadowy side turned away from the Sun. Averageing out the pixels in boxes, reduces these effects. Apart from that, this local averageing increases the stability of the time series of the candidate targets.

Next, each so-called local mean image is scanned for deep convective clouds: i.e. pixels with reflectance values close to 1. This search is not done over the whole FOV, but is limited to a box in the InterTropical Convergence Zone (ITCZ). This is the area around the equator where the northeast and southeast trade winds come together and result in uplifting air, creating big thunderclouds or, in other words, deep convective clouds. The region around the ITCZ that is used in this work is shown by the white box in Figure 2.1. The vertical range of this box is based on the fact that this is the region with the most deep convective clouds

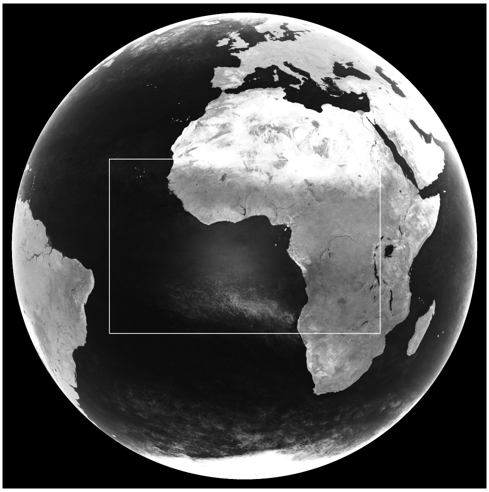

Figure 2.1: Figure showing the region around the ITCZ from which the selection of deep convective cloud sites is done.

in the Meteosat FOV, while the horizontal range allows to limit θ and avoid the edge of the FOV. Apart from this, only using this region also prevents from accidentally selecting the snowy clear-sky sites in the outer north and south of the disk, which also have reflectance values close to 1.

In the following step of the process, the full set of deep convective cloud pixels present in one local mean image, is reduced by requiring a minimal distance between each two candidate targets. Each final selected pixel needs to be the local maximum reflectance value in a box of 151×151 pixels surrounding it, so that no two cloudy targets are closer to each other than 75 pixels. This minimum distance requirement is set to increase the variety in the cloudy selection. Finally, the 6 targets with the highest reflectance values are averaged out, so that one convective cloud value is obtained per image (and thus per day).

2.5 SELECTION OF CLEAR-SKY TARGETS

In order to find clear-sky targets, the clouds need to be filtered out from the images, leaving only the clear-sky Earth below. These clear-sky images are created following the method of Ipe et al. (2003) with a temporal frequency of one image every 10 days[4]. The value of each clear-sky pixel is the fifth percentile of the time series of that pixel from 30 reflectance images before and 30 after. Taking the fifth percentile instead of the pixel to pixel minimum, serves to reduce the sensitivity to cloud shadows. The Meteosat-7 data are used in Figure 2.2 to illustrate this, with an example of an original image expressed in reflectance ρ in Figure 2.2(a) and its clear-sky counterpart in Figure 2.2(b).

Similarly as for the cloudy targets, the first step in the selection process of clear-sky targets is replacing each pixel in the clear-sky images with the local mean of the values in a box around it. The first reason for this is the same as before: the Earth surface is not always flat. Mountains, forests, cities, etc. can make the solar radiation reflect in a way that is not corrected for using the $\cos\theta_0$ in Eq. (2.2). Another reason is that there is a lot of diversity in the scene types present on the Earth. By averageing out, peaks of more reflecting or less reflecting surface types are reduced. For that reason, the local mean is taken here over a larger box (25×25 pixels) than for the convective clouds. Figure 2.2(c) shows the local mean image derived from Figure 2.2(b).

To know the spectral signature of each clear-sky pixel, a specific scene type is assigned to it. The spectral subdivision that is used for this, was defined by the scientists from the Clouds and Earth's Radiant Energy System (CERES) and

[4] The reason why the clear-sky images were derived this way instead of using the cloud mask is to avoid depending on other methods in the determination of the ageing process, as no other information than the VIS MVIRI images themselves are used in the method of Ipe et al. (2003).

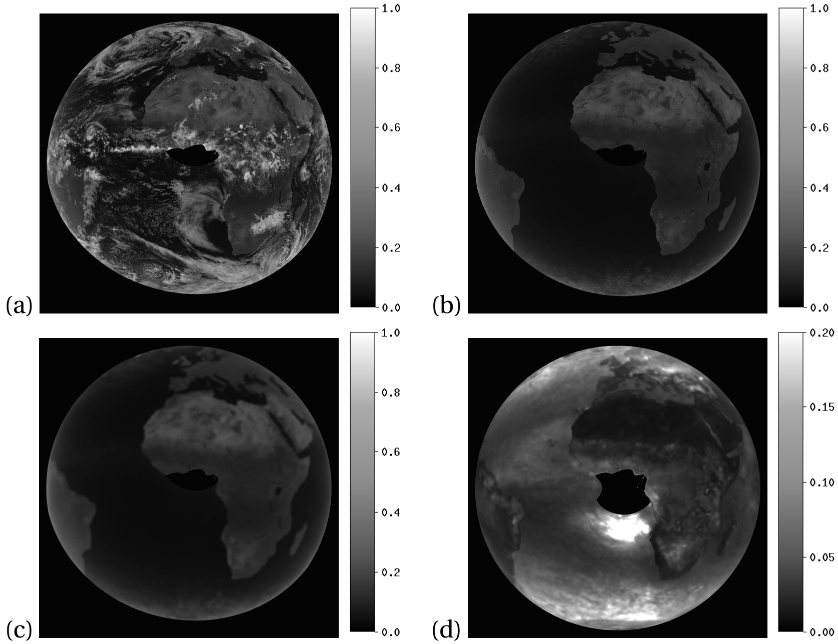

Figure 2.2: The Meteosat-7 VIS image of 10 June 2003 as (a) the reflectance image, (b) the clear-sky reflectance image, (c) the local mean reflectance image and (d) the standard deviation to mean ratio image of the full Meteosat-7 data range. The black spot in the center of these images is the sun glint region that has been removed.

is based on the International Geosphere / Biosphere Programme (IGBP) (Eidenshink & Faundeen 1994, Loveland & Belward 1997). Figure 2.3 shows the distribution of the 6 different scene types: ocean, dark vegetation, bright vegetation (i.e. sparse vegetation where the bright underlying soil is visible), dark desert, bright desert, and snow. As there are almost no all year round snow pixels in the Meteosat FOV, this surface type is not used in this work. Furthermore, the snow spectrum in the VIS band is very similar to the convective cloud spectrum (Dozier 1989).

In the next step, the clear-sky images are scanned for sites which have a low variability in time. To find these clear-sky targets, a criterion is needed to decide what noise level on the time series is low enough for this work. The criterion used here is based on the ratio of standard deviation to mean of each pixel time series over the full time range of a satellite, in the following way. As the decrease in sig-

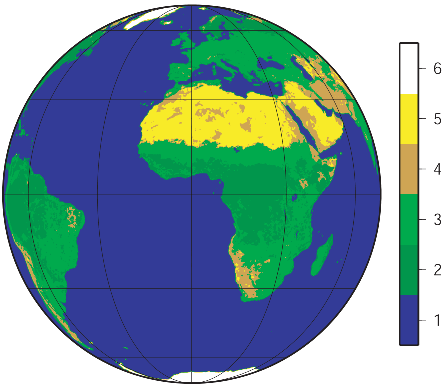

Figure 2.3: The different scene types used to classify the clear-sky targets: ocean (1), dark vegetation (2), bright vegetation (3), dark desert (4), bright desert (5) and snow (6)

nal of the satellite due to the ageing can be approximated to the first order by a linear function, a linear fit in time is computed for each individual reflectance clear-sky pixel time series. Based on this fit, the standard deviation to the fitting line is computed and stored for each pixel in a so-called standard deviation image. In the same way, the mean image is computed as the image where each pixel is the mean value of the pixels with the same position over the whole time range of images. Using these two images, the pixel to pixel ratio of the standard deviation to mean is taken in order to normalise the standard deviation. This standard deviation to mean ratio image for Meteosat-7 is shown in Figure 2.2(d). The candidate targets are then selected as the pixels with a normalised standard deviation smaller than 0.05.

To ensure that the final targets come from different geographical regions, and that the number of sites stays limited, the final step is again a distance limitation: no two sites with the same scene type can be located closer than 50 pixels, i.e. each site is the local minimum of standard deviation to mean ratio for its scene type in a box of 101×101 pixels. For the ocean sites, it is required that in this box of 101×101 pixels, at least 95% of the pixels are ocean sites. This is to prevent from selecting ocean sites too close to the shore or to small islands. All the targets that are retained after all these eliminations, are used in the rest of the work (see Figure 4.1 in Section 4.1). By performing the target selection this way, still a few hundred sites are left to work with. Another option could have been to only select a limited number of sites per scene type, of which the spectral information is well known, and it is known that these sites have a low degree of variability in time. Even though this would decrease the processing time, it limits the spectral information for each scene type individually. As it is important to know if the spectral ageing model works for sites over the full Meteosat FOV, it is useful to have targets spread out over all observed continents.

2.6 TIME SERIES IN REFLECTANCE RATIO UNITS

For each of these clear-sky and cloudy targets, reflectance time series are created. In order to apply the spectral ageing model $\phi(\lambda, t)$, these reflectance time series are unfiltered. The linear unfiltering relation, which converts the observed filtered reflectance ρ into unfiltered reflectance ρ_u (see Section 2.1), is given by the linear regression

$$\rho_u = a + b\rho. \tag{2.4}$$

The a and b coefficients are obtained by fitting simulated filtered and unfiltered reflectances, which are created as follows. Using the Santa Barbara DISORT Atmospheric Radiative Transfer (SBDART)[5] model (Ricchiazzi et al. 1998), spectral radiances $L(\lambda)$ are simulated for different geometries and scene types, for which the spectral signatures are obtained from Clerbaux et al. (2008). In total, 750 surface types are used in this work, which are characterised by a mixture of one or several surface reflectance models from the Advanced Spaceborne Thermal Emission and Reflection Radiometer (ASTER) library (Baldridge et al. 2009). Also, different types of aerosols and cloudiness are allowed. The simulations cover all possible solar and viewing geometries with an angular resolution of 10° for the solar zenith angle θ_0 and relative azimuth angle ψ, and 5° for the viewing zenith angle θ.

To convert the simulated spectral radiances $L(\lambda)$ into filtered and unfiltered radiances, the spectral ageing model $\phi(\lambda, t)$ is used for the filtered radiances L and a flat SR function $\phi(\lambda) = 1$ for the unfiltered radiances L_u. With a sufficiently fine spectral resolution, the filtered radiances are calculated as

$$L = \int_{\mathrm{VIS}} L(\lambda)\phi(\lambda, t)\,\mathrm{d}\lambda \tag{2.5}$$

where the integration covers the full MVIRI VIS channel, and the unfiltered radiances as

$$L_u = \int_{0.25-5\,\mu\mathrm{m}} L(\lambda)\,\mathrm{d}\lambda. \tag{2.6}$$

[5] The Discrete Ordinates Radiative Transfer (DISORT) model is a multi-layered plane-parallel radiative transfer code applicable to problems from the ultraviolet (UV) to the radar regions of the electromagnetic spectrum.

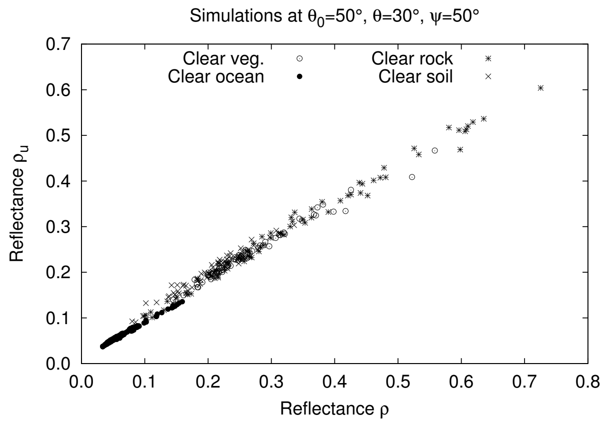

Figure 2.4: Simulated filtered and unfiltered reflectances for different surface types and with angles $\theta_0 = 50°$, $\theta = 30°$ and $\psi = 50°$. The filter that is used for the filtered reflectances in this example is the one of Meteosat-7 at launch.

After both filtered and unfiltered simulated radiances are converted into filtered and unfiltered reflectances, using Eq. (2.2) with $d = 1$ as the simulations have been performed at 1 Astronomical Unit (AU), the coefficients a and b are fitted for each geometry, time step t and scene type for which the simulations were done, through Eq. (2.4). Figure 2.4 shows a sample of simulated filtered and unfiltered reflectances for four different surface types and for the geometry angles $\theta_0 = 50°$, $\theta = 30°$ and $\psi = 50°$. The filtered reflectances shown in this figure were created using the Meteosat-7 SR curve at launch ($t = 0$). The fitted a and b coefficients are then used to convert, for each scene type, geometry and time, the observed filtered reflectance time series into unfiltered reflectance time series. If the degradation is modelled correctly, this results in stable, non-degrading time series.

As a final step, the unfiltered reflectances ρ_u are divided by a modelled anisotropy factor R and albedo A to correct for the difference in Sun-Earth-satellite geometry and albedo for the different surface types. For the clear-sky sites, R and A are provided by the angular distribution models (ADMs) that have been empirically estimated by Loeb et al. (2003), using data of the CERES instrument on the Tropical Rainfall Measuring Mission (TRMM) (Kummerow et al. 1998)[6]. As the CERES short wave band is broader than the VIS MVIRI chan-

[6] The availability of these broadband CERES models is also the reason why the unfiltering is done for Meteosat and why no other stable reference is used.

nel, the cloudy R and A contain the effects of the deep ice and water absorption bands between 1–2 μm. For this reason the anisotropy and albedo models for deep convective clouds are not taken from Loeb et al. (2003). Instead they are modelled with the radiative transfer program libRadtran (Mayer & Kylling 2005) using the Key et al. (2002) ice crystal parameterisation, assuming solid column shaped particles. The result of the division of the observed unfiltered reflectances by these modelled broadband reflectances is called the reflectance ratio r, given by

$$r = \frac{\rho_{\mathrm{u}}}{R(\theta_0, \theta, \psi)\ A(\theta_0)} \tag{2.7}$$

in which the dependency on the angles θ_0, θ and ψ is now expected to be removed.

In the most perfect situation, the r values should be equal to 1. In practice this is, for different reasons, not the case. First of all, the Meteosat SR curve on which the spectral ageing model is based, is not perfect, with possibly larger uncertainties for the older instruments when the characterisation was done less accurately than nowadays. In Chapter 6 a study is done, showing that even the SR characterisation of the VIS channel of Meteosat-7 is not perfect. Secondly, the unfiltering correction relies on simulations which may not exactly represent the observed surface type. The final reason is that the CERES TRMM ADMs used to convert the unfiltered reflectance values ρ_{u} into reflectance ratio r, are not perfect for this use here. As they are global tropical models, they are adequate as an average over the tropical region (latitude between 35°S and N), but might slightly misrepresent targets in the Meteosat FOV. The deficiency of the CERES TRMM models in the Meteosat FOV was reported for dark vegetation by Bertrand et al. (2006). On top of that, the ADMs depend on the CERES calibration, while Meteosat and CERES have not been intercalibrated. Also, there can be sampling errors in these ADMs: when calculating the R and A values, averages were taken over boxes, subdivided per angle. This introduces some variability on these values, which enters the reflectance ratio time series.

2.7 SEASONAL CORRECTION

In the previous step, when the unfiltered reflectance values were converted into reflectance ratio, a division was made for each observation by an empirical anisotropy factor and albedo value (Eq. (2.7)). As explained, these values were not derived from the same FOV which is covered by the Meteosat satellites, but come from observations over the tropical region. This results, among other

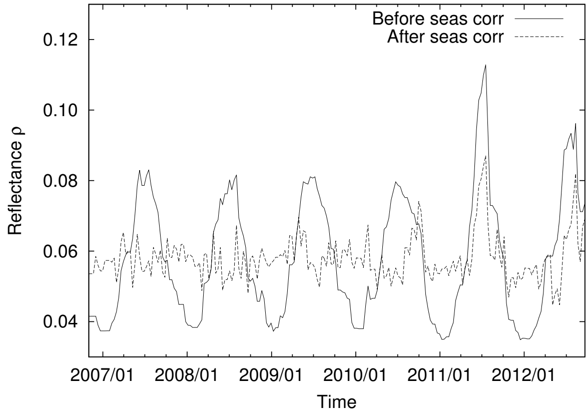

Figure 2.5: Ageing corrected Meteosat-7 time series for a site in the Indian Ocean with latitude 37.26° S and longitude 41.30° E, both before and after the seasonal correction.

things, in residual seasonal effects[7] which are empirically corrected in this work by subtracting the difference between the monthly mean annual cycle and the overall mean from the reflectance ratio time series (Qian et al. 2011). As the original time series decrease in time due to degradation, and this degradation can be approximated to the first order by a linear relation, the mean values are calculated with respect to a linear first order fit. An example of an ageing corrected time series of a site with high seasonal variation is shown before and after seasonal correction in Figure 2.5 for a site in the Indian Ocean (observed during the Indian Ocean Experiment (INDOEX) and Indian Ocean data coverage (IODC)). Due to the fact that a minimum of two cycles is necessary to calculate these correction factors (due to the linear fit), a minimal duration of 2 years of continuous data is required in this work to do the seasonal correction.

2.8 SCENE TYPE AVERAGEING

Finally, the seasonally corrected clear-sky reflectance ratio time series are averaged out according to the 5 different surface types used in this work (ocean, dark vegetation, bright vegetation, dark desert and bright desert). The reason for this

[7] Another source of seasonal effects is the seasonal changing of vegetation cover or leaf area. By using a lot of targets, this effect is averaged out.

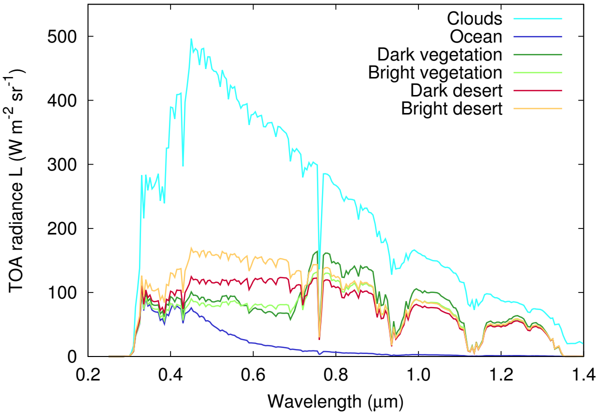

Figure 2.6: Simulated average spectral radiance curves at the TOA for the 6 different scene types used in this work. The spectra come from Clerbaux et al. (2008).

is the following. First, the grouping is done to decrease the number of time series to work with while at the same time still keeping information about the whole Meteosat FOV. Second, the stability is increased by averageing out the somewhat more noisy time series. And finally, the ageing effect is stronger for scene types with a strong component in the blue part of the VIS spectrum. By selecting the sites with the same surface type, similar spectral characteristics are being grouped together and targets with distinct spectral properties can be compared with each other. The sixth time series, i.e. the convective cloud time series, is averaged out over 10 days to have the same temporal resolution as the clear-sky time series. As each value in the original cloud time series already was the mean of 6 targets, the time averaged cloud time series contain the averages of 60 deep convective cloud observations every 10 days.

For each of the 6 scene types, Figure 2.6 shows typical TOA outgoing spectral radiance curves $L(\lambda)$. These clearly show the different spectral characteristics of the different scene types, where each reflects different amounts of radiation in the different wavelengths. In Table 2.2, the mean wavelength in which each of the 6 scene types reflects its energy is calculated, weighted by the spectra shown in Figure 2.6. The second column shows the mean wavelengths following

$$\langle\lambda\rangle = \frac{\int L(\lambda)\,\lambda\,\mathrm{d}\lambda}{\int L(\lambda)\,\mathrm{d}\lambda},$$

Table 2.2: Weighted average wavelengths of each of the 6 spectra from Figure 2.6, with and without filter.

Scene type	$\langle\lambda\rangle$	$\langle\lambda\rangle_{\text{filtered}}$
Clouds	0.7338	0.6665
Ocean	0.5129	0.5638
Dark vegetation	0.8611	0.7299
Bright vegetation	0.8887	0.7205
Dark desert	0.8735	0.6912
Bright desert	0.8421	0.6801

while the values shown in the third column are filtered using the pre-launch characterised Meteosat-7 SR curve:

$$\langle\lambda\rangle_{\text{filtered}} = \frac{\int L(\lambda)\,\phi(\lambda)\,\lambda\,\mathrm{d}\lambda}{\int L(\lambda)\,\phi(\lambda)\,\mathrm{d}\lambda}.$$

Both columns show that the ocean spectrum reflects on average in the lowest wavelengths, followed by the deep convective clouds, the desert, and the vegetation. By multiplying the spectra with the SR curve of Meteosat-7, the mean wavelengths change as the weighting shifts to the wavelength region where the SR observes most radiation (roughly between 0.4 and 1.1 µm). This means that the contributions of both the parts of the spectra for the shortest wavelengths (0.3 – 0.4 µm) and the longest wavelengths (1.1 – 1.4 µm) become almost negligible in the calculations. For the ocean, this results in a higher mean wavelength when filtering, because the ocean spectrum peaks in the shortest wavelengths, while for the other scene types, the mean wavelength becomes smaller as these scene types still reflect a lot of radiation in the higher wavelength region.

Chapter Three

Spectral ageing model

Right before the satellite is launched, when no degradation should have[1] taken place yet, it is assumed that the spectral response (SR) curve of the Meteosat Visible and Infrared Imager (MVIRI) resembles the one that was measured by the spacecraft manufacturer. After the satellite is launched into space, degradation starts, though it is unknown at what exact point this happens. As more and more contamination blocks the radiation from reaching the detectors, the SR of the instrument starts to decrease, resulting in a degraded SR curve $\phi(\lambda, t)$ at a certain time t, expressed in days since launch. In this chapter, the different attempts that led toward the creation of the spectral ageing model are shown, giving the formula of the model itself, and presenting the three parameters the model relies on. It is explained at the end of this chapter how these parameters are fitted for each satellite.

3.1 CREATING THE MODEL

3.1.1 LINEAR DEGRADATION

In the most simple case, the decrease of the SR can be approximated by a linear function in time,

$$\phi_1(\lambda, t) = \phi(\lambda, 0)\ (1 - \alpha t),$$

where $\phi(\lambda, 0)$ is the SR curve of the instrument as it was characterised before launch, and α the parameter that represents the degradation rate of the instrument. As there is no spectral dependency assumed in this model, one speaks of 'grey degradation'. It is known, however, that there is a spectral component to

[1]There is a precedent (Global Ozone Monitoring Experiment (GOME)) where degradation already happened before launch, during storage. This is, however, a rare case.

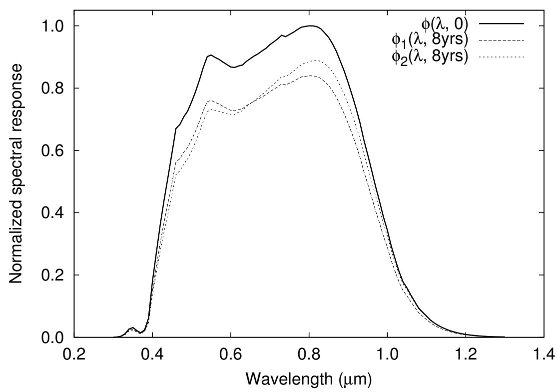

Figure 3.1: Normalised SR curves of the Meteosat-7 VIS channel at launch and after 8 years, using models $\phi_1(\lambda, t)$ and $\phi_2(\lambda, t)$. The model parameters used for these curves are the ones leading to time series as stable in time as possible.

the ageing of the visible (VIS) channel of the Meteosat First Generation (MFG) instruments. Adding a factor to the model $\phi_1(\lambda, t)$, which is on itself also a linear dependency on time, results in the quadratic time dependent model

$$\phi_2(\lambda, t) = \phi(\lambda, 0)\ (1 - \alpha t)\left(1 + \gamma(\lambda - \lambda_0)t\right),$$

where $\gamma(\lambda - \lambda_0)$ represents the spectral degradation rate of the instrument, i.e. the rate at which the optical properties of the contamination are changed, and λ_0 is the central wavelength of the SR curve at launch $\phi(\lambda, 0)$. The tilt around λ_0 in this function shows how, for a positive γ value, the blue part of the spectrum ($\lambda < \lambda_0$) is allowed to decrease more than the red part of the spectrum ($\lambda > \lambda_0$).

The difference between $\phi_1(\lambda, t)$ and $\phi_2(\lambda, t)$ is shown in Figure 3.1, based on the SR curve at launch of the Meteosat-7 VIS channel. The full line shows the original $\phi(\lambda, 0)$, while the other two curves are the degraded modelled SRs after 8 years, using $\alpha = 0.000055$ days^{-1} for the first model, and $\alpha = 0.000050$ days^{-1} and $\gamma = 0.000125$ days^{-1} µm^{-1} for the second. These parameters are the best possible ones, i.e. the parameters that lead to 6 reflectance ratio time series as flat as possible[2]. The reason why α is bigger for the first model than for the second, can be explained like this. In the grey model, α is taken as the value that leads all time series as close as possible to flat ones. Knowing that there is a spectral degradation, and that the model tries to find the best solution for all time series (and

[2]The way these parameters are found is explained in the Section 3.2.

thus all parts of the spectrum), $\phi_1(\lambda, t)$ is overcompensating in the red part, and not correcting enough in the blue part of the spectrum. Adding the γ parameter shows that the overall ageing is in fact not so strong, but that the spectral part is needed to correct the blue ocean time series more than the red desert ones.

3.1.2 Exponential grey degradation

Based on the research from Matthews et al. (2005) and Xiong et al. (2009), and the National Aeronautics and Space Administration (NASA) studies performed by Stewart et al. (1990) and Tribble et al. (1996), the grey part in the ageing model is now changed from a linear degradation to an exponential one

$$\phi_3(\lambda, t) = \phi(\lambda, 0)\, \mathrm{e}^{-\alpha t} \left(1 + \gamma(\lambda - \lambda_0)\, t\right) \tag{3.1}$$

where α is still the grey degradation rate and $\gamma(\lambda - \lambda_0)$ the spectral one. Although the visual difference between the SR curves seems to be negligible in Figure 3.2 for the two models after 8 years, the exponential grey degradation is easier to substantiate physically than the linear one. Assuming for now that the contaminated surfaces do not reflect radiation anymore, at each time t it can be said for any part of the surface of the mirrors and detectors that it either reflects radiation or it does not. If, in this case, the contamination arrives at these sensitive surfaces at a constant rate α, the amount of contamination-free surface decreases exponentially in time, following $e^{-\alpha t}$. Consequently, the amount of visible radiation

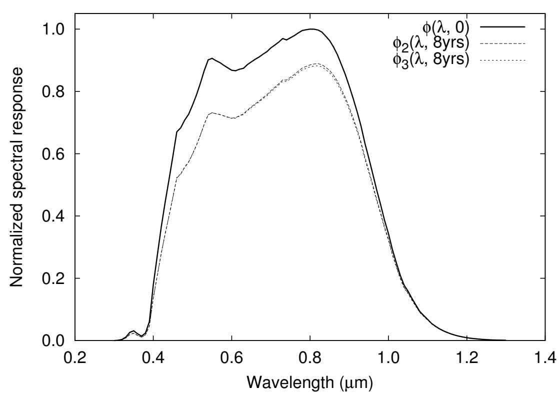

Figure 3.2: Normalised SR curves of the Meteosat-7 VIS channel at launch and after 8 years, using models $\phi_2(\lambda, t)$ and $\phi_3(\lambda, t)$. The model parameters used for these curves are the ones leading to time series as stable in time as possible.

captured at the detectors, decreases at the same rate, as the contaminated surfaces absorb all incident radiation. The model parameters used in Figure 3.2 for $\phi_2(\lambda, t)$ are the same as in Figure 3.1, and for $\phi_3(\lambda, t)$, $\alpha = 0.000050$ days^{-1} and $\gamma = 0.000115$ days^{-1} µm^{-1}. This means that the overall grey degradation rate stays the same, with a slightly smaller spectral one.

For the spectral part of the degradation model, different possibilities were investigated. In the case of the Clouds and Earth's Radiant Energy System (CERES), Matthews et al. (2005) proposed a model with an exponential dependency on wavelength. This idea is based on the fact that atomic oxygen is a major source of contamination for polar orbiting instruments (Dooling & Finckenor 1999). Polar satellites, like the ones carrying the CERES instruments, fly on altitudes where there is enough atomic oxygen in the atmosphere to cause degradation effects. The Meteosat instruments in their geostationary orbits, however, are too high up in space to be bothered by this. The material causing the degradation for geostationary instruments is thus not the same as for satellites in polar orbits and so the model of CERES could not be followed. An exponential decrease in time could have worked, but it was not supported by any other works and it did not lead to significantly better results.

In the three models that were discussed here, it was assumed that the contaminated parts of the mirrors and detectors do not reflect any light anymore because the contamination absorbs it all. If this would be the case, the reasoning behind the spectral degradation as being caused by the contamination absorbing more short wave radiation (and so reflecting less) than long wave radiation, would be nonsense. To incorporate the fact that the contaminated parts of the surfaces still reflect part of the incoming radiation, the model is changed even further, becoming the spectral ageing model used in the rest of this work.

3.1.3 SPECTRAL AGEING MODEL

In the last model ($\phi_3(\lambda, t)$), the sensitivity goes to 0 when the whole surface is contaminated. In reality some amount of radiation is indeed absorbed, but the majority is still reflected and captured by the detectors. In this work, the fraction of radiation reflected by the contaminated surfaces, is represented by the parameter β. Adding this to $\phi_3(\lambda)$, leads to the following model

$$\phi(\lambda, t) = \phi(\lambda, 0)\left(e^{-\alpha t} + \beta\left(1 - e^{-\alpha t}\right)\right)\left(1 + \gamma(\lambda - \lambda_0)t\right). \tag{3.2}$$

Here $e^{-\alpha t}$ represents the signal due to the non-contaminated parts of the mirrors and detectors, while $\beta\left(1 - e^{-\alpha t}\right)$ is the part that represents the fraction of incoming light still reflected by the contaminated surfaces. Figure 3.3 shows the original SR curve $\phi(\lambda, 0)$ of Meteosat-7 together with the modelled response

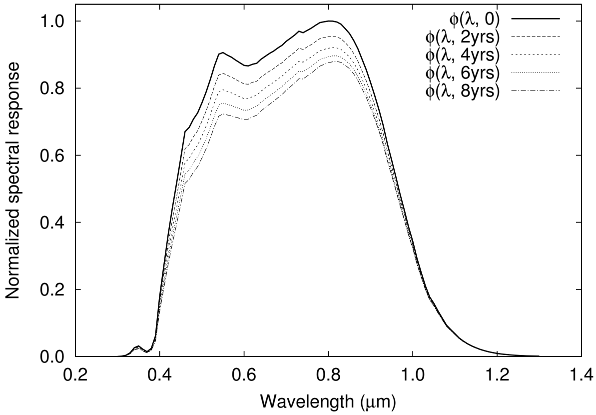

Figure 3.3: Normalised SR functions of the Meteosat-7 VIS channel at launch, and after 2, 4, 6 and 8 years. The model parameters used for these curves are the ones leading to time series as stable in time as possible, and are given in Table 4.2.

curves using the spectral ageing model for $t = 2$, 4, 6 and 8 years. The model parameters used in this figure are $\alpha = 0.000357$ days^{-1}, $\beta = 0.760112$ and $\gamma = 0.000126$ days^{-1} μm^{-1} (as given in Table 4.2)[3].

3.2 PARAMETER FITTING

Next, the three model parameters α, β and γ need to be estimated for each MFG satellite. In Section 2.1, it was already stated that, if the degradation in the data is estimated correctly by the model, the same relation which converts the simulated degrading filtered reflectances into simulated non-degrading unfiltered reflectances, is able to convert the observed degrading filtered reflectance time series into ageing-corrected flat unfiltered reflectance time series. With the modelled SR curve $\phi(\lambda, t)$ from Eq. (3.2), the simulated filtered radiance from Eq. (2.5)

[3] The reason why α is much bigger here than in the previous model is due to the fact that in reality the signal does not go to zero, but saturates to a certain value. To model this with Eq. (Mod3), α had to be much smaller due to the absence of the β parameter.

becomes

$$\begin{aligned} L &= \int_{\mathrm{VIS}} L(\lambda)\phi(\lambda,t)\mathrm{d}\lambda \\ &= \int_{\mathrm{VIS}} L(\lambda)\phi(\lambda,0)\left(\mathrm{e}^{-\alpha t}+\beta\left(1-\mathrm{e}^{-\alpha t}\right)\right)\left(1+\gamma(\lambda-\lambda_0)t\right)\mathrm{d}\lambda \\ &= \left(\mathrm{e}^{-\alpha t}+\beta\left(1-\mathrm{e}^{-\alpha t}\right)\right)\left(L_0+\gamma t L_0'\right) \end{aligned} \tag{3.3}$$

with

$$\begin{aligned} L_0 &= \int_{\mathrm{VIS}} L(\lambda)\phi(\lambda,0)\mathrm{d}\lambda \\ L_0' &= \int_{\mathrm{VIS}} L(\lambda)\phi(\lambda,0)(\lambda-\lambda_0)\mathrm{d}\lambda. \end{aligned}$$

The simulated unfiltered radiance stays independent of the instrument's SR curve:

$$L_{\mathrm{u}} = \int_{0.25-5\mu\mathrm{m}} L(\lambda)\mathrm{d}\lambda. \tag{3.4}$$

For a certain set of (α, β, γ) parameters, the unfiltering from Eq. (2.4) can be fitted for each scene type using the simulated filtered and unfiltered reflectances derived from the simulated filtered and unfiltered radiances of Eq. (3.3) and (3.4). If that set of parameters is able to convert the observed filtered reflectance ratio time series into flat unfiltered reflectance ratio time series using the same fits from the simulations, then the model is able to estimate the degradation in the data and the right parameters have been found. That best set of parameters is found through the minimisation process of Powell (1964), which requires an initial value and search vector as input for each parameter. The algorithm works through a bi-directional search for each of the parameters, starting at the initial value in a direction normal to one of the axes of the parameter space, using the initial step size, and working its way towards the parameters which minimise the cost function C. This function is the mean square variance of the six (observed) unfiltered time series with respect to the mean u_i:

$$C = \sum_{i=1}^{6} w_i \left(\frac{1}{N}\sum_{j=1}^{N}\left(r_{ij}-u_i\right)^2\right) \tag{3.5}$$

where index i runs over the 6 time series and index j over all points in the time series, w_i is the weight given to each of the 6 scene types, N is the number of points in the time series (which is the same for each scene type) and r_{ij} is the reflectance ratio for time series i and time j. The weights w_i for the clear-sky

Surface type	weight w_i
Convective clouds	0.6562
Ocean	0.1611
Dark vegetation	0.0252
Bright vegetation	0.0554
Dark desert	0.0268
Bright desert	0.0753

Table 3.1: For each time series, the weight used in Eq. (3.5) is given.

scene types are equal to the percentage of pixels of that scene type in the Meteosat field–of–view (FOV). For the clouds, the weight was obtained from the number of pixels in the FOV with a cloud fraction equal to 1, averaged out over several days. The cloud fraction is retrieved from the Spinning Enhanced Visible and Infrared Imager (SEVIRI) images. The values for the weights w_i are given in Table 3.1 for each surface type. Figure 3.4 shows the value of the cost function for different combinations of the three model parameters (slope, β, γ) for the Meteosat-7 data. The lowest values are situated within a wide V-shape in the slope-β plane, with decreasing values towards the corner of the V. In Section 4.2 it is shown that the Powell routine is indeed able to find the local minimum that is shown in Figure 3.4.

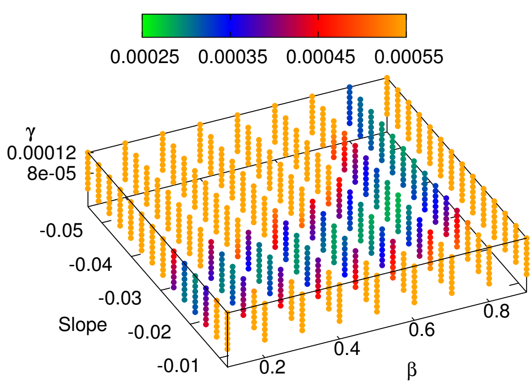

Figure 3.4: A color map showing the value of the cost function in the 3 dimensional parameter space (slope, β, γ).

In the minimisation process, the parameter α is replaced by the slope s, through

$$s = \alpha\,(1-\beta)$$

which is the first derivative of the grey part of the degradation model $e^{-\alpha\, t} + \beta\left(1 - e^{-\alpha\, t}\right)$ at $t = 0$. The reason for this replacement is that, for short time series, the saturation of the drift is not yet visible, and so it is difficult to know if either α and β are both big or both small. The slope, however, will always stay the same, and becomes a more reliable, and numerically stable, variable in that case. The whole minimisation routine is summarised in the following roadmap:

1. Simulate the spectral radiance $L(\lambda)$ for different scene types, cloudiness types and geometries
2. Set the model parameters (s, β, γ) to an initial value
3. Calculate L and L_u using Eqs. (3.3) and (3.4) with the given values for s, β and γ
4. Convert these simulated radiances into reflectances using Eq. (2.2)[4]
5. Do the unfiltering through Eq. (2.4), fitting the a and b values for these simulated reflectance values
6. Use this fit to convert the observed reflectances ρ into unfiltered reflectances ρ_u (Eq. (2.4))
7. Transform ρ_u to reflectance ratio r using Eq. (2.7)
8. Calculate Eq. (3.5)
9. If the variance is not yet the lowest possible, the Powell routine returns a new set of (s, β, γ) parameters and goes back to step 3.

[4] In Eq. (2.2), FSI is kept constant in the same way as was done for the observations and d is kept fixed at 1 as the simulations have been made at $d = 1$.

Chapter Four

Model applied to Meteosat-7

In the previous chapter, a model was postulated, showing how the spectral response (SR) curve of the visible (VIS) channel of the Meteosat Visible and Infrared Imagers (MVIRIs) changes in time and wavelength. Together with the mathematical formula of the model, a way was presented to derive the three satellite dependent model parameters. In the next phase, these parameters need to be determined. In doing so, it will be possible to check the validity of the model assumptions. Meteosat-7 was part of the Meteosat Transition Programme (MTP) of the European Organization for the Exploitation of Meteorological Satellites (EUMETSAT) to fill the gap between the Meteosat First Generation (MFG) and Meteosat Second Generation (MSG) of instruments. Built similarly as its predecessors, the satellite was operational at the nominal position at 0° longitude for 8 years (June 1998 – July 2006). This long time period makes the Meteosat-7 dataset an ideal test case. In this chapter, the model is applied to Meteosat-7 as explained before. The 6 time series are shown, both before and after ageing correction, and the model is validated. In the end, a theoretical comparison study is made between the spectral ageing model and the SEVIRI Solar Channel Calibration (SSCC), based on the retrieval of 5 essential climate variables (ECVs).

The results shown in Sections 4.1, 4.2, and 4.3 have been published in Decoster et al. (2013), while the results from Section 4.4 are in preparation for publication.

4.1 ORIGINAL TIME SERIES

Figure 4.1 shows the positions of the 298 clear-sky targets, which were found as explained in Section 2.5, using the Meteosat-7 dataset. Averageing out these 298 time series according to the 5 clear-sky scene types (ocean, dark vegetation, bright vegetation, dark desert and bright desert), and adding the one time series for the deep convective clouds, results in the 6 time series which are shown in

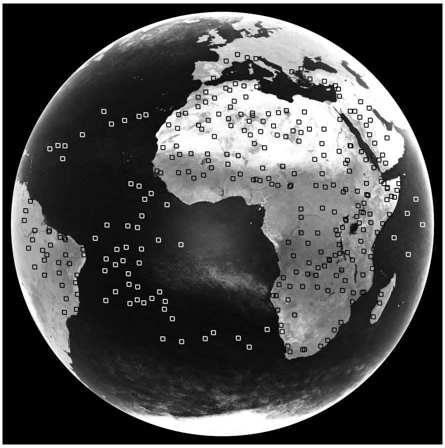

Figure 4.1: Figure showing the position of the 298 selected clear-sky targets for the Meteosat-7 dataset.

Figure 4.2(a) before seasonal correction and Figure 4.2(b) after. The first thing to remark is that, as explained in Section 2.6, the initial reflectance ratio values differ from 1 for four of the six time series. Apart from that, the small difference in degradation rate for each of the time series can be seen in the figure (e.g. when comparing the bright desert with the ocean and cloudy time series). The dark and bright vegetation decrease with 1.4 % per year while the dark and bright desert decrease with 1.55–1.7 % per year. The ocean time series decrease with about 1.85 % per year, and the deep convective cloud time series with slightly more than 1.9 % per year. The exact numerical values of these relative slopes are given in column 4 of Table 4.1, together with their standard deviation. The explanation of how the latter are calculated, is given in the Appendix. The weighted mean slope and standard deviation are added at the bottom of the table.

As both the ocean and the convective clouds reflect most radiation in the blue part of the VIS wavelength range (see Figure 2.6), their slightly stronger decrease in time corroborates the wavelength-dependency of the degradation process of Meteosat-7. A stronger degradation is expected for the ocean than for the deep convective clouds due to the nature of the spectral degradation (strongest for the shortest VIS wavelengths), and because the ocean reflectance spectrum peaks in somewhat shorter wavelengths than the one of the convective clouds. Even though this stronger decrease for the ocean than for the convective cloudy time series is not visible in the unfiltered reflectance ratio time series, it should be for the filtered version of the data, where the unfiltering step is left out and

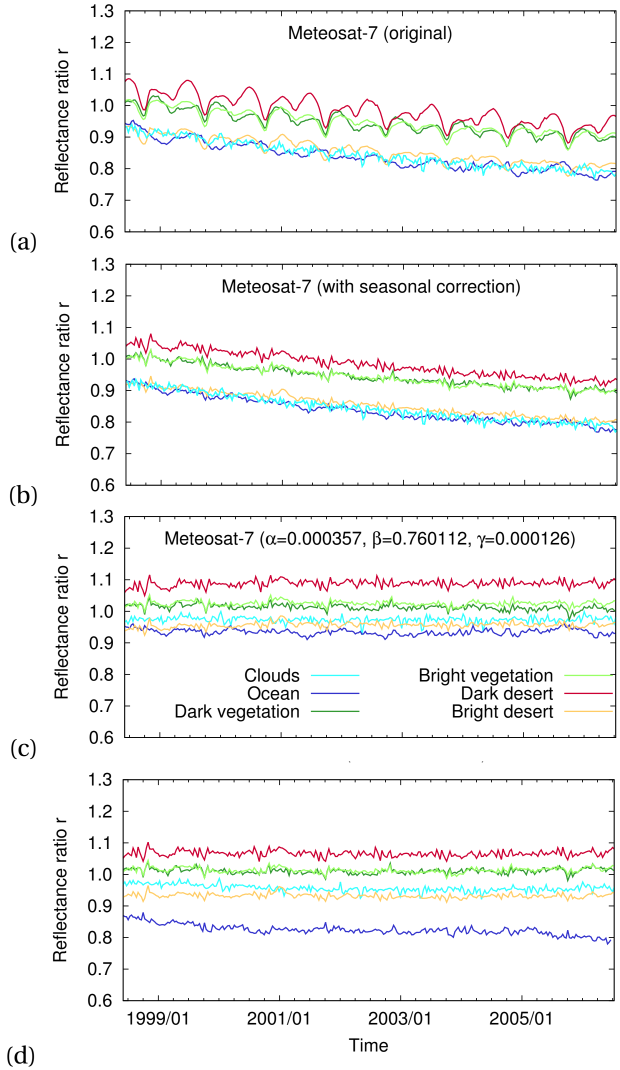

Figure 4.2: Meteosat-7 reflectance ratio time series for (a) the original time series, (b) after seasonal correction, (c) after ageing correction using the parameters $\alpha = 0.000357\,\mathrm{day}^{-1}$, $\beta = 0.760112$ and $\gamma = 0.000126\,\mu\mathrm{m}^{-1}\mathrm{day}^{-1}$, and (d) after being corrected using the SSCC method.

surface type	number of time series	weight w_i	slope of original time series (% yr^{-1})	slope of spectrally corr. time series (% yr^{-1})	slope of SSCC corr. time series (% yr^{-1})
convective clouds	60	0.6562	-1.9143 ± 0.0273	-0.0265 ± 0.0234	-0.2324 ± 0.0237
ocean	55	0.1611	-1.8698 ± 0.0285	-0.0613 ± 0.0241	-0.6198 ± 0.0287
dark vegetation	57	0.0252	-1.4012 ± 0.0221	-0.1729 ± 0.0196	-0.0054 ± 0.0208
bright vegetation	102	0.0554	-1.4073 ± 0.0215	-0.0076 ± 0.0193	-0.0125 ± 0.0204
dark desert	47	0.0268	-1.5427 ± 0.0226	0.0826 ± 0.0235	-0.0350 ± 0.0223
bright desert	37	0.0753	-1.6924 ± 0.0195	0.0814 ± 0.0207	-0.0790 ± 0.0193
total sum	299	1.00			
weighted average			-1.8394 ± 0.0263	-0.0237 ± 0.0230	-0.2601 ± 0.0239

Table 4.1: For each surface type, the number of sites used in this work is given, together with the weight values used in the cost function (Eq. (3.5)), the percentage that the slope of the reflectance ratio time series changes per year, and its standard deviation, both for the original ones and the spectrally corrected ones, and for the reflectance ratio time series corrected for grey ageing using the SSCC method of Govaerts et al. (2004). The explanation of how the standard deviations on the slopes are calculated, is given in the Appendix.

the filtered reflectances are immediately divided by a filtered anisotropy factor R and albedo A (see Eq. (2.7)). The reason for this difference in slope between the filtered and unfiltered versions of the blue time series, is to be found in the unfiltering conversion

$$\rho_\mathrm{u} = a + b\,\rho$$

itself. As there is no filtered (narrowband) anisotropy factor and albedo available, only theoretical proof can be given. For easy reading, in the following explanation, the unfiltered time series will be indicated with r_u and ρ_u like before, while the filtered versions are written as r_f and ρ_f instead of r and ρ.

Using Eq. (2.7) to rewrite the unfiltering conversion as a function of reflectance ratio instead of reflectance (with $\widetilde{\rho} = R(\theta_0,\theta,\psi)\,A(\theta_0)$), leads to

$$\tilde{\rho}_\mathrm{u}\,r_\mathrm{u} = a + b\,\tilde{\rho}_\mathrm{f}\,r_\mathrm{f}. \tag{4.1}$$

By taking the partial derivative of this equation with respect to time, and assuming the temporal change of a and b small enough to ignore in this calculation, the slopes of the reflectance ratio time series arrive into the equation:

$$\tilde{\rho}_\mathrm{u}\frac{\partial r_\mathrm{u}}{\partial t} = b\,\tilde{\rho}_\mathrm{f}\frac{\partial r_\mathrm{f}}{\partial t}. \tag{4.2}$$

To get the relative change of the reflectance ratio time series, Eq. (4.2) is divided by the unfiltering conversion (Eq. (4.1)),

$$\begin{aligned}
\frac{\tilde{\rho}_\mathrm{u}\,\frac{\partial r_\mathrm{u}}{\partial t}}{\tilde{\rho}_\mathrm{u}\,r_\mathrm{u}} &= \frac{b\,\tilde{\rho}_\mathrm{f}\,\frac{\partial r_\mathrm{f}}{\partial t}}{a + b\,\tilde{\rho}_\mathrm{f}\,r_\mathrm{f}}\left(\frac{r_\mathrm{f}}{r_\mathrm{f}}\right)\\
\frac{\frac{\partial r_\mathrm{u}}{\partial t}}{r_\mathrm{u}} &= \frac{b\,\tilde{\rho}_\mathrm{f}\,r_\mathrm{f}}{a + b\,\tilde{\rho}_\mathrm{f}\,r_\mathrm{f}}\left(\frac{\frac{\partial r_\mathrm{f}}{\partial t}}{r_\mathrm{f}}\right)\\
&= \frac{1}{1 + \frac{a}{b\,\tilde{\rho}_\mathrm{f}\,r_\mathrm{f}}}\left(\frac{\frac{\partial r_\mathrm{f}}{\partial t}}{r_\mathrm{f}}\right)\\
&= \frac{1}{1 + \frac{a}{b\,\rho_\mathrm{f}}}\left(\frac{\frac{\partial r_\mathrm{f}}{\partial t}}{r_\mathrm{f}}\right).
\end{aligned}$$

Filling in typical values for the filtered reflectances ρ_f for both ocean and convective clouds, and the a and b coefficients for these scene types for typical angles $\theta_0 = 30°$, $\theta = 30°$ and $\psi = 90°$, leads for the deep convective cloud time series to

$$\frac{1}{1 + \frac{a}{b\,\rho_\mathrm{f}}} = \frac{1}{1 + \frac{0.04}{0.9 \times 0.7}} \approx 0.94$$

and for the ocean time series to

$$\frac{1}{1+\frac{a}{b\rho_f}} = \frac{1}{1+\frac{0.014}{0.94\times 0.1}} \approx 0.87.$$

Filling in the values for the unfiltered slopes, shows that indeed the slope of the filtered ocean time series is more strongly negative than the slope of the filtered deep convective cloud time series.

4.2 CORRECTED TIME SERIES

Starting with a set of plausible model parameters, the road map that was given at the end of Chapter 3 can now be followed to minimise the cost function of Eq. (3.5). The parameters that come out of this minimisation process are given in Table 4.2, together with the value of the minimised standard deviation of the cost function, which is added at the bottom of the table. To have an idea on the precision of these parameters, the standard deviation on each value is computed by running the same minimisation technique on 30 different random subsets of 100 from the 299 available time series. As there is only one convective cloud time series, no subset can be taken here. Instead, 3 different time series are created by taking once the 6 highest cloudy pixels to average out per day (as usual), once the 5 highest, and once the 4 highest. These three time series are randomly added to the 30 subsets in such a way that each subset contains 1 convective cloud and 99 clear-sky time series. For each of these 30 subsets, slightly different model parameters are obtained. The standard deviation in the last column of Table 4.2 is the standard deviation of these 30 values. The significant non-zero value for the γ parameter indicates the need for a wavelength-dependent correction of degradation for Meteosat-7.

Table 4.2: The optimal solution is given for each parameter together with their standard deviation. At the bottom, the value of the minimised standard deviation of the cost function is shown.

parameter	units	optimal solution
s	day^{-1}	-0.000085 ± 0.000003
α	day^{-1}	0.000357 ± 0.000032
β	/	0.760112 ± 0.022055
γ	µm^{-1} day^{-1}	0.000126 ± 0.000013
std. dev.	/	0.015875 ± 0.003464

Filling in this set of model parameters into the spectral ageing model, leads to the corrected time series shown in Figure 4.2(c). When comparing Figures 4.2(b) and (c), one thing that can be seen, apart from the fact that the time series are now all quasi horizontal, is that the starting points of the six time series in Figure 4.2(c) are slightly higher than the ones in Figure 4.2(b). The reason for this is that in the spectral ageing model (Eq. (3.2)), the starting point $t = 0$ is the moment of launch (September 1997 in this case) while the dataset used here only starts in June 1998 when the instrument became operational at the nominal position. The percentage that the slope of each of these time series changes per year is given in column 5 of Table 4.1. These values confirm the anticipated improvement as they are now all clearly smaller than the original ones. The residual standard deviation for each individual time series is again calculated as shown in the Appendix, and added to the table. The resulting corrected SR curves were already shown in Figure 3.3 for $t = 2$, 4, 6 and 8 years.

4.3 VALIDATION OF THE MODEL

To prove that the spectral ageing model performs well, it is validated, based on the Meteosat-7 data. In a first step, the spectral ageing model is applied to random all-sky sites, where different scene types are grouped together to create time series. The result of this regional validation is shown in Section 4.3.1. The second validation is based on the full dataset of the International Geosphere / Biosphere Programme (IGBP). Instead of grouping the clear-sky targets into 5 groups[1], the 17 classes of the IGBP are used as scene type subdivision. The method and residual slopes of the 17 time series are given in Section 4.3.2. At the end, in Section 4.3.3, the SSCC method is applied to the same 6 time series as used before, to see the difference with the spectral ageing model for the Meteosat-7 data.

4.3.1 REGIONAL VALIDATION

The two keys to the regional validation are that, first of all, instead of only the selected targets, all pixels in the original reflectance images are corrected for ageing. Apart from that, the unfiltering of Eq. (2.4) is now fitted using all-sky simulations[2] as the full original images are used instead of only the clear-sky images. To do the correction, all pixels are converted from filtered reflectance to unfiltered reflectance, using the model parameters from Table 4.2. As there are no all-sky angular distribution models (ADMs) (only for strictly clear-sky or cloudy pixels),

[1] The sixth group, i.e. the deep convective clouds, is not used in this validation step.

[2] These simulations are also created using the Santa Barbara DISORT Atmospheric Radiative Transfer (SBDART) model, allowing all types of clouds.

(a) 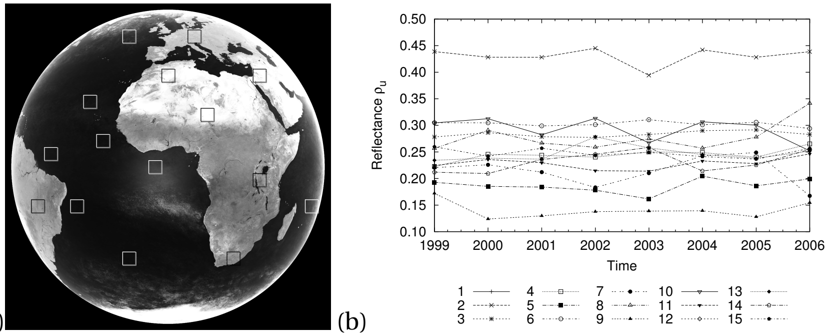 (b)

Figure 4.3: (a) The position of the random selection of 15 boxes of 100×100 pixels, and (b) their yearly averaged reflectance time series.

the division by R and A is not possible, and thus the unfiltered reflectance values are not converted into reflectance ratio as before.

To show the results, the Meteosat field–of–view (FOV) is divided into 25×25 boxes, each with a size of 100×100 pixels. In each box, the unfiltered reflectance values are averaged out and used to create time series. As each box contains 10 000 pixels, this means that different scene types are combined in each time series. In order to show some of the time series, first, a few random boxes are selected for which the positions and sizes are shown in Figure 4.3(a). As the unfiltered reflectance values are not converted into reflectance ratio, the pixels are not corrected for differences in surface reflection throughout the seasons. To mitigate these seasonal effects, yearly averages are taken. The resulting time series are shown in Figure 4.3(b).

Next, the residual slopes of the time series are computed. This is done for all 401 of 625 boxes that are in the Meteosat FOV and satisfy the condition $\theta < 80°$ and $\theta_0 < 80°$. The spatial distribution of the residual slopes per year are shown in Figure 4.4(a). Figure 4.4(b) gives the slopes as a function of their mean reflectance, where the error bars are their standard deviations. This figure shows that the slopes are all grouped around zero with a few extreme values going as high as 0.007 ± 0.0017 in the North Atlantic Ocean and at the East coast of Brazil. To find the reason for this, the monthly mean Moderate Resolution Imaging Spectro-radiometer (MODIS) (Terra) Level 3 'cloud fraction' atmospheric product is used (MOD 08_M3) for the period of 1 March 2000 until 31 December 2006. The cloud fraction is originally expressed as a value between 0 and 10 000, but is rescaled here to a value between 0 and 1. For each of the 360×180 pixels[3], a lin-

[3]This MODIS product is delivered with a pixel resolution of 1°.

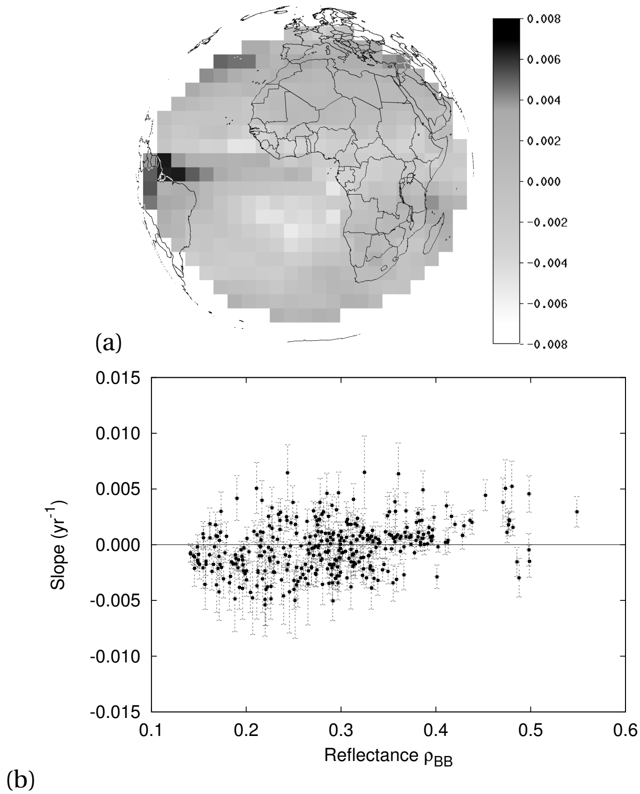

Figure 4.4: Results of the regional validation. (a) Spatial distribution of the residual slopes, where the values are expressed per year. (b) Residual slopes per year as a function of mean reflectance.

ear least squares fit is made through the cloud fraction data for the full time period. Figure 4.5 shows the slopes per year of these fits. A cloud fraction increase of about 0.01 yr^{-1} is detected by MODIS in the North Atlantic Ocean region, as can be seen in the figure. The increasing reflectance of 0.007 ± 0.0017 yr^{-1} can be explained by this in the following way. On average, a cloud fraction C equal to 1 corresponds to a mean reflectance ρ of 0.8, while a cloud fraction of 0 corresponds to a clear ocean reflectance of 0.05. This means that, on the whole, $\Delta\rho/\Delta C = 0.75$. Using this ratio together with the observed cloud fraction slope

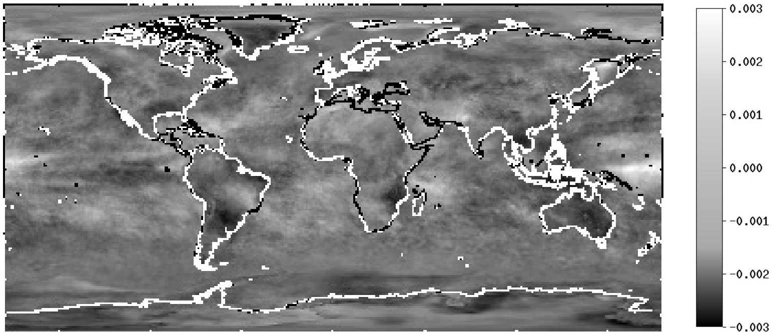

Figure 4.5: The slope per year of the cloud fraction, measured by MODIS over the period of 03/2000 – 12/2006.

of 0.01 yr^{-1}, leads to a predicted

$$\Delta\rho = \frac{\Delta\rho}{\Delta C}\,\Delta C = 0.75 \times 0.01\ \mathrm{yr}^{-1} = 0.0075\ \mathrm{yr}^{-1}, \tag{4.3}$$

which is within error margins equal to the observed reflectance increase of $0.007 \pm 0.0017\ \mathrm{yr}^{-1}$. The standard deviation σ of the reflectance slopes is equal to $0.0022\,\mathrm{yr}^{-1}$, with 95% of the boxes having a slope between $-0.0042\,\mathrm{yr}^{-1}$ and $0.0045\,\mathrm{yr}^{-1}$ (about $\pm 2\sigma$, proving a Gaussian error distribution). Using a daily averaged flux of $100\,\mathrm{W\,m^{-2}}$ and a daily averaged reflectance of 0.3, the reflectance standard deviation can be translated into a flux stability of about 7 $\mathrm{W\,m^{-2}}$ / decade. This value is clearly higher than the Global Climate Observing System (GCOS) requirement ($0.2\ \mathrm{W\,m^{-2}}$ / decade), but as shown in the following, most of this apparent trend over 8 years is due to cloud variability.

For comparison, the same procedure is now applied to the clear-sky images instead of the original ones (still using the all-sky simulations). Figure 4.6(a) shows the spatial distribution of the residual slopes for all boxes, while Figure 4.6(b) gives the slope as a function of their mean reflectance, where each box still consists of 100×100 pixels. As there are no more clouds adding to the variability, it is normal that the results are better with smaller error bars. The few slopes with larger standard deviations in Figure 4.6(b) come from parts in the FOV with permanent stratus and stratocumulus clouds, where it was not possible to totally remove the presence of clouds using the clear-sky procedure (e.g. at the west coast of Africa). To compare with the validation on the original images, the standard deviation σ is smaller (about 0.0006), with about 95% of the boxes having a slope between $-0.0014\,\mathrm{yr}^{-1}$ and $0.0012\,\mathrm{yr}^{-1}$ (again about $\pm 2\sigma$). This results in a stability of about $2\,\mathrm{W\,m^{-2}}$ / decade (using a mean flux of 100 $\mathrm{W\,m^{-2}}$

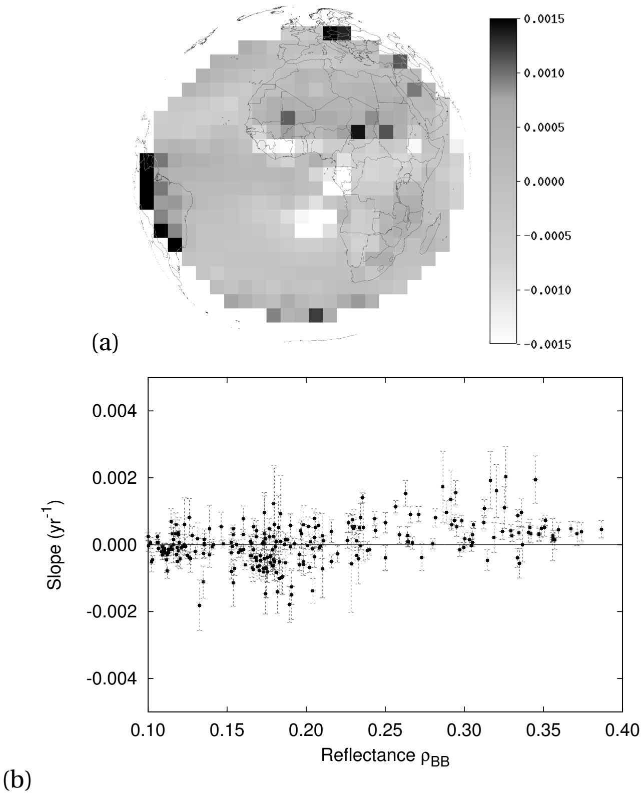

Figure 4.6: Results of the regional validation for the clear-sky images only. (a) Spatial distribution of the residual slopes, where the values are expressed per year. (b) Residual slopes per year as a function of mean reflectance.

and a mean ρ of 0.3). Part of this observed trend might still be attributed to the clear-sky processing.

4.3.2 IGBP surface type selection

In a second validation, the 17 class land cover dataset created by the IGBP Data and Information System is used. The 298 clear-sky targets are now subdivided based on these 17 classes (instead of the 5 Clouds and Earth's Radiant Energy System (CERES) classes before). 17 time series are created, where all pixels with the same surface type are averaged out into one time series, and a linear fit is

Table 4.3: For each IGBP scene type, the percentage of these surface types present in the Meteosat FOV is given, together with the slope per year of the fit through each time series and the standard deviations on the slopes.

Scene	name	% of scenes	slope (% yr^{-1})
1	Evergreen Needleleaf Forest	0.505	-0.0155 ± 0.1247
2	Evergreen Broadleaf Forest	0.440	-0.1015 ± 0.0262
3	Deciduous Needleleaf Forest	0.003	-0.3025 ± 0.2212
4	Deciduous Broadleaf Forest	0.250	0.0696 ± 0.0498
5	Mixed Forest	0.146	0.1625 ± 0.0622
6	Closed Shrublands	0.763	-0.1217 ± 0.0253
7	Open Shrublands	2.874	0.0607 ± 0.0226
8	Woody Savannas	4.162	-0.1867 ± 0.0319
9	Savannas	5.698	-0.0208 ± 0.0244
10	Grassland	2.262	0.0779 ± 0.0320
11	Permanent Wetlands	0.070	0.0088 ± 0.0590
12	Croplands	2.273	0.1263 ± 0.0541
13	Urban and Built-up	0.021	0.1214 ± 0.0441
14	Cropland Mosaics	4.415	0.0612 ± 0.0286
15	Snow	0.000	NA
16	Bare Soil and Rocks	9.601	0.0922 ± 0.0214
17	Water Bodies	62.26	0.1148 ± 0.0300

made through each of these 17 time series. The residual slopes (expressed in percentage per year) and the standard deviations on the slopes are given in Table 4.3. As there are barely any pixels with snow all year round in the Meteosat FOV, surface type number 15 is left out. The slopes are comparable to the values that were given in Table 4.1, giving extra validation of the spectral ageing model.

4.3.3 SSCC MODEL APPLIED TO TARGETS

In the final validation part, instead of using the spectral ageing model, the SSCC calibration of Govaerts et al. (2004) is applied to the 299 selected target time series. Figure 4.2(d) shows the same 6 clear-sky and cloudy time series that were used to create the spectral ageing model, but instead of correcting them for ageing following the spectral ageing model, and keeping the calibration coefficient constant, the SSCC method is used, where the calibration coefficient changes linearly in time, following

$$C_f(t) = C_f + (D_f N_t \times 10^{-5})$$

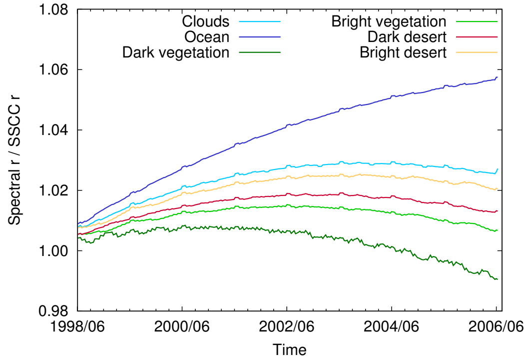

Figure 4.7: Figure showing the ratio of the reflectance ratio values corrected using the spectral ageing model to the reflectance ratio values corrected using the SSCC calibration method.

where C_f is the fixed calibration coefficient at launch (= 0.9184 $\mathrm{W\,m^{-2}\,sr^{-1}DC^{-1}}$ for Meteosat-7), D_f is the daily drift (= $5.3507 \times 10^5\,\mathrm{W\,m^{-2}\,sr^{-1}DC^{-1}day^{-1}}$ for Meteosat-7) and N_t is the number of days since launch. The first thing that should be noticed when comparing Figures 4.2(c) and (d), is that the ocean time series is still decreasing in the latter, while the others are not. This is as expected due to the fact that the wavelength-dependency in the degradation was not taken into account in the SSCC calibration. Moreover, most of the time series bend down a little in the middle of the curve, making them not perfectly horizontal. The reason for this is that the SSCC method assumes a linear decrease in time, and although this corrects the majority of the degradation, as mentioned before in Chapter 1, the validation work of SSCC showed saturation in the degradation which makes the ageing look more exponential than linear. Figure 4.7 shows the ratio of the 6 time series corrected using the spectral ageing model (Figure 4.2(c)) to the 6 time series corrected using the SSCC method (Figure 4.2(d)). Both the effect of the still decreasing SSCC corrected ocean time series and the bending are clearly visible here: the ratio of spectrally to SSCC corrected time series keeps increasing for the ocean time series, while for the others it increases in the beginning and decreases again in the second part of the time period, resulting in the bend.

4.4 COMPARISON STUDY OF THE SSCC AND SPECTRAL AGEING METHODS

4.4.1 METHODOLOGY

In this section, a theoretical comparison is carried out between the spectral ageing model and the official SSCC calibration, applied on the SR curve of Meteosat-7. The effect of both methods on the retrieval of 5 different ECVs, (aerosol optical depth (AOD), land surface albedo, cloud optical depth (COD), incoming surface flux and top of the atmosphere (TOA) outgoing VIS broadband radiance) is investigated and compared through the use of simulations. Like before, spectral TOA radiances $L(\lambda)$ are generated using radiative transfer models (RTMs), but this time for one specific geometry only, i.e. $\theta_0 = 30°$, $\theta = 30°$, $\psi = 90°$. These simulations are integrated over the spectral range of the Meteosat-7 VIS channel, taking into account its SR. This results in the radiances

$$L = \int_{\mathrm{VIS}} L(\lambda)\,\phi(\lambda, 8\mathrm{yrs})\,\mathrm{d}\lambda \tag{4.4}$$

where $\phi(\lambda, 8\mathrm{yrs})$ is the SR curve of the MVIRI VIS channel, modelled for 8 years of degradation. Even though Meteosat-7 was the only satellite that was actually operational for 8 years at 0° longitude, from Table 1.3 it can be seen that this time period is representative of the mean operational lifetime of the Meteosat satellites. By using the ageing degraded SR curves at $t = 8$yrs, the comparison is done for a case with sufficient ageing. The radiances from Eq. (4.4) are simulated using either the spectrally degraded SR curve or the SR degraded using the SSCC calibration. Both ageing modelled curves are shown in Figure 4.8. Next, for each of the 5 ECVs discussed hereafter, the difference between the simulated radiances generated using the SSCC degraded SR curve and the radiances simulated using the spectrally degraded SR are computed and the relation between these radiances and the ECV itself is shown. This so-called radiance bias $\Delta L = L_{\mathrm{SSCC}} - L_{\mathrm{spec}}$ is then converted into the ECV bias, ΔECV, through

$$\Delta\mathrm{ECV} = \frac{\Delta L}{\partial L / \partial \mathrm{ECV}} \tag{4.5}$$

where $\partial L/\partial$ECV is the local slope to the simulated data. This way, the difference between the use of one or the other SR curve for the retrieval of each ECV can be calculated and compared.

To generate the simulations, two different RTMs are used: SBDART and libRadtran. The main difference in the use of both models in this part of the work, is the fact that the SBDART simulations add some natural variability. This can be explained as follows. The same 750 SBDART simulations that were used before

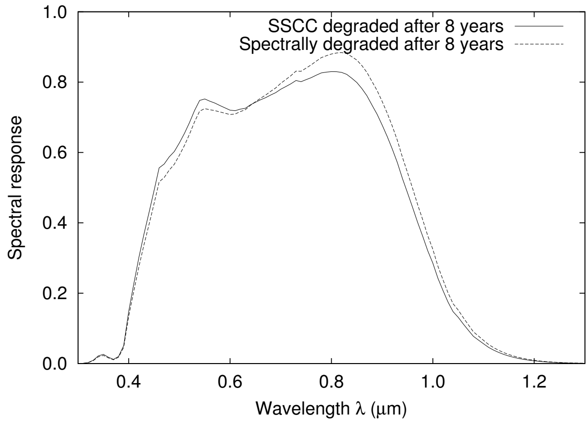

Figure 4.8: SR curves of the Meteosat-7 VIS channel, modelled for 8 years of degradation using the SSCC calibration method (solid line) and the spectral ageing model (dashed line).

in the unfiltering process (Section 2.6), are used here. They were made for different surface types, amounts of aerosols, types of aerosols, amounts of clouds present, types of clouds present, etc. For each of the ECVs for which these simulations are useful, subdivisions are made in these 750 simulations, depending on the variable for which the comparison is made for. These subdivisions can be, for example, into different scene types or different types or amounts of aerosols, or clouds. In each of these groups, some variability has been introduced by the random modification of the input parameters characterising the scene (atmospheric profile, aerosol type, cloud cover, surface type, wind speed, etc.). This variability then gives an idea on the significance of the ECV bias. Whenever these simulations did not allow to investigate a particular ECV, libRadtran was used to model the behavior of the ECV with respect to the two sets of degraded radiance values. In these simulations, only one parameter is changed at a time, so that the simulations, the trends, and the differences between the SSCC and the spectrally degraded SR curves are much clearer, but there is no 'natural' noise on the data.

In the following, for each of the 5 ECVs, the impact of using the spectrally corrected SR function instead of the SSCC corrected one is analysed and discussed separately, where each time it is clearly indicated which of the two RTMs is used.

4.4.2 AEROSOL OPTICAL DEPTH

Aerosols are solid particles suspended in the Earth's atmosphere, which can arrive there both by natural causes (desert dust, volcanic ashes, etc.) and by human activities (exhaust fumes from cars or industry, biomass burning smoke, etc.). They have the effect of absorbing and scattering visible radiation, and producing brighter clouds, which reflect even more solar radiation[4] but release less efficient precipitation[5]. Therefore, it is not surprising that aerosols have a strong impact on the Earth's radiative balance, and so that it is very useful to know the effect of any type and amount of particles in the atmosphere. One of the properties of aerosols that can be measured from satellites using only one channel in the VIS spectrum (like with the MVIRI instrument), is the AOD, which describes the degree to which visible light is attenuated[6] in the Earth's atmosphere by these aerosols, either through scattering of the radiation or through absorption of it. The most reliable AOD values are retrieved when the clouds and their shadows are removed from the images. These observed clear-sky radiances are then compared to radiance values simulated for the same clear-sky conditions and underlying surface type, but for different possible AOD values. Interpolation from these AOD look-up tables (LUTs) then provides the right AOD for the observation.

Ocean retrieval

AOD retrieval works best over clear ocean as its albedo is very small, and it is somewhat easier to simulate surface reflectance spectra over ocean than over land. Of the 750 SBDART simulations, 379 do not contain clouds and 153 of them were made above ocean. The latter are shown in Figure 4.9 after they were filtered by either the SSCC degraded or the spectrally degraded SR. Two different trends are visible in the figure, which is due to the different types of boundary layer[7] aerosols used: the simulations made with rural, oceanic and tropospheric aerosols result in the upper trend (see Figure 4.10(a)) while the urban aerosols

[4]This is due to the effect aerosols have on the formation of cloud particles. Aerosols can act as cloud condensation nuclei, resulting, for a fixed water content, in more but smaller cloud particles, which increase the reflectance.

[5]The precipitation efficiency is defined as the ratio of the precipitation rate to the sum of all precipitation sources (Li & Gao 2012), which decreases due to the increased number of (small) cloud droplets.

[6]The amount of radiation that passes through the aerosol layers present in the atmosphere, decreases exponentially with AOD (e^{-AOD}), but can be approximated by a linear function for AOD values smaller than 1.

[7]The boundary layer is the part of the troposphere that is directly influenced by the presence of the Earth's surface.

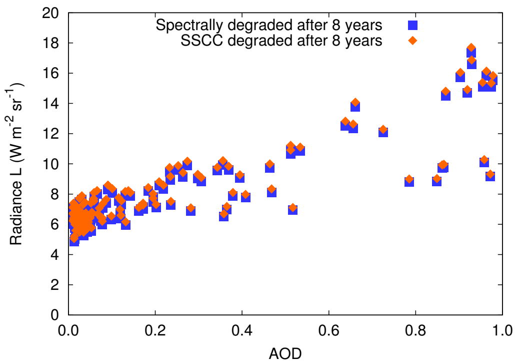

Figure 4.9: Simulated radiances as a function of AOD for clear-sky ocean conditions, made using the SBDART code.

lead to the lower trend (see Figure 4.10(c)). The following discussion is subdivided into these two groups.

By looking at the upper trend (Figure 4.10(a)), it can be seen that for a fixed AOD value, the spectrally degraded SR curve leads to smaller radiances L than the SSCC degraded one. This is explained by the fact that the former has a lower sensitivity in the blue (where the aerosols reflect most solar light) than the latter (see Figure 4.8), and so will observe less of the radiance reflected by the aerosols. From Figure 4.10(a) the direct proportionality between L and AOD is clear. As linear fits can be made through the data points, the local slope that is needed to convert the radiance bias ΔL into ΔAOD (see Eq (4.5)), stays fixed over the full AOD range. For each of the three aerosol types (rural, oceanic and tropospheric), the slopes of their fits are given in the third column of Table 4.4, together with their standard deviations, and the standard deviation of the linear fits in the fourth column. As for each aerosol type the slopes of the two fits are the same (within error margins), their mean value is used in Eq. (4.5). Figure 4.10(b) shows ΔAOD as a function of AOD. For all three aerosol types, the bias starts between 0.02 and 0.03 for small AOD values, but slightly increases for the rural and tropospheric aerosols, while it slightly decreases for the oceanic ones. The reason for this difference must lie in the reflectance spectrum of these aerosols. If ΔAOD decreases with increasing AOD, so does ΔL. This means that the spectrally degraded radiances increase more strongly with AOD than the SSCC degraded ones, which is confirmed by the values from Table 4.4. From Figure 4.8 it can then be deduced that the spectrum of the oceanic aerosols must have a stronger component in the longer wavelengths than the rural and tropospheric

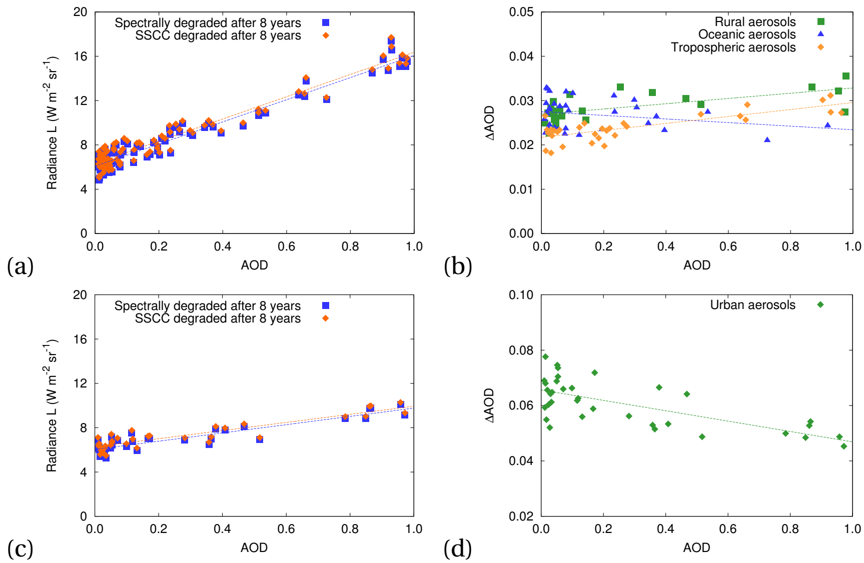

Figure 4.10: Simulations for clear-sky ocean conditions, made using the SBDART code, for (a)–(b) rural, oceanic and tropospheric aerosols, and (c)–(d) urban aerosols. The left sided images show the relation between the simulated radiances and the AOD, while the right side shows the relation between the AOD bias and AOD.

Table 4.4: The slopes and their standard deviations of the linear fits made through the L(AOD) data for both degraded SR curves, and the four different aerosol types. The standard deviation of the fits are also given.

Aerosol type	SR	slope $(\mathrm{W\,m^{-2}sr^{-1}})$	standard deviation $(\mathrm{W\,m^{-2}sr^{-1}})$
Rural	SSCC	9.228 ± 0.415	0.675
	Spectral	9.173 ± 0.407	0.663
Oceanic	SSCC	9.096 ± 0.598	0.748
	Spectral	9.133 ± 0.580	0.725
Tropospheric	SSCC	11.097 ± 0.409	0.700
	Spectral	11.010 ± 0.400	0.685
Urban	SSCC	3.663 ± 0.293	0.544
	Spectral	3.733 ± 0.285	0.529

aerosols (Ricchiazzi et al. 1998). The same procedure is now followed for the urban aerosols. Figure 4.10(c) shows that for these type of particles too, for an observed radiance L, the retrieved AOD is larger for the spectrally degraded radiances than for the SSCC degraded ones. Table 4.4 shows the fitted slopes, from which the mean is used to convert ΔL to ΔAOD. The AOD bias is shown in Figure 4.10(d) as a function of AOD. Similarly as for the oceanic aerosols, ΔAOD decreases with increasing AOD, pointing to a reflectance spectrum which has a stronger component in the longer wavelengths than the shorter.

The following can be concluded for the AOD retrieval over ocean. Even though the (random) retrieval uncertainty, estimated as the standard deviation of the fits divided by their slope ($\approx$0.07), is larger than the bias on AOD ($\approx$0.03), ΔAOD is a systematic uncertainty, which is positive for all aerosol types, is relatively constant over the AOD range between 0 and 1, and is of the order of the background AOD ($\approx$0.05). This means that the spectral ageing affects most of all the retrieval of background aerosols but also, to decreasingly smaller extent, the aerosols with higher AOD values.

Land retrieval

Over land, the method of retrieving AOD from satellite data is more difficult as the observed radiances are a combination of light reflected by the aerosols and light reflected by the underlying land surface type. As long as the albedo is low enough (< 20%), a method can be followed which compares clear-sky observations with and without aerosols, where in the latter the aerosols have been manually removed from the images. The radiance difference between these two is then used to retrieve the right AOD value from the LUTs. This method was used e.g. by Knapp et al. (2002, 2005) and Mei et al. (2011). If, however, the albedo of the land is too high, the absorbing properties of aerosols result in a lower outgoing visible radiance. This is for instance the case over desert or snow, where this method does not work.

As the SBDART simulations were made using different settings of surface type, amounts and types of aerosols or clouds, it is not possible to compare clear-sky simulations made for the same surface conditions, but for varying amounts of aerosols using this RTM. LibRadtran is used instead to simulate clear-sky TOA radiances above one type of desert and one type of vegetation, allowing a whole range of AOD values. Figure 4.11(a) shows in light blue the surface reflectance of the desert type used from the Advanced Spaceborne Thermal Emission and Reflection Radiometer (ASTER) spectral library (sandstone). The other curves are the TOA spectral radiances $L(\lambda)$, simulated through the RTM and converted here for comparison into reflectance spectra $\rho(\lambda)$, for three different AOD values. This confirms that, over desert, the reflectance decreases with an increasing amount of aerosols. This is also clear from Figure 4.11(b).

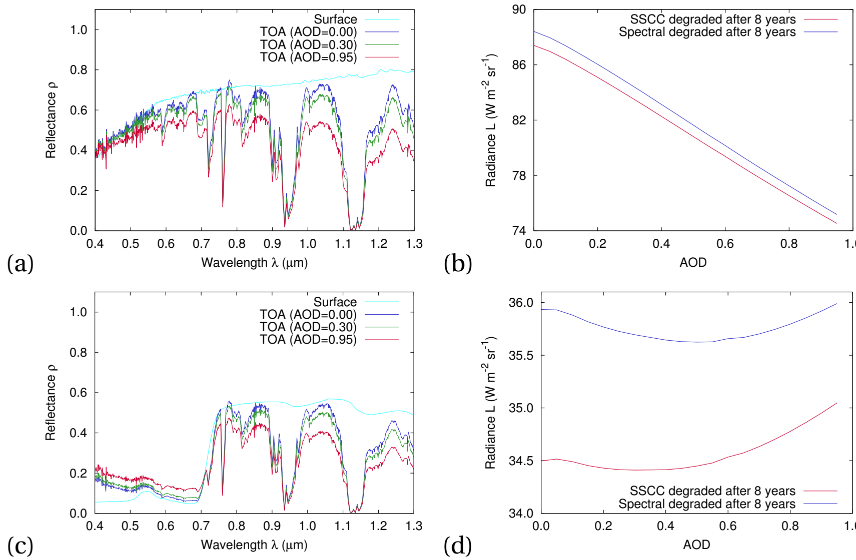

Figure 4.11: LibRadtran simulations for default aerosol settings and clear-sky conditions. (a) Sandstone desert reflectance spectra at the surface and at the TOA for different AODs. (b) Simulated radiance as a function of AOD over sandstone surface. (c) Deciduous vegetation reflectance spectra at the surface and at the TOA for different AODs. (d) Simulated radiance as a function of AOD over deciduous surface.

The type of vegetation used is called "deciduous", which is a type of vegetation (plant, tree or shrub) which looses its leaves in autumn and winter. The surface reflectance spectrum used to define the surface type in libRadtran, is shown in Figure 4.11(c) in light blue. Again, the RTM is applied to retrieve the TOA reflectance spectra for different amounts of aerosols. From the figure it can be seen that the reflectance at the TOA increases with increasing amount of AOD in the lower wavelength range (0.4 – 0.75μm), but decreases for larger wavelengths (0.75 – 1.3μm). This can be understood by looking at the surface reflectance spectrum (light blue). In the lower wavelength region, the reflectance of these plants is really low so that aerosols increase the reflection of incoming solar radiation. In the higher wavelength region, however, the absorbing properties of the aerosols are dominant, reducing the amount of reflected radiation. This dual nature is also visible in Figure 4.11(d). As the radiances here are integrations over the full spectrum, the bending shape of the curve indicates a switch where for small AODs, there is a bigger effect of the decreasing TOA reflectance spectrum in the larger wavelengths of the VIS channel than of the increasing spectrum in the smaller wavelengths, and vice versa in the increasing radiances for the larger AODs. The difference in AOD at which the bending occurs between the blue and red curves, results from the different degraded SR curve that is used. As for this surface type too, the aerosols serve partially as a blocking layer for low AOD values, the method explained is not able to predict the right AOD from observations.

In the case of these two land surface types, it is not possible to estimate the sensitivity of the AOD retrieval to the two differently degraded SR curves. A solution for land albedo values which are too high, can be to use the Land Daily Aerosol (LDA) algorithm by Wagner et al. (2007), which uses observations over the whole day, assuming the aerosol layer stays constant over the day, and this way estimates the surface reflection at the same time as the AOD through optimal estimation.

4.4.3 Land Surface Albedo

Another ECV product of GCOS is the land surface albedo, i.e. the ratio of the outgoing reflected flux to incoming flux at the Earth's surface. This is an important component in the Earth radiation budget (ERB) of the Earth (Hansen et al. 1997), as it determines how much of the incoming radiation is reflected by the land, back into the atmosphere. It varies from 10% for dark vegetation to 90% for snow. Small changes to the land, like the presence of snow on trees or the absence of leaves, have an effect on the amount of radiation that is reflected. Hence, permanent changes in land use result in serious shifts in the amount of outgoing VIS radiation in the affected parts of the world, and thus in the local ERB.

The 750 SBDART simulations were made for different types of surfaces, defined by their spectral albedo $A(\lambda)$. As these surface spectra show how much radiation is reflected in the full VIS wavelength range, and not how much of the solar radiation is reflected, they need to be transformed into solar albedo A, which is derived as

$$A = \frac{\int A(\lambda) S_{\text{surf}}(\lambda) \mathrm{d}\lambda}{\int S_{\text{surf}}(\lambda) \mathrm{d}\lambda}, \tag{4.6}$$

where the spectral albedo $A(\lambda)$ is weighted by the solar incoming flux measured at the surface $S_{\text{surf}}(\lambda)$, which was shown before in red in Figure 1.3. As this incoming surface flux is mostly a direct flux (not indirect scattered flux), the albedo considered here is the so-called "black sky" surface albedo. The SBDART simulations can then be used to calculate the surface albedo bias ΔA resulting from the different degraded SR curves. From the clear-sky simulations (379 of the 750) only the 226 over land are used here. Figure 4.12 shows the simulated radiances

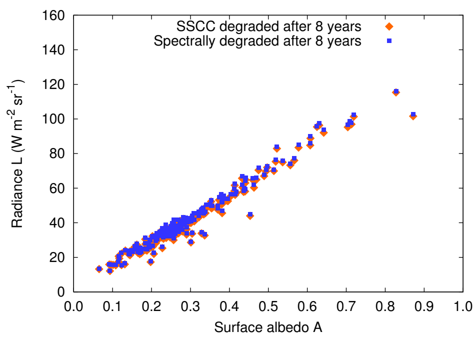

Figure 4.12: Simulated radiances as a function of surface albedo for clear-sky conditions, made using the SBDART code.

as a function of surface albedo for three different surface types together (vegetation, soil, and rock[8]). As can be seen from the figure, the spectral degradation leads to slightly higher simulated radiances than the SSCC degradation. Taking the integrals of the SR curves of Figure 4.8 shows that the surface below the spectrally degraded curve is almost 3% higher (0.430) than below the SSCC degraded one (0.418), explaining this radiance difference.

The simulated radiances are shown for the three surface types separately in Figures 4.13(a), (c), and (e) over vegetation, soil, and rock respectively. It is clear that $L(A)$ can be fitted with a linear function for all three surface types. This means that, when converting the radiance bias ΔL into albedo bias ΔA following Eq. (4.5), the local slope stays constant over the full surface albedo range. The values of the fitted slopes are given in Table 4.5, together with their standard deviations and the standard deviations of the fits. As for each surface type, the slopes are the same (within error margins) for the radiances derived from the two degraded SR curves, the mean value of the slopes is used in Eq. (4.5). Figures 4.13(b), (d), and (f) show the surface albedo bias ΔA as a function of surface albedo. For all three surface types, these values are negative, which is due to the fact that the radiance bias ΔL is negative ($L_{\mathrm{SSCC}} < L_{\mathrm{spec}}$), and become increasingly more negative with increasing albedo A. The latter is a consequence of the fact that the slopes of the fits through the spectrally degraded radiances are consistently larger for these surface types than the ones through the SSCC degraded data (see Table 4.5), leading to negatively increasing radiance biases ΔL with increasing surface albedo.

[8]See Clerbaux et al. (2008) for the list of ASTER spectra used to create these different surface types.

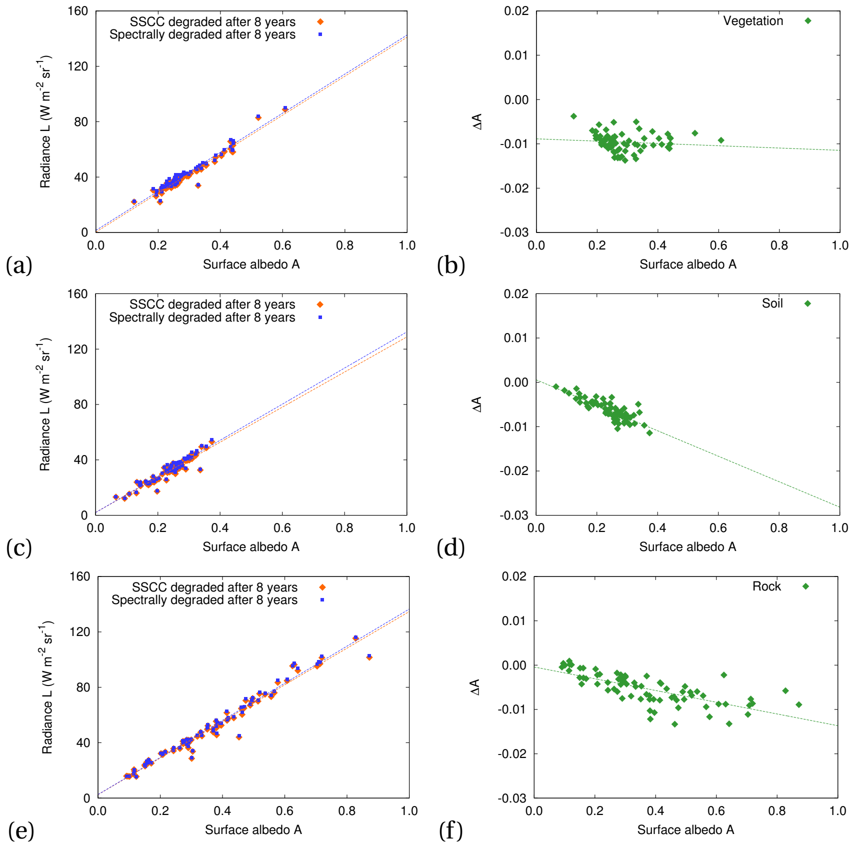

Figure 4.13: Simulations for clear-sky conditions, made using the SBDART code, over (a)–(b) vegetation, (c)–(d) soil, and (e)–(f) rock. The left sided images show the relation between the simulated radiances and the land surface albedo A, while the right side shows the relation between the albedo bias and A.

Table 4.5: The slopes and their standard deviations of the linear fits made through the $L(A)$ data for both degraded SR curves, and the three different scene types. The standard deviation on the fits are also given.

Scene type	SR	slope ($\mathrm{W\,m^{-2}sr^{-1}}$)	standard deviation ($\mathrm{W\,m^{-2}sr^{-1}}$)
Vegetation	SSCC	140.729 ± 3.921	2.834
	Spectral	141.095 ± 4.005	2.895
Soil	SSCC	126.753 ± 5.441	2.890
	Spectral	130.450 ± 5.517	2.931
Rock	SSCC	132.204 ± 2.919	4.579
	Spectral	133.967 ± 2.904	4.556

From all these results it appears that the use of the spectral ageing model instead of the SSCC calibration has a significant effect on the retrieval of surface albedo. This effect is largest over vegetation for small surface albedo values, where a relative method difference of about 5% is measured for a surface albedo of 0.2. For the other surface types the effect is much smaller ($< 2\%$).

4.4.4 CLOUD OPTICAL DEPTH

The COD is, like the AOD, the degree to which solar incoming light is attenuated in the Earth's atmosphere: clouds with a high COD reflect more radiation, while clouds with a low COD still let radiation go through. This reflecting property depends on the liquid/ice water content of the clouds and the size distribution of the cloud droplets/crystals, which is connected to the cloud albedo, and so also to the energy balance of the Earth. The amount of direct radiation that reaches the ground, decreases exponentially with COD ($e^{-\mathrm{COD}}$). There are several ways the COD can be retrieved from satellite observations in the VIS channels. One method is to derive the COD from the reflected radiances L, comparing with simulations. An example of this is the cloud physical properties (CPP) method, used in Climate Monitoring Satellite Application Facility (CM SAF) by, for example, Roebeling et al. (2006), which makes use of the 0.6µm channel of the Spinning Enhanced Visible and Infrared Imager (SEVIRI) to derive the COD in an iterative loop with the retrieval of cloud particle size through the 1.6µm channel, assuming fixed surface albedo maps. A second way to derive the COD from satellite data is through the cloud cover index (or cloud fraction) n, as was done in Ipe et al. (2004). RTMs are used to relate the cloud cover index to the amount of visible radiation observed. Both methods are explored here, (i) using SBDART simulations to show the effect of the two different degraded SR functions on the retrieval of COD through radiances L, and (ii) using libRadtran to do the same,

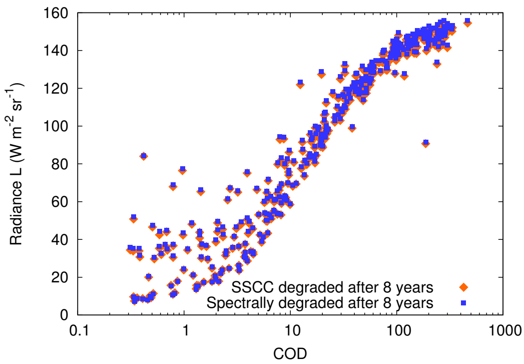

Figure 4.14: Simulated radiances as a function of COD for cloudy conditions, obtained by using the SBDART code.

but making use of the cloud cover index n to derive the CODs.

COD versus L

Figure 4.14 shows the 371 cloudy SBDART radiance simulations used, for different scene types together (ocean, vegetation, soil and rock). From this figure it can be seen that the spectrally degraded radiances are consistently higher than the SSCC degraded ones. As the cloud spectrum covers the whole VIS channel, the fact that the integral of the spectrally degraded SR curve is larger than the integral of the SSCC degraded one, explains again this small radiance difference.

The simulated radiances over ocean only are shown in Figure 4.15(a). The spectrally degraded radiance values are overall larger than the SSCC degraded ones. The radiance bias ΔL can be converted into $\Delta(\log(\text{COD}))$ using Eq. (4.5), where the ECV is now the logarithm of the COD, and the slope is the local slope to the simulated data $\partial L/\partial(\log(\text{COD}))$. In contrast to the previous cases, the $L(\log(\text{COD}))$ relation cannot be approximated by a linear function, and so the slope in Eq. (4.5) is not a constant. It is possible to fit a modified sigmoid function to Figure 4.15(a),

$$L = \frac{a}{1 + b.10^{-\log(\text{COD})/c}} + d, \tag{4.7}$$

where the values for a, b, c, and d are given in Table 4.6. For each simulation, the slope from Eq. (4.5) is taken as the first derivative of the fit (Eq. (4.7)) in that

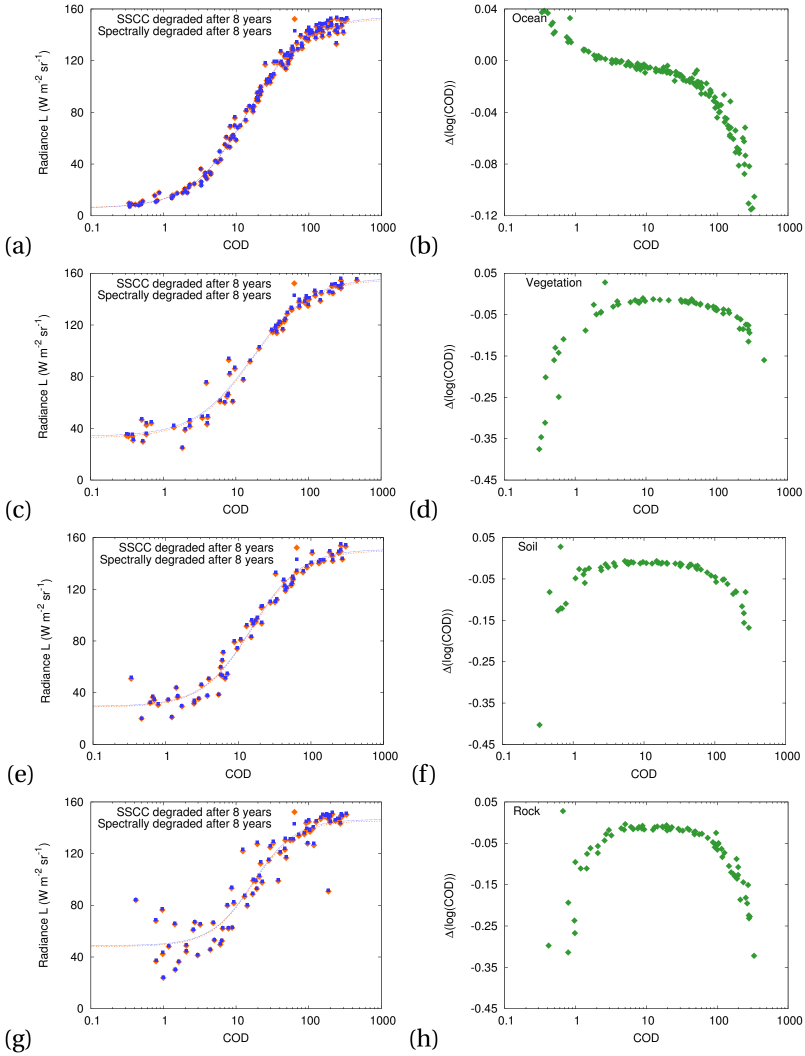

Figure 4.15: Simulations for cloudy conditions, made using SBDART code, over (a)–(b) ocean, (c)–(d) vegetation, (e)–(f) soil, and (g)–(h) rock. The left sided images show the relation between the simulated radiances and the COD, while the right side shows the relation between the COD bias and COD.

Table 4.6: The fitted sigmoid coefficients a, b, c, and d for the $L(\log(\mathrm{COD}))$ data for degraded SR curves and the four different scene types, together with the standard deviation σ of the fits.

Scene type	SR	a	b	c	d	σ
Ocean	SSCC	146.866	19.600	0.895	6.076	4.066
	Spectral	148.345	19.568	0.894	5.795	4.176
Vegetation	SSCC	122.812	21.911	0.918	32.563	6.326
	Spectral	122.690	22.205	0.914	33.831	6.406
Soil	SSCC	121.153	32.142	0.788	28.824	6.779
	Spectral	121.572	32.491	0.785	29.510	6.911
Rock	SSCC	97.287	67.198	0.676	48.142	13.330
	Spectral	97.612	68.793	0.672	48.881	13.459

particular point (COD_0, L_0), as

$$\left.\frac{\partial L}{\partial(\log(\mathrm{COD}))}\right|_{\mathrm{COD}=\mathrm{COD}_0} = \frac{a\,.\,b\,.\ln(10)\,.\,10^{-\log(\mathrm{COD}_0)/c}}{c\left(1+b\,.\,10^{-\log(\mathrm{COD}_0)/c}\right)^2}. \tag{4.8}$$

Figure 4.15(b) shows the bias $\Delta(\log(\mathrm{COD}))$ as a function of COD, which is overall negative as the SSCC degraded radiances are on average smaller than the spectrally degraded ones. The main shape of this figure comes from the fact that the slope in the denominator of Eq. (4.5) varies with COD. For intermediate COD values, the slope is really large, leading to a bias close to zero. For the lower and higher CODs, the smaller value for the slope leads to a bias different from zero, which becomes negative when more clouds are present due to the fact that the integral of the spectrally degraded SR is larger than of the SSCC degraded one, and becomes positive for the smaller COD values as the underlying ocean peaks in the blue part of the VIS spectrum, in the wavelength region where the spectrally degraded SR curve is lower than the SSCC degraded one.

Figures 4.15(c), (e), and (g) show the radiance simulations for vegetation, soil and rock, respectively. For all three, the spectrally degraded radiances are consistently higher than the SSCC degraded ones. Sigmoid fits are made through these curves, and the a, b, c, and d values are also given in Table 4.6. Based on these fits, the COD bias $\Delta(\log(\mathrm{COD}))$ is calculated, and shown in Figures 4.15(d), (f), and (h). The $\Delta(\log(\mathrm{COD}))$ plot has a bending shape, which can be explained as follows. For low values of COD, all of these surface types have a reflectance spectrum with slightly more energy in the red part of the VIS spectrum where the spectrally degraded SR curve is higher than the SSCC degraded one. In the central part (COD between 10 and 100), the values become close to 0 due to the high slope in the denominator of Eq. (4.5). For the highest COD values, the fully opaque clouds determine the radiance values in the same way as over ocean, resulting in a negative bias due to the difference in integral of the degraded SR curves.

Concluding from this, for vegetation, soil, and rock, the relative method difference introduced by the spectral ageing model in the retrieval of COD is about 100% for low COD values, and about 10% over ocean. These values, especially the ones over land, need to be compared however with a quite high standard deviation of the fit, especially for these lower COD values.

***COD versus** n*

The cloud cover index n was defined by Cano et al. (1986) as

$$n = \frac{L - L_{\mathrm{cs}}}{L_{\mathrm{ov}} - L_{\mathrm{cs}}}, \tag{4.9}$$

where L is the measured radiance, L_{cs} is its clear-sky counterpart, and L_{ov} is the radiance that would be measured at an optically opaque overcast scene. This shows that, for a perfectly clear sky, $n = 0$ and for a totally overcast sky, $n = 1$. The SBDART simulations cannot be used here for the same reason as for the AOD retrieval over land: there are simulations available for varying amounts of clouds, but not for the exact same surface conditions. Instead, cloudy simulations are generated with libRadtran over 3 different surface types (ocean, vegetation and desert), and for a fully opaque sky, a clear sky and several intermediate COD values. From the derived simulated radiances, n is calculated and analysed as a function of COD.

Figure 4.16(a) shows the cloud cover index n above ocean for different COD values. From this figure, it is clear that the $n(\log(\mathrm{COD}))$ relation has the same sigmoidal shape as the $L(\log(\mathrm{COD}))$ simulations from Figure 4.15(a). The two degraded SR curves seem to lead to almost equal cloud index values. This is partly due to the subtraction of the radiances in both nominator and denominator of Eq. (4.9), so that the effect of the surface is mitigated. Apart from that, the ratio of radiance to overcast-radiance takes care of the majority of the difference between the two SRs, especially for cloudy observations. The bias of the cloud cover index Δn can be converted into the COD bias $\Delta\log(\mathrm{COD})$ using Eq. (4.5). For this, Figure 4.16(a) is first fitted with a modified sigmoid function

$$n = \frac{a}{1 + b\,.\,10^{-\log(\mathrm{COD})/c}}, \tag{4.10}$$

where the values for a, b, and c are given in the first two lines of Table 4.7, and then the local slope $\partial n/\partial(\log(\mathrm{COD}))$ is calculated through Eq. (4.8), where now the derivative of n is taken with respect to log(COD). Figure 4.16(b) shows the

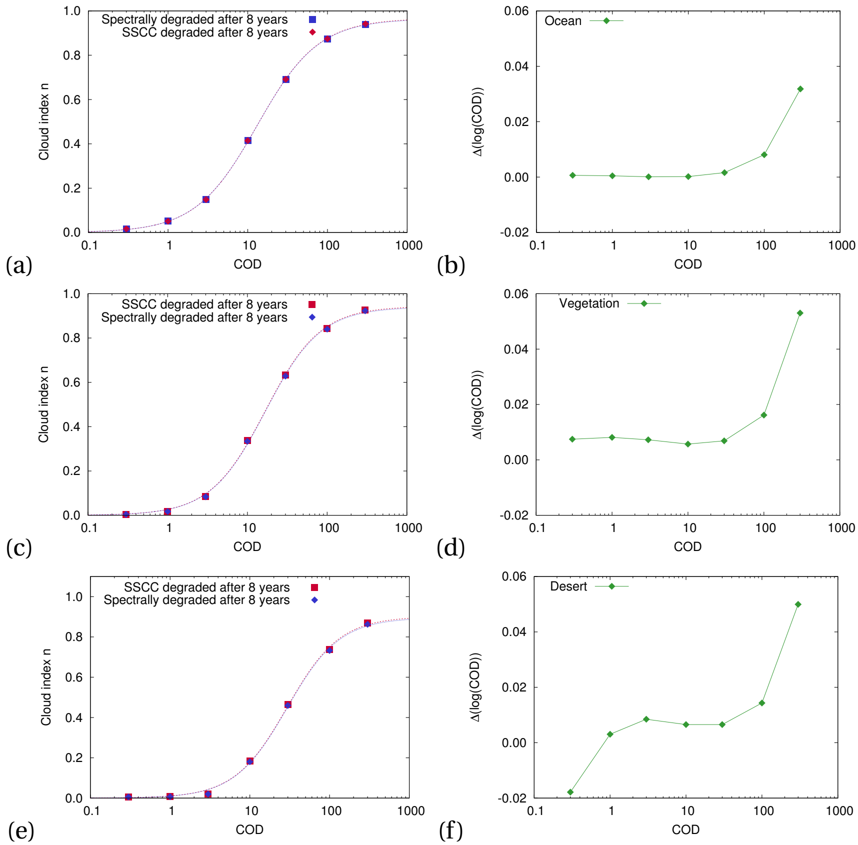

Figure 4.16: Simulations for cloudy conditions, made using libRadtran, over (a)–(b) ocean, (c)–(d) deciduous vegetation, and (e)–(f) sandstone desert. The left sided images show the relation between the simulated cloud indices n and the COD, while the right side shows the relation between the COD bias and COD.

Table 4.7: The fitted sigmoid coefficients a, b, and c for the n(log(COD)) data for both degraded SR curve and three different scene types, together with the standard deviation σ of the fits.

Scene type	SR	a	b	c	σ
Ocean	SSCC	0.9663	18.1426	0.8883	0.0046
	Spectral	0.9639	18.1144	0.8874	0.0046
Vegetation	SSCC	0.9432	34.1098	0.7983	0.0120
	Spectral	0.9394	34.6823	0.7967	0.0121
Desert	SSCC	0.9014	83.3949	0.7635	0.0145
	Spectral	0.8952	84.9523	0.7613	0.0146

relation of Δ(log(COD)) to COD. Comparing this with Figure 4.15(b) shows that here too, the shape of the figure depends on the fact that the slope is not constant over the COD range, but the figure looks like it has been flipped around the x-axis. This is due to the fact that now the effect of a larger integral of the spectrally degraded SR curve than the SSCC degraded one, has arrived in the denominator (in L_{ov}), leading to a smaller n for the spectrally degraded simulations than for the SSCC ones. The left part of the figure is different, staying almost constant around 0 as for low values of COD, the nominator of n becomes almost equal to 0.

The same steps are made for vegetation (see Figure 4.16(c)) and for desert (see Figure 4.16(e)), which show the same sigmoidal shape as over ocean. Here too, the log(COD) bias can be calculated from Δn and the local slope of the sigmoid fit through the n(log(COD)) simulations. Figures 4.16(d) and (f) show the relation between Δ(log(COD)) and COD. For vegetation, this curve is similar to the one for ocean, but with a slightly higher bias for clear-sky simulations. This is due to a combination of the fact that vegetation has a different surface reflectance than ocean, and the low value of the slope in the denominator of Eq. (4.5). For desert, the bias becomes negative for COD values smaller than 1, pointing to the fact that the spectrally degraded cloud cover index n becomes larger than the SSCC degraded one. The reason for this is the fact that desert reflects on average more energy in the longer wavelengths of the VIS spectrum than vegetation (and certainly ocean). This, combined with the low slope, leads to a strong decrease in Δ(log(COD)) for low COD values.

Similarly as for the COD retrieval from the radiance values, here too the relative difference introduced by the spectral ageing model in the retrieval of COD is highest for low COD values over vegetation. The difference, however, is much smaller (about 1.5%) due to the fact that the effect of the surface reflectance is reduced through the definition of cloud cover index. Overall, it can be concluded that, for the retrieval of COD, the use of cloud cover index decreases the sensitivity of the actual shape with respect to the shape of the SR curve.

4.4.5 Incoming Surface Flux

The incoming surface flux (or irradiance) is another important factor in the energy regulation of the Earth. It would most easily be measured from ground stations if their numbers would be sufficient. As the global network has a serious lack of ground measurements over the ocean and in some other parts of the world, satellite measurements are more useful. When measuring the global incoming solar flux at the surface from space, one needs to know the amount of clouds in the atmosphere to derive how much radiation reaches the surface as direct solar irradiance, and how much of the attenuated radiation is scattered in the atmosphere and reaches the surface as diffuse solar irradiance. The method discussed here is a statistical method called Heliosat (Cano et al. 1986), which relies on the same cloud cover index n as in Section 4.4.4. The Heliosat method uses linear regressions between the satellite cloud cover index n and ground measured values for incoming solar irradiance. Based on these regressions, the global incoming surface flux can be derived from satellite observations.

In this study, libRadtran is used to simulate outgoing TOA radiances (to calculate the cloud cover index n), and their equivalent incoming surface fluxes. This is done for different surface types (ocean, vegetation and desert) and different amounts of clouds (COD). In Figure 4.17(a), the relation between the cloud cover index n and the incoming solar flux over ocean is shown. There are four curves in this figure, two for the direct and two for the diffuse incoming irradiance, where the two curves derived from the differently degraded SR curves but the same type of incoming radiation are almost right on top of each other in the figure due to the very small bias in n. The red and blue curves show how the incoming direct solar flux changes with cloud index n. As libRadtran is a plane parallel RTM, for values of n larger than 0.4 the cloud layer is too opaque to let direct solar radiation go through. The yellow and green curves show the amount of diffuse incoming solar flux for a certain degree of clouds. For a cloud index n equal to 0, there is less diffuse light coming in than direct light, as there are no clouds in the sky to scatter the solar radiation, only the molecular gasses and aerosols. With increasing n, the amount of diffuse incoming solar radiation increases while the direct incoming radiation decreases. Around $n = 0.2$, the amount of diffuse incoming solar radiation starts to decrease with increasing cloud cover index n, because the clouds start to reflect more and more radiation directly back into space. As was also the case before when the relation between n and COD was investigated, the cloud index bias Δn is negligibly small due to the definition of n ($\approx$0.2% relative cloud cover index bias). Unlike the COD case, it is not possible to derive the incoming flux bias here. The reason for this is that

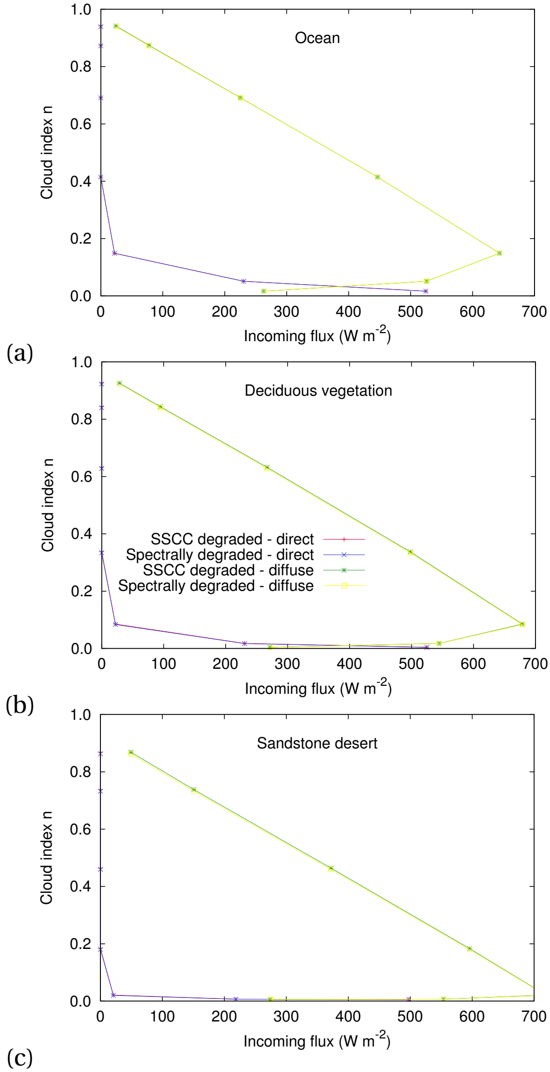

Figure 4.17: Simulations for cloudy conditions, made using libRadtran, for both direct and diffuse incoming radiation, over (a) ocean, (b) deciduous vegetation and (c) sandstone desert.

no reliable fits can be made through the curves of Figure 4.17(a), and so it is not possible to calculate the slope in Eq. (4.5) for each simulation. However, as the cloud cover index bias Δn is so small, the same conclusions can be made here as for the $n(\log(\mathrm{COD}))$ case, i.e. that due to the definition of cloud index, only minor differences are introduced by changing the shape of the SR curve. Figures 4.17(b) and 4.17(c) show the simulations made above vegetation and desert respectively. Similar trends are visible here.

4.4.6 TOA Outgoing Visible Broadband Radiance

Satellite instruments measure the incident radiation through channels with a specific SR. For broadband instruments like the Geostationary Earth Radiation Budget (GERB) or CERES, the channels allow to measure the full outgoing components of the ERB. In the case of GERB, the Royal Meteorological Institute of Belgium (RMIB) has developed a technique to fill in the gaps when no GERB measurements are available for the solar reflected radiance. When this is the case, the data of the narrow 0.6 and 0.8μm VIS channels of the SEVIRI instrument onboard the same satellite are used to create so-called GERB-like data through a narrowband–to–broadband (NB–to–BB) conversion. In future studies, attempts will be made to use the same technique to convert the VIS data of MVIRI into GERB-like data (see Chapter 7), using the overlap period between Meteosat-7 and Meteosat-8. Together with the current shortwave (SW) GERB database, extending the GERB-like dataset in the past would help in delivering a long-term climate data record of broadband solar reflected radiances. In this section, the SBDART simulations are used to show the dependence of the broadband radiance L_{BB} to the two degraded SR curves. The curve used to generate the broadband radiances, is the perfect SR (1 over the full wavelength region) that was used for the unfiltering in Chapter 2.

The NB–to–BB relation is shown in Figure 4.18 for all surface types together and clear-sky conditions. From this figure, one can see that, for a fixed broadband radiance L_{BB}, the spectrally degraded radiances are in general higher than the SSCC degraded ones. This overall effect is explained again by the difference in integrated surface below both degraded SR curves. In Figure 4.19(a) only the clear-sky radiances over ocean are shown. The low radiance values come from the fact that ocean only reflects little solar radiation. The radiance bias ΔL can again be converted into the broadband radiance bias ΔL_{BB} through Eq. (4.5). To do this, the relation in Figure 4.19(a) is approximated by a linear function so that the slope in the denominator is again constant over the full L_{BB} range. Table 4.8 gives the values of the slopes of the linear fits through the simulations. As these values are again the same (within error margins) for both degraded SR curves, the mean value of the slopes is used to calculate ΔL_{BB} through Eq. (4.5). Fig-

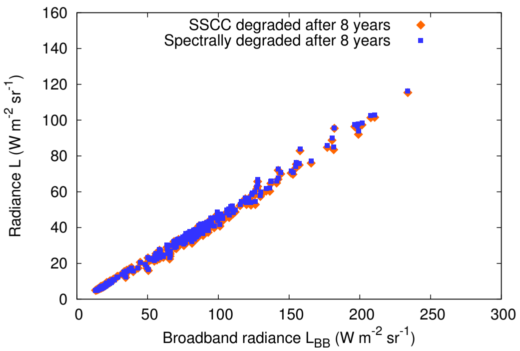

Figure 4.18: Simulated radiances as a function of broadband radiance for clear-sky conditions, made using the SBDART code.

Table 4.8: The slopes and their standard deviations of the linear fits made through the clear-sky $L(L_{\mathrm{BB}})$ data for both degraded SR curves and four different scene types. The standard deviation on the fits are also given.

Scene type	SR	slope	standard deviation ($\mathrm{W\,m^{-2}sr^{-1}}$)
Ocean	SSCC	0.513 ± 0.004	0.276
	Spectral	0.509 ± 0.005	0.298
Vegetation	SSCC	0.522 ± 0.008	1.654
	Spectral	0.525 ± 0.008	1.570
Soil	SSCC	0.486 ± 0.012	1.706
	Spectral	0.500 ± 0.012	1.681
Rock	SSCC	0.501 ± 0.006	2.348
	Spectral	0.508 ± 0.005	2.149

ure 4.19(b) shows this bias as a function of broadband radiance. ΔL_{BB} is positive due to the fact that the SSCC degraded radiances become larger than the spectrally degraded ones, as ocean peaks in the short VIS wavelengths, and the slope in Eq. (4.5) is positive. This difference becomes larger for higher broadband radiances as the effect of the difference in the two degraded SR functions is more pronounced. Figures 4.19(c), (e), and (g) show the clear-sky simulations over vegetation, soil, and rock respectively. In all three cases the spectrally degraded simulations lead to higher radiances than the SSCC corrected ones. The broadband bias ΔL_{BB} is shown as a function of broadband radiance in Figures 4.19(d),

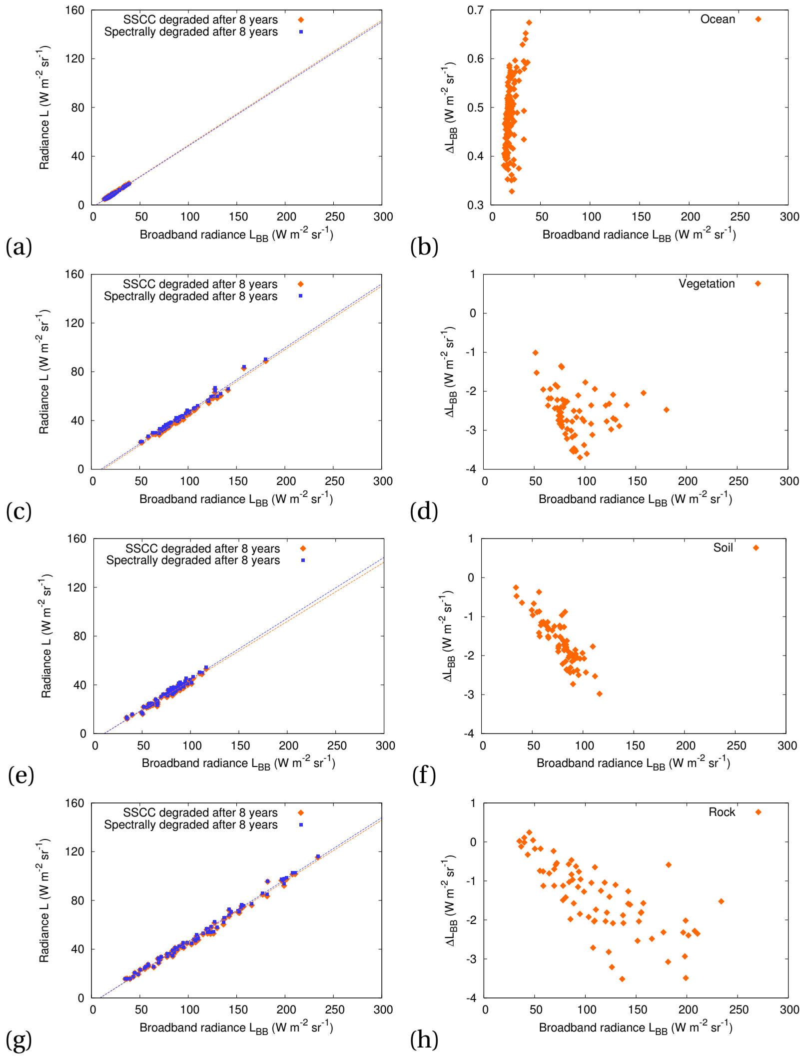

Figure 4.19: Simulations for clear-sky conditions, made using SBDART, over (a)–(b) ocean, (c)–(d) vegetation, (e)–(f) soil, and (g)–(h) rock. The left sided images show the relation between the simulated radiances L and L_{BB}, while the right side shows the relation between the L_{BB} bias and L_{BB}.

(f), and (h). As these scene types reflect more radiation in the longer wavelengths of the visible region than ocean, the bias is negative, and becomes stronger with increasing broadband radiance.

The same work is now done using the cloudy SBDART simulations, as shown in Figure 4.20 for all surface types together (ocean, vegetation, soil and rock). For the same reason as before, the majority of the simulations has a higher spectrally degraded than SSCC degraded radiance. Figure 4.21(a) shows the selection of cloudy simulations above ocean. By comparing with Figure 4.19(a) it is clear that an extended set of COD values were used, where the lower left side shows the clear-sky values, and the upper right side the fully overcast ones. For each simulation, the radiance bias ΔL is converted into broadband bias ΔL_{BB}. To do this, the NB–to–BB relation is fitted with a linear first order function for both degraded radiance values. The slopes of these fits are given in Table 4.9. Here too, the slope used in Eq. (4.5) is taken as the mean value of the slopes of these two fits, as they are again almost the same, within error margins. The broadband bias ΔL_{BB} is shown in Figure 4.21(b) as a function of broadband radiance. The bias decreases with increasing L_{BB} due to the fact that the cloud reflectance spectra are broad and the integrated spectrally degraded SR curve is larger than the integrated SSCC degraded one. The upper left part of the figure shows positive bias values as here the underlying ocean surface is visible. Figures 4.21(c), (e), and (g) show the cloudy simulations above vegetation, soil, and rock surfaces respectively. Again, the simulations for low COD values are situated at the left bottom (comparable to Figure 4.19), while the high COD simulations lead to the highest radiance values. The linear relations between the degraded radiances and the

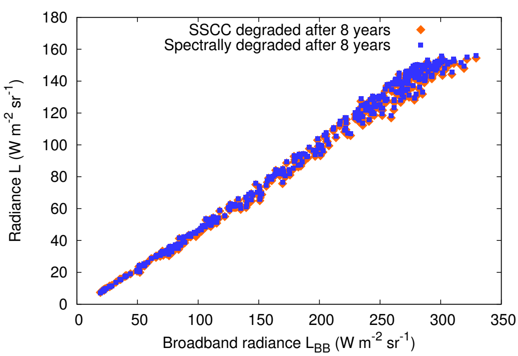

Figure 4.20: Cloudy radiance simulations, made using SBDART as a function of broadband radiance.

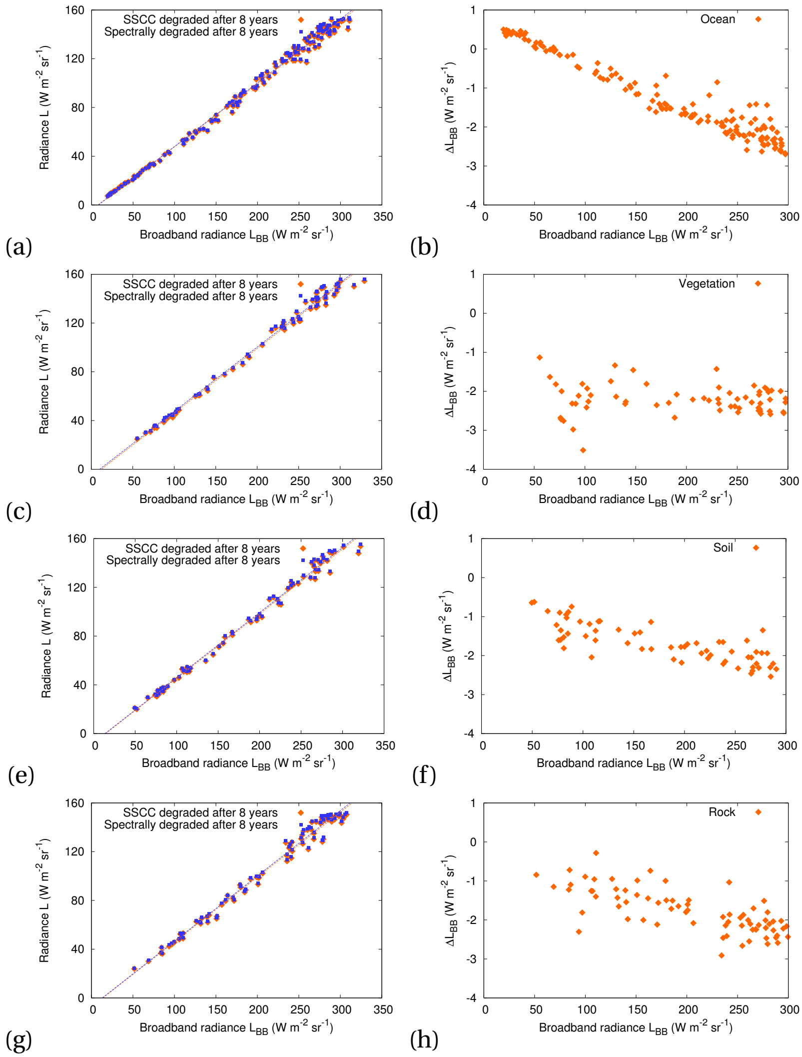

Figure 4.21: Simulations for cloudy conditions, made using SBDART, over (a)–(b) ocean, (c)–(d) vegetation, (e)–(f) soil, and (g)–(h) rock. The left sided images show the relation between the simulated radiances L and L_{BB}, while the right side shows the relation between the L_{BB} bias and L_{BB}.

Table 4.9: The slopes and their standard deviations of the linear fits made through the cloudy $L(L_{BB})$ data for both degraded SR curves and four different scene types. The standard deviation on the fits are also given.

Scene type	SR	slope	standard deviation ($\mathrm{W\,m^{-2}sr^{-1}}$)
Ocean	SSCC	0.517 ± 0.003	3.769
	Spectral	0.523 ± 0.003	3.738
Vegetation	SSCC	0.527 ± 0.006	4.076
	Spectral	0.528 ± 0.006	4.002
Soil	SSCC	0.530 ± 0.006	4.168
	Spectral	0.533 ± 0.006	4.126
Rock	SSCC	0.532 ± 0.008	4.956
	Spectral	0.536 ± 0.008	4.905

broadband radiances are fitted and used to convert the bias ΔL into the broadband bias ΔL_{BB}. The slopes through the fits are shown in Table 4.9, where the mean value is used in the conversion of Eq. (4.5). Figures 4.21(d), (f), and (h) show the same decreasing relation between the broadband bias and broadband radiance for the three land surface types as for the clear-sky.

In conclusion, it seems that the effect of accounting for spectral ageing as opposed to the SSCC method, is to change the broadband radiances over all clear scene types with about 2–5%, over cloudy scenes with about 1–2%. There are 3 sources for the observed differences: first of all the effect of the spectral ageing model over clear ocean, leading to a positive bias, secondly the overall difference, independent of the scene type, due to the difference in integrated surface below the two degraded SR curves, and thirdly, the uncertainty on the model parameters which becomes larger after 8 years.

4.4.7 CONCLUSION

Overall, the main effect of using the spectral ageing model instead of the official EUMETSAT SSCC calibration is largest for the retrieval of background aerosols over ocean, land surface albedo for low albedo values and broadband radiances for low L_{BB} values. These differences range from 2–5%, and are important to take into account when ECVs are retrieved using long data periods of one satellite. This is also clear from Table 4.10 which shows the GCOS requirements for each of the 4 ECVs for the spatial resolution, temporal resolution, accuracy and stability of its time series. The spatial and temporal resolutions are met, except for the spatial resolution of the land surface albedo. When comparing the ΔECV

Table 4.10: For each of the ECVs, the GCOS requirements for the spatial resolution, temporal resolution, accuracy and stability of the long-term data records are given.

ECV	Spatial resolution	Temporal resolution	Accuracy	Stability
Aerosol optical depth	5–10km	4h	max(10%;0.03)	0.01
Land surface albedo	1km	daily to weekly	max(5%;0.0025)	max(1%;0.0001)
Cloud optical depth	50km	3h	10%	2%
TOA ERB shortwave	100km	monthly	$1\,\mathrm{W\,m^{-2}}$	$0.3\,\mathrm{W\,m^{-2}}$

values with the accuracy and stability requirements, it is clear that the use of the spectral ageing model cannot be ignored. There are three important notes to be made here. First of all, the effect over clear ocean is often opposite to the effect over clear land scenes. The reason for this is intrinsic to the spectral ageing model, as after 8 years the SR has become less sensitive than the SSCC degraded one in the short VIS wavelengths than in the longer wavelengths. Apart from that, due to the difference in degradation rate for both methods (exponential instead of linear decrease in time), the integrated surface below both degraded SR curves is different. This has an effect on most of the ECVs discussed here, resulting in significant biases. Finally, it is important to realise how the use of normalised variables (like the cloud cover index, or more generally, the difference between observed radiance and its clear-sky counterpart) reduces the sensitivity with respect to the choice of degraded SR curve.

Chapter Five

Model applied to full MFG

Until now, all results shown and data used, were related to Meteosat-7 alone. The model proves to work fine for this instrument, so it is worth to see what happens to the visible (VIS) data of the other 5 geostationary Meteosat Visible and Infrared Imagers (MVIRIs) when the spectral ageing model is applied. The methodology is very similar to what was used in the previous chapters, with some adjustments which are clearly noted and explained in the first section. The time series of each of the 6 Meteosat satellites are discussed individually, before and after ageing correction, where the Atlantic Ocean data coverage (ADC) and Extended ADC (X-ADC) time series are added for Meteosat-3, and the Indian Ocean data coverage (IODC) time series for Meteosat-5 and -7. At the end of this chapter, the time series are all shown and discussed together as the full Meteosat First Generation (MFG) database at 0° longitude, normalised to Meteosat-7. The results shown in this chapter have recently been submitted to the special edition on "Calibration and Verification of Remote Sensing Instruments and Observations" of the Remote Sensing journal.

5.1 INTRODUCTION

5.1.1 ORIGINAL DEGRADING TIME SERIES

The same 298 clear-sky sites from Chapter 4 are averaged out according to scene type to create for each of the MFG satellites 5 clear-sky reflectance ratio time series (ocean, dark vegetation, bright vegetation, dark desert, and bright desert). The position of the selected sites were shown in Figure 4.1. Stable sites have also been computed using the data of the other satellites, in the same manner as explained in Section 2.5, but they did not prove to be more stable for the full MFG dataset than the sites from Meteosat-7. Together with the convective clouds, this leads to 6 spectrally different time series. The launch date and the exact data

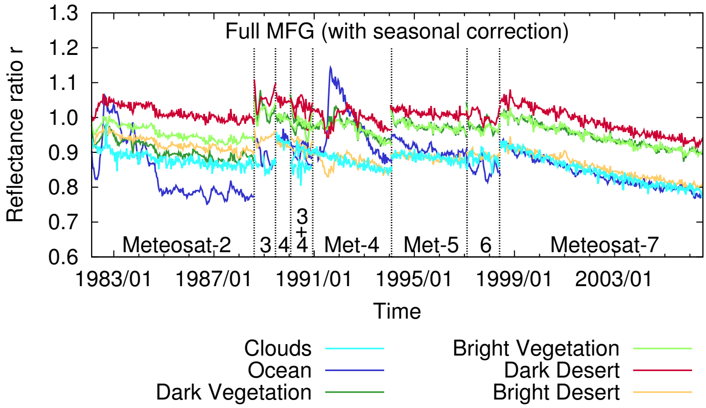

Figure 5.1: The original 6 seasonal corrected time series for all MFG satellites from February 1982 until June 2006. The vertical lines show the switches of operational satellite at the nominal position.

periods at 0° longitude used in this work for each satellite were given before in Table 2.1, together with the gain settings, calibration coefficient, offset, and solar irradiance used in the conversion from digital count (DC) to reflectance ratio r. The original seasonal corrected time series are shown in Figure 5.1 for all 6 satellites together. The label in the figure indicates for which satellite the data are shown. The time series of all 6 satellites are clearly degrading. The spectral character is the clearest in the ocean time series of Meteosat-5 and -7 by comparing them with the other time series. For the other satellites, the spectral degradation is not so clear from the figure. The time periods of observation of Meteosat-3 and -6 at 0° longitude were very short, making it difficult to do the seasonal correction. As said, at least two years of data are necessary, which was not the case for Meteosat-6 (explaining the high noise level in its time series), and was barely the case for Meteosat-3, which was split up in two periods of about one year with a break of several months in between (see Table 2.1). The ocean time series of Meteosat-2 and -4 were influenced by the eruptions of two volcanoes: El Chichón in Mexico (28 March – 4 April 1982) and Mount Pinatubo in the Philippines (June 1991), which is confirmed from the solar radiation transmission observations from the Mauna Loa Observatory in Hawaii as shown by Figure 5.2.

In the following, all the relevant issues which involve several satellites, are discussed and addressed. This is, first of all, the correction done on the ocean time series to eliminate the majority of the effect of the volcanic eruptions. A

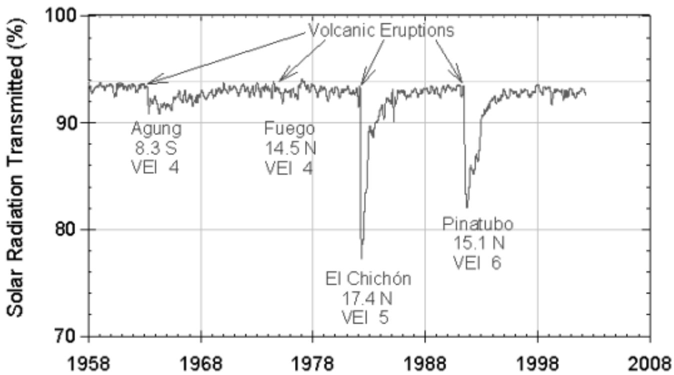

Figure 5.2: Atmospheric solar radiation transmission for the time period 1958–2008, measured by the Mauna Loa Observatory (source: http://www.cmdl.noaa.gov/albums/cmdl_overview/Slide18.sized.png).

second problem is caused by the 6-bit digitisation that was used for Meteosat-2 and -3, and a last problem is the saturation that occurs for these same two instruments.

5.1.2 AEROSOL CORRECTION

Figure 5.3 shows the aerosol optical depth (AOD) over ocean, taken from the Global Aerosol Climatology Project (GACP) (Geogdzhayev et al. (2002) and Mishchenko et al. (1999)) of the National Aeronautics and Space Administration (NASA) Goddard Institute of Space Studies (GISS) for the time period of August 1981 until June 2006, averaged out over the 55 clear-sky ocean targets. This AOD dataset was created using channel-1 and -2 observations of the Advanced Very High Resolution Radiometer (AVHRR), supplemented by data from other satellites, field observations, and chemical-transport modelling. Both Figures 5.2 and 5.3 clearly show the effect of El Chichón and Pinatubo, though in different amounts. The thickest part of the volcanic plume of El Chichón already passed the Mauno Loa Observatory on April 9 1982 on its way westward, while the Pinatubo cloud was only observed in Hawaii one month after the eruptions, when it already had time to spread out, both horizontally and vertically. This explains why the decrease in solar transmission was stronger for El Chichón than for Pinatubo in Figure 5.2, even though Pinatubo had a more powerful impact on the climate. Compared to El Chichón, in 2 months time, about double the amount of Earth surface was covered by the Pinatubo cloud (40%), more than

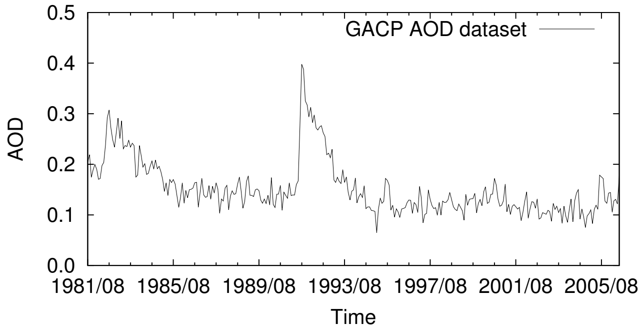

Figure 5.3: GACP AOD measurements for the time period 1981 – 2006, averaged out over the 55 clear-sky ocean targets.

double the amount of aerosols were observed in the first 3 months after the eruption ($20 - 30\times10^9$ kg), and over a period of 10 months, the mean AOD was 1.7 times larger (Kondratyev & Galindo 1997).

As the natural visible signal over ocean is low, the presence of these volcanic aerosols in the region between the upper troposphere and the lower stratosphere, is clearly visible as an increase in reflectance ratio r in Figure 5.1. The effect is also present in the land time series, though differently for Pinatubo than for El Chichón. Vulcanic aerosols can both absorb and reflect solar radiation, where the ratio of absorbing to reflecting properties depend on the type and size of the aerosols. In the case of El Chichón, all five clear-sky time series show an increase between the moment of eruption in April 1982 and the middle of 1984. This indicates that the absorption component of the volcanic particles must have been low enough so that the aerosol layer still increased the solar reflected radiation in that time period. For Pinatubo, however, the desert time series show a decrease in reflectance ratio at the same time as the ocean time series start to increase. In the Pinatubo cloud, the aerosols must have been stronger absorbers than for El Chichón, so that over dark surfaces, the aerosols added to the reflected radiation of the underlying surface, but over brighter surfaces, the absorbing properties reduced the amount of observed radiation. This is confirmed by Kondratyev & Galindo (1997). No effect of the eruptions is visible in the convective cloud time series, as the reflecting tops have such high albedos that neither reflecting nor absorbing effects of the aerosols are visible. From Figure 5.1 it can also be seen that the spread of the aerosols over the Earth went extremely fast (it has been measured to take about a month), but that it took several years before all the ashes had left the stratosphere. This effect is also clear from Figures 5.2 and 5.3.

The time period of the GACP AOD dataset covers the full MFG operational period at 0° longitude (1982 – 2006), and as the measurements were made globally over ocean, they include the effect of the El Chichón and Pinatubo eruptions. These 1° × 1° monthly mean AOD values are used to correct the MFG ocean data in the following way[1]. First of all, to fill the holes where there is, for a certain site and month, no AOD data, the average is taken for that site over the 3 closest non-zero values in time before that month and 3 non-zero values after. Next, the AOD dataset is smoothened out in time to eliminate extreme noise in the original data. This is done by replacing every AOD value with the median of 3 values: the data point itself, the value of the same site the month before and the value of the month after. This monthly mean AOD dataset is then coupled to the monthly mean reflectance ratio time series for each of the clear-sky ocean targets, and for each of the 6 MVIRI instruments. As for AOD values smaller than 1 the reflectance over ocean increases (approximately) linearly with the presence of aerosols (Loeb & Kato 2002), the same relation is valid between AOD and reflectance ratio. Following this, the intercept at AOD = 0 of the linear regression between reflectance ratio and AOD for a certain ocean site should then represent the reflectance ratio that target would have when no aerosols were present. To find this linear relation for each ocean target, the data of all satellites are combined. This way, the range in AOD values is increased, as only for Meteosat-2 and -4 high volcanic AOD values were measured and for the other satellites the amount of aerosols in the atmosphere was low. The linear relation between r and AOD is calculated through the least-squares fitting of

$$r = a_i + b_i\, t + c_i\, t^2 + \mathrm{AOD}\,\frac{\partial r}{\partial(\mathrm{AOD})}. \tag{5.1}$$

In this equation, there are ten parameters that need to be fitted: the satellite dependent coefficients a_i, b_i and c_i of the second degree polynomial used to approximate the degradation for each satellite, and the satellite independent slope of the linear relation between r and AOD, expressed by $\partial r/\partial(\mathrm{AOD})$. The most important parameter here is the slope $\partial r/\partial(\mathrm{AOD})$. This parameter is found by fitting Eq. (5.1) on the observed reflectance ratio r and AOD values for each site, but using the data of all six satellites together. On average, over the different sites, it is equal to 0.61 ± 0.19. Knowing the value of this parameter for each target, allows to subtract the product of $\partial r/\partial(\mathrm{AOD})$ and AOD from each reflectance ratio ocean time series, which is equal to the intercept of the linear regression. This is done for the full ocean time series of each of the 6 satellites.

[1] As no land AOD data were found for this full time period, the land time series are not corrected in this work.

5.1.3 6-BIT DIGITISATION

Meteosat-2 and -3 were part of the pre-operational phase. The discretisation that was used for these satellites, when translating the electrical current into DC, was different for the VIS and water vapour (WV) channels than for the infrared (IR) channel: the output of the VIS and WV channels was converted using 6 bits (values 0 – 63), while for the IR channel, 8 bits were used (values 0 – 255). To make the data of the three channels more comparable, they were converted into 8 bits. For the VIS data, this was done by multiplying each value (in DC) by 4 (Koepke 1982*b*). This leads to the same range of values as for the other two channels, but each time with steps of 4 DC. This is clear from Figure 5.4, which is made using the 55 ocean targets for the Meteosat-2 and -3 time period. The grey crosses show the daily minimum value of the targets (instead of the mean), while the black full curve is the ocean reflectance ratio time series of Figure 5.1. The crosses nicely show the discrete levels, with the majority being a multiple of 4, and some intermediate values which were introduced in the rectification process when the raw (Level 1.0) images were converted into the Level 1.5 images. As there is an offset of about 4, the lowest original non-zero ocean values for Meteosat-2 are around 8, where the volcanic eruption is visible in the time span where the values jump from 8 to 12. The gain change of level 0 to level 1 for Meteosat-2 is indicated by the vertical line, separating Meteosat-2(a) from (b). It can be seen that a number of pixels jumps up from value 8 to 12 after this gain change. For Meteosat-3, the values start at 12 and 16 (Meteosat-3(a)), and fall back to 8 and 12 after the gain

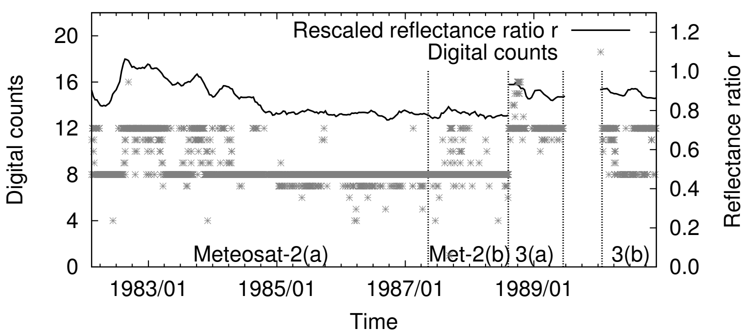

Figure 5.4: 55 ocean targets for Meteosat-2 and -3. The grey crosses are the daily minimum values of the 55 targets (left y-axis). The black full line is the reflectance ratio curve of Figure 5.1 (right y-axis).

went from level 1 to level 0 (Meteosat-3(b)).

This digitisation problem is worst for ocean data as ocean reflects only little light, and so almost all dark ocean values arrive at a digital count value of 8 or 12. For the other scene types, the relative difference is smaller as the signal is higher. Converting the ocean data from digital count to reflectance ratio leads to jumps in the reflectance ratio values. There is a very good correspondence between the 8 to 12 jumps in DC during the volcanic eruption of El Chichón, and the jumps in the reflectance ratio curve for that same time period. This leads to more variation on the reflectance ratio time series and probably also to a bigger effect of the El Chichón eruption in 1982 and the following years. The jumps in DC during the gain changes are not visible in the reflectance ratio time series, as this is corrected for by the different calibration coefficients used.

There is no way to solve this discretisation problem yet at this point. One way to have an idea on the true value of a certain ocean pixel, can be to look at its diurnal cycle, and see how, and if, the values change. There is also some doubt about the offset value, which might be too high due to the conversion of 6 to 8 bits. This issue will return later in Section 5.8, when the results are discussed.

5.1.4 Saturation

A third issue that is discussed here, is the saturation that took place after the gain level change of 0 to 1 for Meteosat-2, and before the gain level change of 1 back to 0 for Meteosat-3 (see Table 2.1 for the exact dates). Figure 5.5 shows the 60 convective cloudy targets at the top of the image and the 37 bright desert targets at the bottom, expressed in digital counts and for both Meteosat-2 and -3. The upper part of the figure shows in black all 6 values that were selected per day as a convective cloudy site, while in grey the daily mean of these 6 values is given on top of it. The bright desert time series in the figure is made up of the daily mean values of all 37 targets, with a temporal frequency of 10 days. The jumps (at the vertical lines) show the point in time when the gain level was changed. Normally these jumps disappear when converting the DC into radiance as different calibration and offset values need to be used before and after the gain change. Due to the saturation, however, the calibration might not correct the convective clouds good enough as the relative jump is smaller for the saturated pixels than for the non-saturated ones.

This relative jump was calculated for both Meteosat-2 and -3, using the bright desert time series in Figure 5.5 as a reference for the saturated convective cloudy time series, because the SEVIRI Solar Channel Calibration (SSCC), that is used in this work for the values of the calibration coefficient and offset at launch, was also based on bright desert scenes which were stable in time (Govaerts et al. 2001). To measure the jump in Figure 5.5 for the convective clouds, linear fits

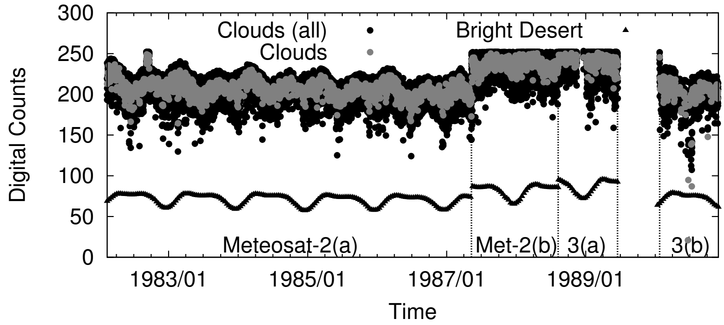

Figure 5.5: The Meteosat-2 and -3 convective cloudy and bright desert time series expressed in DC. At the top in black, all 6 convective cloudy values are shown per day, in grey, the mean of these 6 values is given, and in black at the bottom, the mean values of the 37 bright desert targets are shown.

were made through the daily averaged time series, while for the desert time series, only the tops of the time series were used because the seasonal cycle is very clear and stable for these targets. The relative differences for Meteosat-2 between the time series before and after the gain change are equal to

$$\text{Clouds}: \quad \frac{230-200}{200} = 0.150 \tag{5.2}$$

$$\text{Desert}: \quad \frac{86.7-73.5}{73.5} = 0.180, \tag{5.3}$$

while for Meteosat-3,

$$\text{Clouds}: \quad \frac{205-240}{240} = -0.146 \tag{5.4}$$

$$\text{Desert}: \quad \frac{79-95.6}{79} = -0.174, \tag{5.5}$$

resulting in a difference between both jumps of 0.03 for both satellites, indicating a 3% loss of signal due to saturation. Due to the fact that the convective cloudy targets are averaged out every 10 days, these effects might be less visible in the reflectance ratio time series. So far, nothing is done for this problem either, except knowing that the convective cloudy time series of Meteosat-2 and -3 might not be at the right reflectance ratio values.

5.1.5 Aerosol corrected time series

The original time series, where the ocean is now corrected using the GACP AOD dataset, are shown in Figure 5.6. The reason why the peaks in the ocean time series of Meteosat-2 and -4 have not disappeared, is because it is extremely difficult to find the right value for the reflectance ratio to AOD slope $\partial r/\partial(\text{AOD})$ as there is a lot of variance in the GACP data, especially for the lowest AOD values. Small changes to the $\partial r/\partial(\text{AOD})$ value result in big differences in the aerosol corrected ocean time series. Apart from that, the reason why the peaks for Meteosat-2 are still higher than for Meteosat-4, is most likely because the Meteosat-2 data were digitised using 6 bits while 8 bits were used for Meteosat-4. Overall it can be seen that the ocean time series of all 6 satellites are lower when comparing to Figure 5.1, without large temporal changes. To have an idea on the amount of degradation per year for each satellite, linear fits are made through the time series. The ratio of slope (yr^{-1}) to intercept then gives the percentage of decrease per year. These values are shown in Table 5.5 in Section 5.8 for each satellite, where the explanation of how the standard deviations are computed is given in the Appendix.

In the following sections the time series are corrected per satellite. The results are shown and compared before and after ageing correction, and the model parameters, leading to this correction, are given.

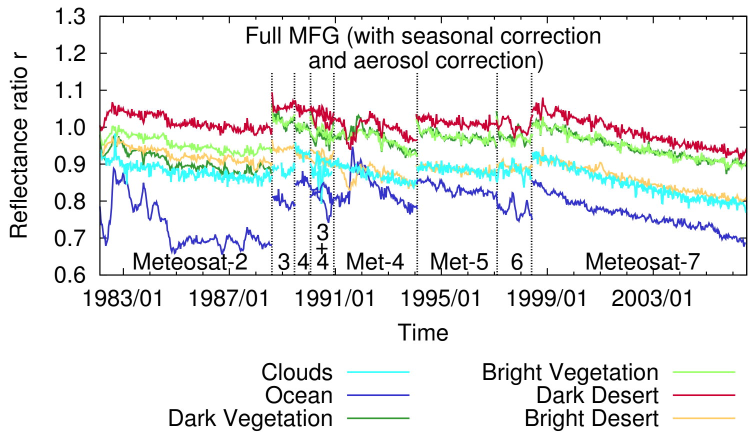

Figure 5.6: The original seasonal corrected time series for all 6 satellites, where the ocean time series is corrected for aerosols using the GACP AOD dataset.

5.2 METEOSAT-2

In June 1981, Meteosat-2 was launched as the second satellite in the Meteosat pre-operational phase. The dataset used at 0° longitude, runs from February 1982 to August 1988. As explained previously, a gain level change was made, resulting in different calibration coefficients before and after[2]. Even though the VIS channel makes use of 2 detectors, for the satellites in the pre-operational phase, one of the two detectors was turned off every second image (the one at **00 Universal Time Convention (UTC)) because of transmission bandwidth limitations (Govaerts & Lattanzio 2007). The 6 original reflectance ratio time series for Meteosat-2 are shown in Figure 5.7(a) before the seasonal correction, (b) after the seasonal correction, and (c) after the ocean time series are corrected for aerosols. The El Chichón eruption can be seen in all three panels during the period of April 1982 to October 1984, as an increase for all clear-sky time series. There seems to be some yearly increased noise in the second half of the year in the clear-sky time series of the (b) and (c) panels of the figure. Comparing with Figure 5.7(a), this falls together with the strong dips of the residual seasonal cycle. The reason for this added variation comes from the fact that the seasonal correction is computed monthly and, in this case, the variation during each month is large and does not correct all 3–4 images per month.

The 6 time series are now corrected for ageing. When minimising the cost function of Eq. (3.5), the parts of the time series which are most affected by the volcanic eruption are not used as these would lead to overcorrections. As the effect of El Chichón is most clearly visible in the time period of April 1982[3] to October 1984, this part is removed for the 5 clear-sky time series. This is a balance between taking away the necessary data during the eruption and still retaining enough for a stable parameter fitting. The same omitted periods are avoided when doing the seasonal correction. Due to the high variation in the ocean time series, it is not possible to find a positive γ parameter using this minimisation technique. Figure 5.7(d) shows the 6 ageing corrected time series, where the model parameters used are

$$\begin{aligned} \text{slope} &= -0.017 \pm 0.008\,\text{yr}^{-1} \\ \alpha &= 0.00044 \pm 0.00034\,\text{day}^{-1} \\ \beta &= 0.90 \pm 0.26 \\ \gamma &= 0.00 \pm 0.00\,\mu\text{m}^{-1}\,\text{day}^{-1}. \end{aligned}$$

[2] Another gain change was performed earlier on 20 October 1981 going from level 1 to level 0.

[3] This is a few months after the eruption took place, because this seems to be the moment around which the aerosols were spread far enough around the globe to start affecting all ocean data in the clear-sky images.

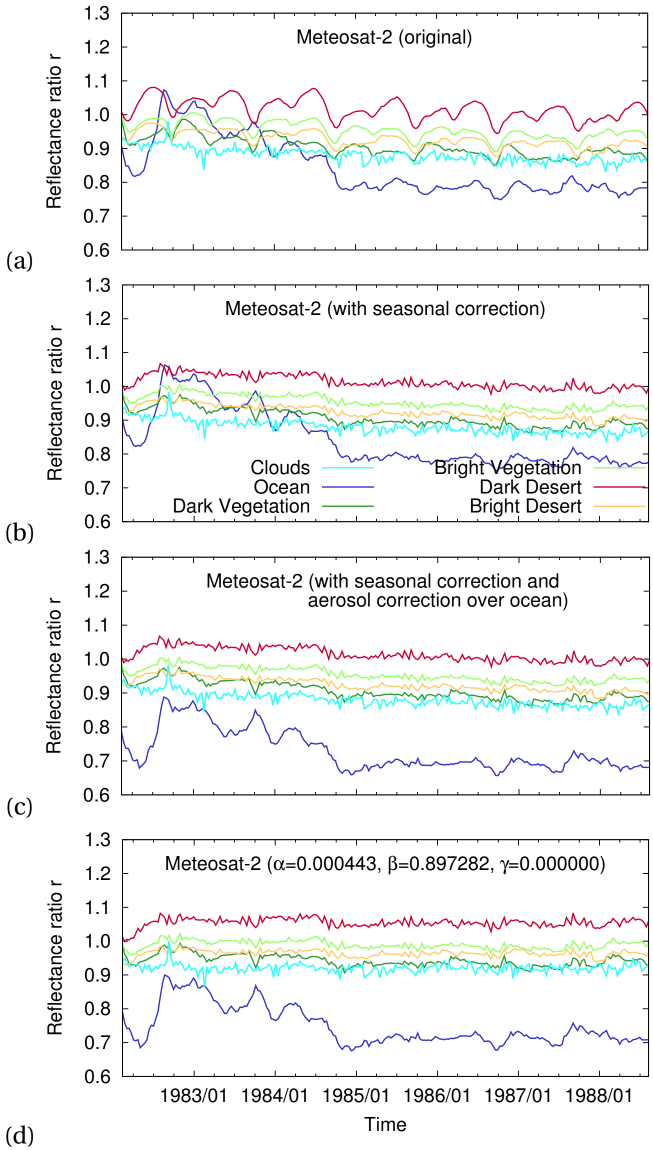

Figure 5.7: Meteosat-2 time series (a) before seasonal correction, (b) after seasonal correction, (c) after aerosol correction, and (d) after ageing correction.

The percentages of change per year of the linear fits through the ageing corrected time series are added in Table 5.5 in Section 5.8, together with the standard deviations. For the calculation of these slopes, the same time periods where the effect of El Chichón is the largest, are not used.

5.3 METEOSAT-3

The third Meteosat satellite - and at the same time the last of the pre-operational programme - was launched in June 1988. The satellite replaced Meteosat-2 as the main operational satellite in August of the same year and stayed at 0° longitude for about 10 months. After a period of 7 months, it started to collect data again for a second period of a bit more than one year. For this second period, the gain level was changed back from 1 to 0. Figure 5.8 shows the original time series before seasonal correction in panel (a), after seasonal correction in panel (b), and after aerosol correction for the ocean time series in panel (c). The variation seems to be slightly higher in the time series of the second period than in the ones of the first period. This could be due to the deseasonalisation, which is done using both parts together but is still in total barely long enough to calculate the mean annual cycle. Apart from that, there is also the 6-bit digitisation problem which introduces jumps in the ocean reflectance ratio time series (as can also be seen from Figure 5.4).

The ageing model is applied to the time series and the result is shown in Figure 5.8(d). The parameters used are

$$\begin{aligned} \text{slope} &= -0.009 \pm 0.027\,\text{yr}^{-1} \\ \alpha &= 0.00010 \pm 0.00029\,\text{day}^{-1} \\ \beta &= 0.75 \text{ (fixed)} \\ \gamma &= 0.0000 \pm 0.0004\,\mu\text{m}^{-1}\text{day}^{-1}. \end{aligned}$$

It was not possible to find significant γ and β values, so the value for γ becomes equal to the smallest possible value, i.e. zero, and, since the time period is really short, the β parameter is fixed at 0.75, about the value found in Section 4.2 for Meteosat-7. The residual slopes of the 6 ageing corrected time series, expressed in percentage per year, are added to Table 5.5 of Section 5.8.

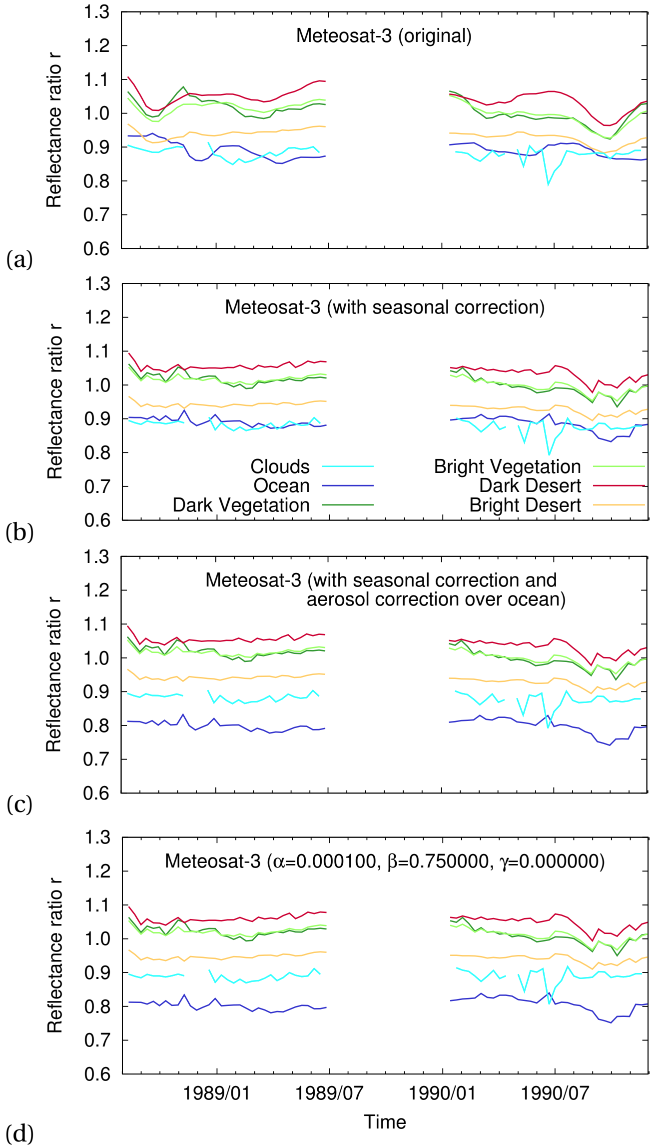

Figure 5.8: Meteosat-3 time series (a) before seasonal correction, (b) after seasonal correction, (c) after aerosol correction, and (d) after ageing correction.

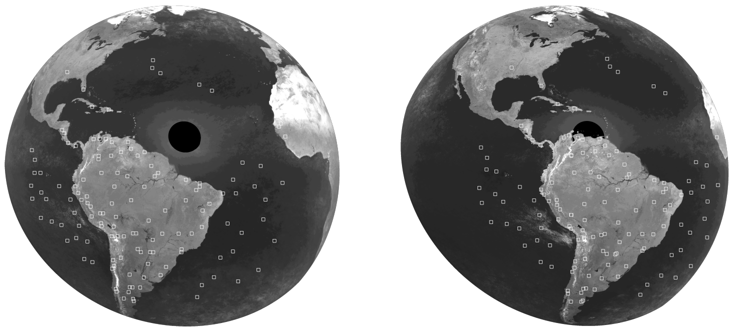

(a) (b)

Figure 5.9: The selected clear-sky stable sites for the 134 overlapping sites for (a) the ADC at 50° W and (b) the X-ADC at 75° W.

5.3.1 ATLANTIC OCEAN DATA COVERAGE (ADC / XADC)

In August 1991, Meteosat-3 was moved over the Atlantic Ocean for the ADC at 50° W, in loan to the National Oceanic and Atmospheric Administration (NOAA) to take over the operations from the sixth Geostationary Operational Environmental Satellites (GOES) which had failed in 1989. After one year and a half, Meteosat-3 was relocated to the GOES-East nominal position of 75° W, to run the X-ADC from February 1993 until November 1995. The field–of–views (FOVs) of the ADC and X-ADC are shown in Figures 5.9(a) and (b) respectively. The same procedures are followed for the ADC and X-ADC datasets as was done for the data at the nominal position, in an attempt to improve the model parameters by increasing the length of the Meteosat-3 time series. As there is not much overlap between the FOV above the Atlantic Ocean and the FOV at the nominal position of 0° longitude, new sites are selected. This is done in the same way as explained in Chapter 2, but now looking for overlapping clear-sky sites which are present in both Atlantic FOVs. The selected 134 sites are indicated by the white boxes in Figures 5.9(a) and (b). Figure 5.10 shows the resulting time series after aerosol correction for the nominal position, ADC and X-ADC data. The time period for the ADC is too short to perform the seasonal correction. Instead, the seasonal correction factors of the X-ADC period are used, which are unfortunately not able to correct the ADC data. On top of that, the time period of the ADC was also right in the aftermath of the Pinatubo eruption of June 1991. It is not possible to remove the effects of Pinatubo from the data due to a combination of the fact that the seasonal correction is not good enough, the Meteosat-3 data are processed using 6 bits, and the fit of reflectance ratio r with respect to AOD is too unsta-

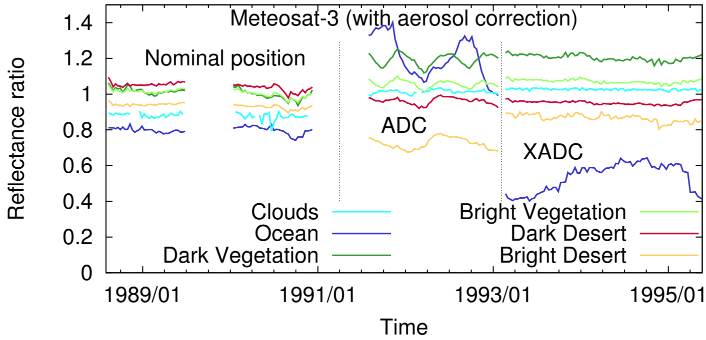

Figure 5.10: Original Meteosat-3 time series for the data coverage at 0° longitude (August 1988 – December 1990), the ADC at 50° W (August 1991 – January 1993), and the X-ADC at 75° W (February 1993 – May 1995), using the overlapping sites.

ble[4]. The latter is also visible in the X-ADC period, where the AOD correction introduces extra variability in the ocean time series. The fact that the convective cloudy time series do not connect over the three time periods of Meteosat-3 data, hints to a possible other gain change when Meteosat-3 was moved over the Atlantic Ocean. An attempt was made to correct these time series for spectral ageing, but due to the fact that both the 6 ADC time series and the X-ADC ocean time series are not useful, this does not lead to an improvement of the Meteosat-3 model parameters.

5.4 METEOSAT-4

The Meteosat Operational Programme (MOP) started with the launch of Meteosat-4 in March 1989. The operational period used here runs from June 1989 until February 1994. For Meteosat-4 and the rest of the MFG satellites, no more gain changes were performed while the satellites were operational. The original reflectance ratio time series are shown in Figure 5.11(a) before and (b) after seasonal correction, and in panel (c) after the aerosol correction was performed for the ocean time series. The effect of Pinatubo is visible as an increase in the ocean time series of panel (c) from June 1991 until July 1993, and a decrease

[4] At the nominal position, it was possible to use all 6 satellites to do this fit, and even then the method was very sensitive to small AOD changes. In this case, only 4 years of data are available to fit the r to AOD relation on.

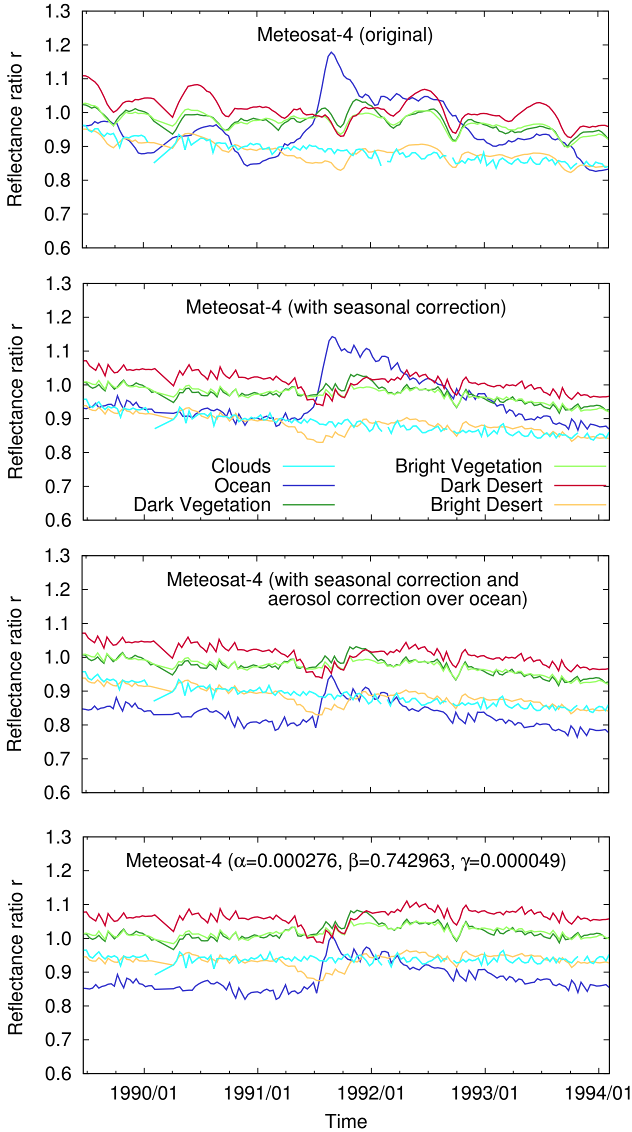

(a) (b) (c) (d)

Figure 5.11: Meteosat-4 time series (a) before seasonal correction, (b) after seasonal correction, (c) after aerosol correction, and (d) after ageing correction.

in the desert time series until December 1991. The increased variance that was visible in the time series of Meteosat-2 due to the deseasonalisation, can be seen here too. When comparing with Figure 5.11(a), it is clear that it coincides with the steep slopes in the seasonal cycles.

In Figure 5.11(d), the time series have been corrected for spectral ageing. Similarly as for El Chichón in the Meteosat-2 data, the period where the effect of Pinatubo is the largest, is not used in the seasonal, nor the ageing correction of the Meteosat-4 time series. The ocean data are not considered between June 1991 and July 1993, while the land time series are not used between June 1991 and December 1991. This leads to the following model parameters:

$$\begin{aligned}
\text{slope} &= -0.026 \pm 0.002\,\text{yr}^{-1} \\
\alpha &= 0.000276 \pm 0.000075\,\text{day}^{-1} \\
\beta &= 0.743 \pm 0.145 \\
\gamma &= 0.000049 \pm 0.000037\,\mu\text{m}^{-1}\text{day}^{-1}.
\end{aligned}$$

Table 5.5 of Section 5.8 shows how the fits through the ageing corrected Meteosat-4 time series evolve in time. These values were calculated avoiding the same time periods for the ocean and land time series where the eruption of Pinatubo most affects the data.

5.5 METEOSAT-5

As the second MOP satellite, the European Organization for the Exploitation of Meteorological Satellites (EUMETSAT) launched Meteosat-5 in March 1991. The satellite became officially operational in May 1991, but until January 1994 Meteosat-4 and -5 alternated at the nominal position as operational satellite. There is not enough Meteosat-5 data available to use in this period to create the clear-sky images, so the dataset used here runs only from January 1994 until February 1997. Following the suggestion of Govaerts (1999), the spectral response (SR) curve of Meteosat-7 is used in the unfiltering process of the Meteosat-5 data, for which the calibration coefficient and offset value are given on the EUMETSAT webpage and are used here in this work (see Table 2.1). In Figure 5.12(a) and (b), the 6 original time series are shown for Meteosat-5, before and after seasonal correction respectively. There seems to be again some yearly increased noise from September to October in the time series of the (b) panel of the figure. Comparing with Figure 5.12(a), this falls together again with the deeper dips of the seasonal effects. Figure 5.12(c) shows the ocean time series which have been corrected for aerosols.

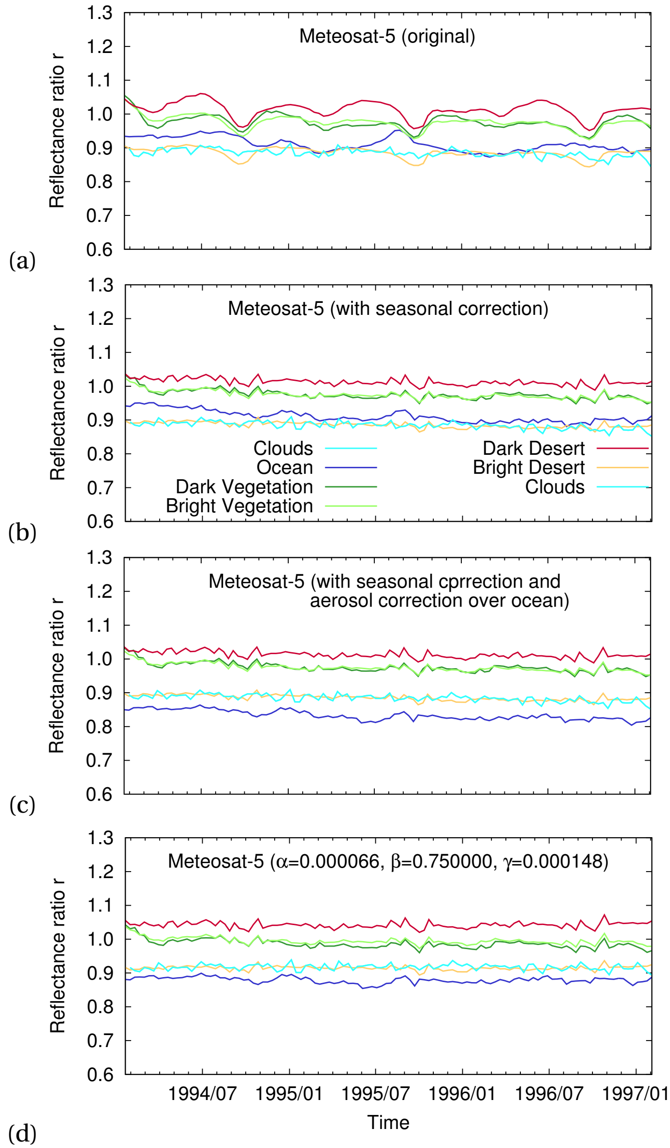

Figure 5.12: Meteosat-5 time series (a) before seasonal correction, (b) after seasonal correction, (c) after aerosol correction, and (d) after ageing correction.

After correcting the time series with the spectral ageing model, the minimisation process leads to the parameters

$$\begin{aligned} \text{slope} &= -0.0060 \pm 0.0073\,\text{yr}^{-1} \\ \alpha &= 0.000066 \pm 0.000081\,\text{day}^{-1} \\ \beta &= 0.75 \text{ (fixed)} \\ \gamma &= 0.00015 \pm 0.00011\,\mu\text{m}^{-1}\text{day}^{-1} \end{aligned}$$

for which the corrected time series are shown in Figure 5.12(d). The β value was kept fixed again, as the Powell method did not lead to a plausible value.

5.5.1 Indian Ocean Data Coverage (IODC)

Meteosat-5, -6 and -7 were all three relocated over the Indian Ocean after their operational period at 0° longitude, to support the Indian Ocean Experiment (INDOEX). Meteosat-5 was moved to 63° E, and was the operational satellite for the IODC from June 1998 until December 2006. The data over the Indian Ocean are treated in the same way as the data at the nominal position, in order to increase the time period and improve the model parameters. Different targets need to be found for the IODC dataset, as the IODC FOV barely overlaps with the FOV at 0° longitude. Figure 5.13 shows the Meteosat FOV over the Indian Ocean at 63° E with the selected set of 338 clear-sky targets. The time series for the six different scene types are shown in Figure 5.14(a) before seasonal correction, (b) after

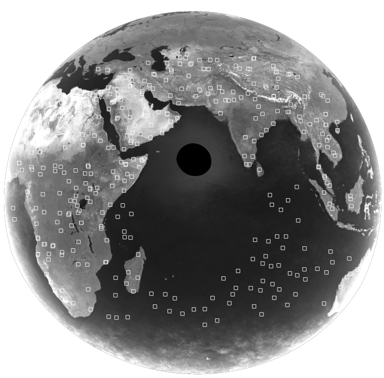

Figure 5.13: The selected clear-sky stable sites on top of the Meteosat FOV above the Indian Ocean for the IODC of Meteosat-5 at 63° E.

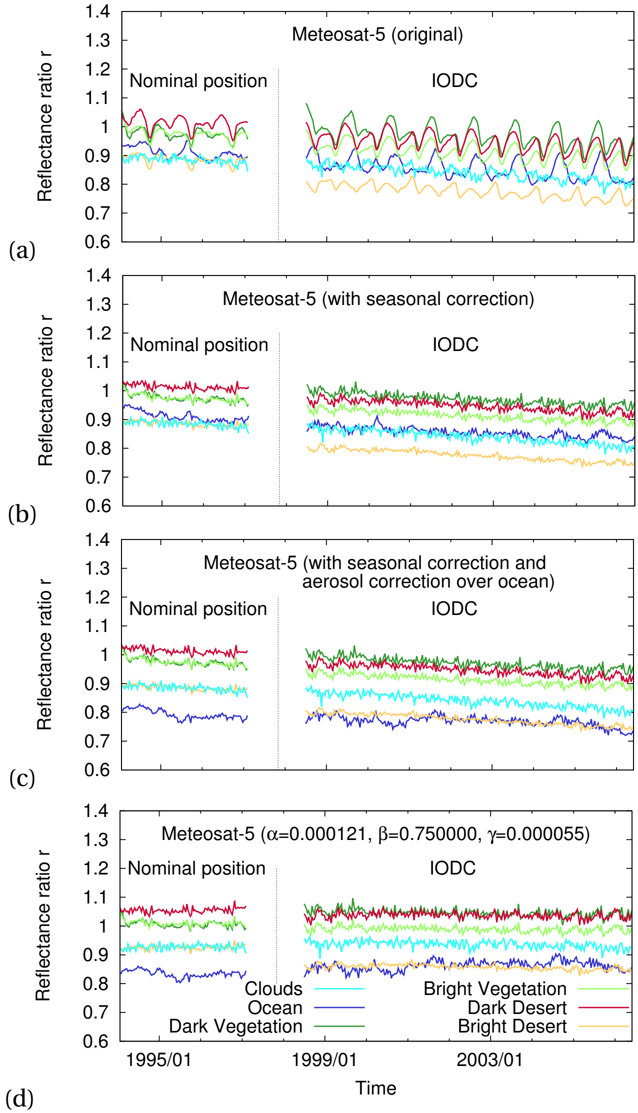

Figure 5.14: Meteosat-5 time series for the data coverage at 0° longitude, and the IODC at 63° E (a) before seasonal correction, (b) after seasonal correction, (c) after aerosol correction and (d) after ageing correction.

Table 5.1: The yearly percentage of decrease of the Meteosat-5 IODC time series, before and after ageing correction. The explanation of how these values are computed, is given in the Appendix.

Surface type	before ageing correction	after ageing correction
convective clouds	-0.9833 ± 0.0267	-0.2384 ± 0.0279
ocean	-0.5651 ± 0.0453	0.2848 ± 0.0451
dark vegetation	-0.6889 ± 0.0257	-0.1921 ± 0.0268
bright vegetation	-0.6563 ± 0.0226	-0.1042 ± 0.0236
dark desert	-0.7204 ± 0.0240	-0.0856 ± 0.0255
bright desert	-0.9257 ± 0.0193	-0.2355 ± 0.0206

seasonal correction, and (c) after the ocean time series have been corrected for aerosols. These figures show both the data at the nominal position and the IODC. The time series for the IODC data period do not connect with the first set of time series because different sites are used. Either way, it is clear that the IODC time series keep degrading in a similar way as the time series at the nominal position. The end of the IODC time series seem to show some extra variation, which might be due to an increased inclination angle of the orbit at the end of the satellite's lifetime when fuel became scarce.

The full set of time series (0° + 63°) are now corrected for ageing, where this time the cost function that is being minimised contains 2×6 time series so that the variance of both data coverages is as low as possible. Figure 5.14(d) shows the ageing corrected time series, using the parameters

$$
\begin{aligned}
\text{slope} &= -0.0110 \pm 0.0007\,\text{yr}^{-1} \\
\alpha &= 0.000121 \pm 0.000009\,\text{day}^{-1} \\
\beta &= 0.75 \text{ (fixed)} \\
\gamma &= 0.000055 \pm 0.000020\,\mu\text{m}^{-1}\text{day}^{-1}.
\end{aligned}
$$

These parameters are really close to the ones found using only the observations at the nominal position. Due to the fact that the dataset used here is longer, and that the standard deviations of the parameters are smaller than the ones derived from the data at the nominal position alone, they are taken as the best set of model parameters to correct the Meteosat-5 data. The percentages per year of the slopes of the linear fits through the ageing corrected time series at 0° longitude are added to Table 5.5, while the IODC slopes are shown in Table 5.1, both before and after ageing correction.

5.6 METEOSAT-6

Meteosat-6 was launched in November 1993 as the third and last satellite in the MOP. It remained the back-up satellite for Meteosat-5 until January 1997, and this due to a high noise level in the WV channel, which was observed soon after launch. Only one year and a half of data are available to work with (January 1997 – June 1998). For Meteosat-6 too, the suggestion of Govaerts (1999) is followed to replace the SR curve at launch by the one of Meteosat-7, and use the adjusted calibration coefficient and offset values given on the EUMETSAT website (see Table 2.1 for the exact values). Figure 5.15(a) shows the original time series before seasonal correction, (b) after seasonal correction, and (c) after aerosol correction. As there are not enough data available to calculate the mean annual cycle, the seasonal correction factors of Meteosat-7 are used, but by comparing figures (a) and (b), it is clear that this does not remove the Meteosat-6 seasonal effects.

The minimisation technique proves not to be able to find any significant parameters for this dataset. Even when β is kept fixed at 0.75, the Powell method returns zero values for the three other parameters. As long as the seasonal correction cannot be performed, it is not possible to find good parameters this way. As mentioned earlier, Meteosat-6 was also operational over the Indian Ocean, but unfortunately this was only as back-up, and not enough data are available to do the clear-sky process and extend the time series. In the discussion at the end of the chapter, it is explained how Meteosat-6 can still be manually corrected making use of the ageing corrected time series of Meteosat-5 and -7.

5.7 METEOSAT-7

The last of the MFG satellites was launched in September 1997 and was part of the Meteosat Transition Programme (MTP) between the first and second generation of Meteosat satellites. Meteosat-7 was operational at 0° longitude from June 1998 until July 2006. The 6 original time series are shown in Figure 5.16(a) before seasonal correction, in panel (b) after seasonal correction and (c) after aerosol correction. The same periodic variability that was seen for Meteosat-2, -4 and -5, is visible in figures (b) and (c) resulting from the way the deseasonalisation is done.

After correcting the time series with the spectral ageing model from Eq. (3.2), they become the ones shown in Figure 5.16(d). The model parameters that come

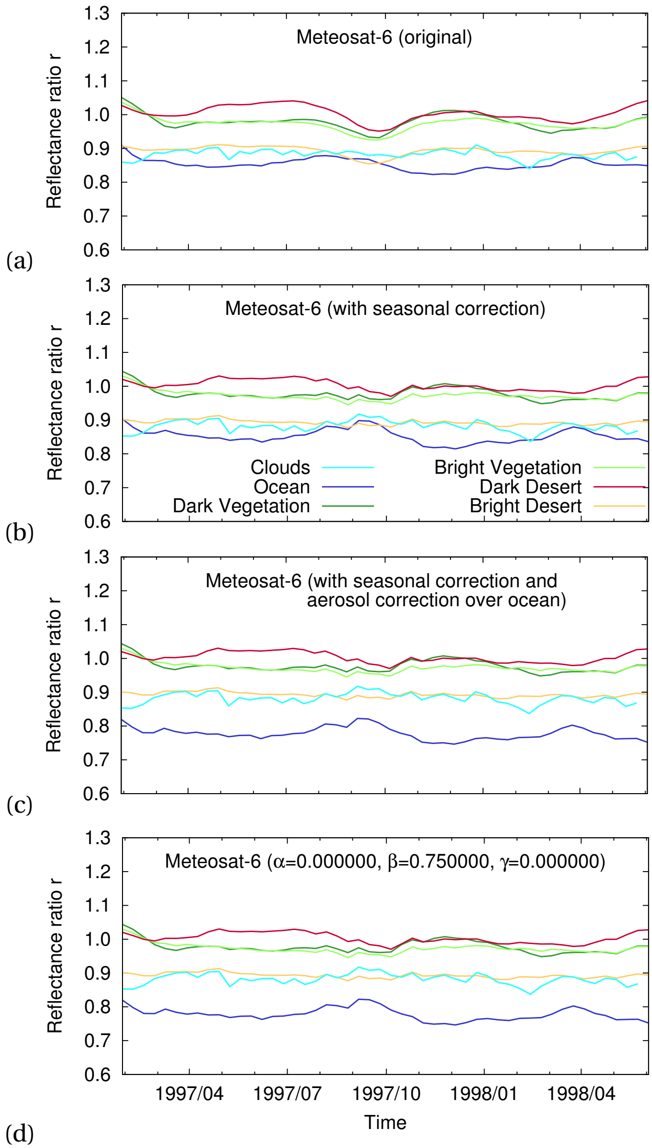

Figure 5.15: Meteosat-6 time series (a) before seasonal correction, (b) after seasonal correction, (c) after aerosol correction, and (d) after ageing correction.

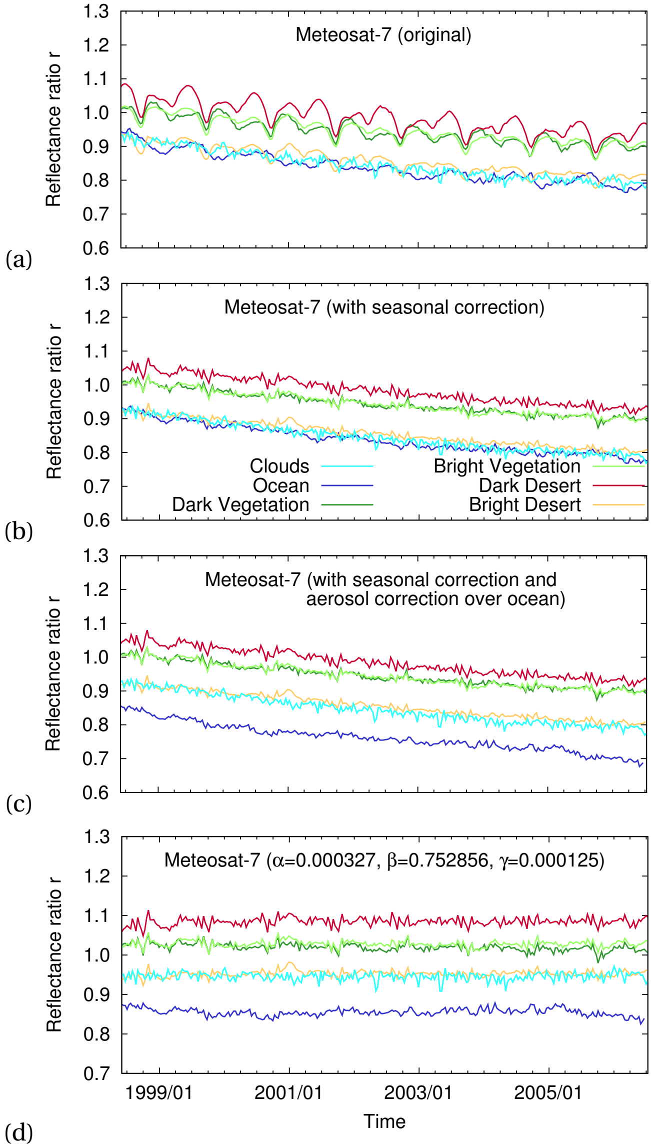

Figure 5.16: Meteosat-7 time series (a) before seasonal correction, (b) after seasonal correction, (c) after aerosol correction, and (d) after ageing correction.

out of minimising the cost function are

$$
\begin{aligned}
\text{slope} &= -0.0295 \pm 0.059\,\text{yr}^{-1} \\
\alpha &= 0.000327 \pm 0.000009\,\text{day}^{-1} \\
\beta &= 0.7529 \pm 0.0053 \\
\gamma &= 0.000125 \pm 0.000014\,\mu\text{m}^{-1}\text{day}^{-1}
\end{aligned}
$$

which differ from the ones given in Chapter 4 due to the AOD correction done here.

5.7.1 Indian Ocean Data Coverage (IODC)

In December 2006, Meteosat-7 took over the operations of Meteosat-5 in the IODC at 57° E, and is expected to continue to do this at least until 2016. By extending the time series at the nominal position with the IODC time series, the model parameters can be improved, having now, like Meteosat-5, about 13 years of data of the same satellite. New sites are selected over the Indian Ocean due to the lack of overlap with the 0° longitude FOV. The 314 clear-sky targets are shown in Figure 5.17. Figure 5.18 shows the original time series for the targets at the nominal position and the IODC targets (a) before, and (b) after the seasonal correction. The full dataset nicely shows the exponential behavior, where the degradation saturates in the IODC part of the time series. No aerosol correction

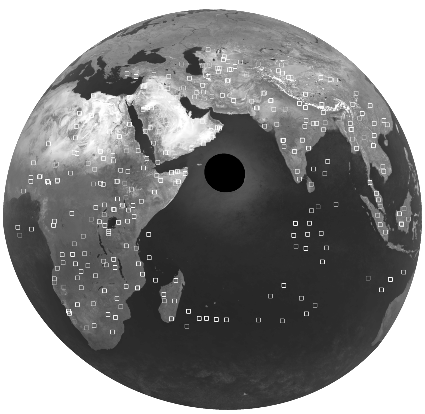

Figure 5.17: The 314 selected clear-sky stable sites on top of the Meteosat FOV above the Indian Ocean for the IODC of Meteosat-7 at 57° E.

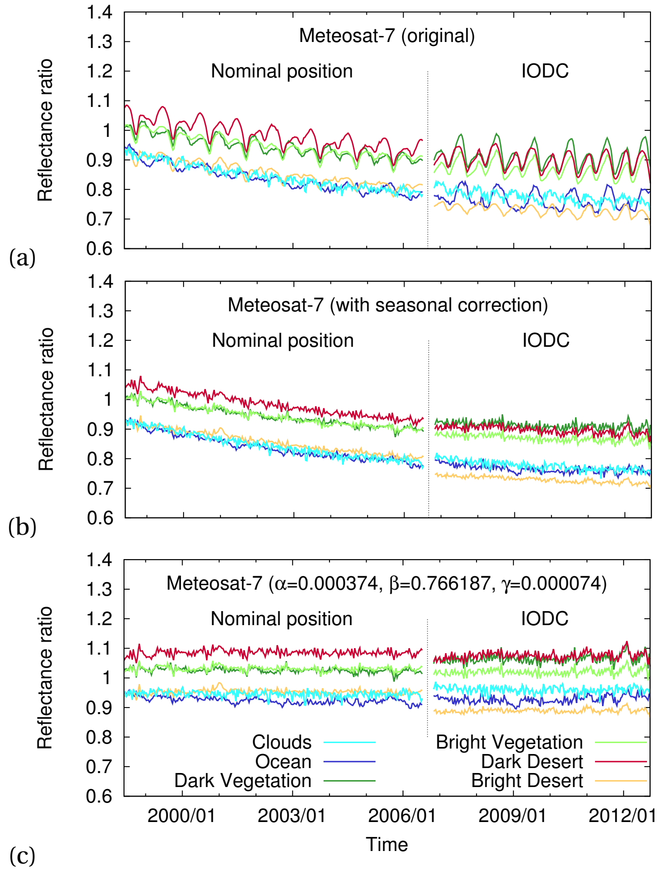

Figure 5.18: Meteosat-7 IODC time series for the data coverage at 0° longitude, and the IODC at 57° E (a) before seasonal correction, (b) after seasonal correction, and (c) after ageing correction.

is done because the GACP dataset only runs until 2006, but as there are no clear effects of volcanic eruptions in the data, this should not be a problem to apply the model.

The time series are corrected for ageing, where again 2×6 time series are used in the minimisation process. The model parameters that come out of the Powell

Table 5.2: The yearly percentage of decrease of the Meteosat-7 IODC time series, before and after ageing correction.

Surface type	before ageing correction	after ageing correction
convective clouds	-0.917 ± 0.047	-0.087 ± 0.0476
ocean	-0.612 ± 0.051	0.263 ± 0.053
dark vegetation	-0.340 ± 0.050	0.205 ± 0.052
bright vegetation	-0.481 ± 0.041	0.102 ± 0.042
dark desert	-0.546 ± 0.046	0.148 ± 0.049
bright desert	-0.698 ± 0.029	0.069 ± 0.031

minimisation method are

$$\begin{aligned} \text{slope} &= -0.0319 \pm 0.0021\,\text{yr}^{-1} \\ \alpha &= 0.000374 \pm 0.00006\,\text{day}^{-1} \\ \beta &= 0.7662 \pm 0.0193 \\ \gamma &= 0.000074 \pm 0.000011\,\mu\text{m}^{-1}\text{day}^{-1}. \end{aligned}$$

These parameters are comparable to the ones found for the 0° time series of Meteosat-7, and are, here too, used to correct the full Meteosat-7 dataset. Figure 5.18(c) shows the ageing corrected time series. The values of the slopes in percentage per year of the aerosol corrected time series at the nominal position are given in Table 5.5 of Section 5.8, while the ones for the IODC (not corrected for aerosols) are given in the Table 5.2.

5.8 DISCUSSION

Figure 5.19(a) shows the ageing corrected time series for all 6 MFG satellites. As no degradation correction was done for Meteosat-6, while the used calibration is the one extrapolated at launch, it has consistently lower values than Meteosat-4, -5 and -7. Furthermore, spectral degradation is clearly present for the Meteosat-6 data, affecting the clear ocean and cloudy time series more than the ones over land. Even though it is not possible to model the ageing based on the 1.5 years of data, the ageing parameters can be derived in such a way that the Meteosat-6 time series agree as closely as possible with the previous (i.e. Meteosat-5) and following (i.e. Meteosat-7) ones. The best consistency is obtained for Meteosat-6

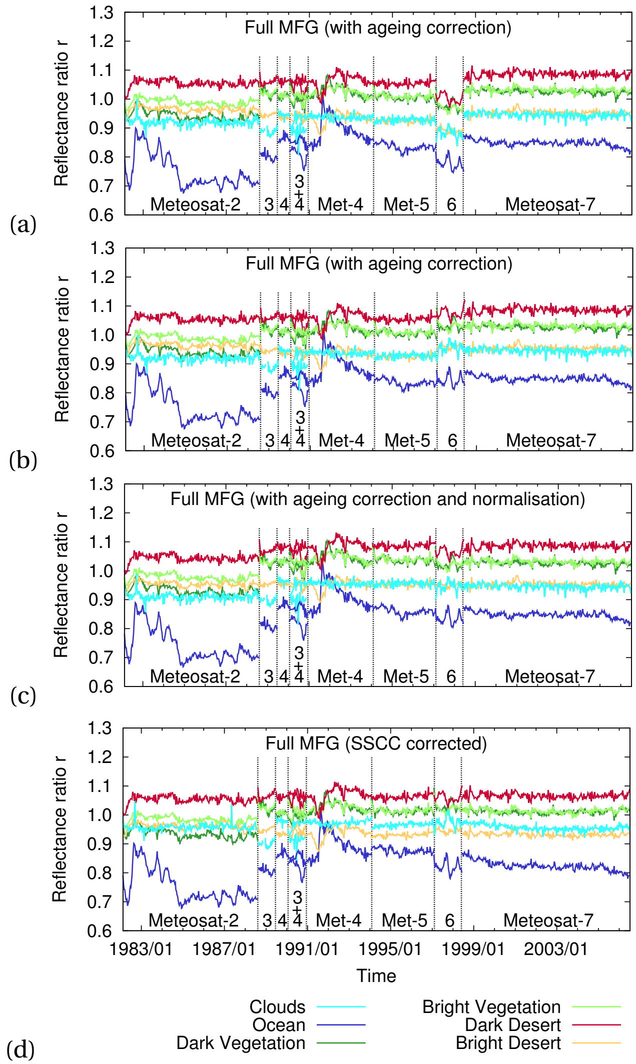

Figure 5.19: The ageing corrected time series with (a) the time series corrected using the minimisation technique for each satellite individually, (b) the same time series, where the parameters of Meteosat-6 have been manually corrected, (c) the normalised time series and (d) the time series corrected using the SSCC method.

Table 5.3: The normalisation coefficients for each satellite with respect to the Meteosat-7 bright desert time series, together with the normalised calibration coefficients.

Satellite	Normalisation coefficient	Normalised calibration
Meteosat-2	0.9889	0.645 / 0.539
Meteosat-3	1.0096	0.634 / 0.764
Meteosat-4	1.0195	0.746
Meteosat-5	1.0303	0.839
Meteosat-6	0.9903	0.829
Meteosat-7	1.0000	0.918

using the following parameters:

$$\begin{aligned}
\text{slope} &= -0.023\,\text{yr}^{-1}\\
\alpha &= 0.000250\,\text{day}^{-1}\\
\beta &= 0.750000\\
\gamma &= 0.000100\,\mu\text{m}^{-1}\text{day}^{-1}.
\end{aligned}$$

Figure 5.19(b) shows these new ageing corrected time series, where, this time, the Meteosat-6 data connect reasonably with the others.

Small shifts are still present in the bright desert time series (which were used for the calibration) of the full MFG database. This is due to the fact that the calibration coefficients of the SSCC method were extrapolated to launch using a linear drift, while the spectral ageing model assumes an exponential change in time. These small shifts are corrected for by normalising the bright desert time series (and so also the calibration coefficients), based on the one of Meteosat-7. Figure 5.19(c) shows the normalised time series, where the normalisation coefficients are given in Table 5.3. This normalisation coefficient lies on average between 1 and 3%, and, as expected, the highest correction is done for Meteosat-5, for which the time between launch and operations was the longest. The normalised calibration coefficients are also added to Table 5.3, which are the calibration coefficients from the SSCC method at launch (see Table 2.1), multiplied by the normalisation coefficients.

The final model parameters used for each of the satellites in Figures 5.19(b) and (c) are shown in Table 5.4. Having a look at the first column, it appears that the slopes are quite variable from one satellite to the other, ranging from about -0.9% up to -3.2% yr^{-1}, where the two oldest instruments seem to have somewhat

Table 5.4: For each satellite, the optimal values for the 4 model parameters, and the square root of the minimised cost function (stddev).

Satellite	slope (yr^{-1})	α ($day^{-1} 10^{-3}$)	β	γ ($\mu m^{-1} day^{-1} 10^{-3}$)	stddev
Meteosat-2	-0.017 ± 0.008	0.44 ± 0.34	0.90± 0.26	0.000 ± 0.000	0.023 ± 0.012
Meteosat-3	-0.009 ± 0.027	0.10 ± 0.29	0.75 (fixed)	0.000 ± 0.396	0.024 ± 0.047
Meteosat-4	-0.026 ± 0.002	0.28 ± 0.08	0.74 ± 0.15	0.049 ± 0.037	0.020 ± 0.014
Meteosat-5	-0.011 ± 0.001	0.12 ± 0.01	0.75 (fixed)	0.055 ± 0.020	0.017 ± 0.003
Meteosat-6	-0.023 ± 0.018	0.25 ± 0.05	0.75 (fixed)	0.100 ± 0.025	0.030 ± 0.001
Meteosat-7	-0.032 ± 0.002	0.37 ± 0.06	0.77 ± 0.02	0.074 ± 0.011	0.017 ± 0.011

smaller slopes than the two newest ones. When it was possible to derive them, β values of about 0.75 were obtained, which represent the asymptotic sensitivity in the ageing model. The higher value for Meteosat-2 (0.90) is characterised by much more uncertainty, which is probably due to the 6-bit digitisation. For the spectral ageing (column 5), relatively similar values are derived for Meteosat-4, -5 and -7, where γ ranges between 0.000049 and 0.000074 $\mu m\, day^{-1}$. In terms of residual standard deviation, the most stable satellite data records after ageing correction are the ones of Meteosat-5 and -7 (about 1.7% at 1σ). Due to the lack of good deseasonalisation, a higher variance is observed for Meteosat-6 (3%). As expected, higher standard deviations are observed for Meteosat-2 and -3 due to the 6-bit digitisation.

From Figure 5.19(c), it is clear that the major trends in the time series have been reduced through the ageing correction. This is confirmed by comparing the values of the slopes before and after the correction in Table 5.5, where the spectral ageing effect has been removed. Apart from Meteosat-2 and -3, all 6 time series are now also at about the same level in Figure 5.19(c). For Meteosat-3 there seems to be a difference in level for the convective clouds and the ocean when comparing with the more recent satellites, while for Meteosat-2 this is mainly the case for the vegetation and the ocean data. Part of this is due to the 6 to 8-bit conversion of these two satellites. Even the lowest electrical currents, observed by these two instruments, arrive at a digital count value of 1 (nothing smaller is possible). On average, these values are more likely equal to about 0.5. In the 6 to 8-bit conversion, all values are multiplied by 4, so that in the 8-bit version, the offset is equal to 4, but might be closer to 2 in reality (Y. Govaerts, pers. comm., September 2013). This effect is largest for the darkest surface types which reflect the least visible radiation, like ocean and vegetation. By decreasing the offset, the darkest time series shift upwards. This has been tested, and indeed, a bet-

Table 5.5: Table giving the amount in % per year that the slopes of fits through the time series change for each MFG satellite before and after ageing correction, together with the standard deviation on these values. The explanation of how these percentages and standard deviations are computed, is given in the Appendix.

Surface type	Meteosat-2 Before	Meteosat-2 After	Meteosat-3 Before	Meteosat-3 After
convective clouds	-0.9411 ± 0.0489	-0.0678 ± 0.0477	-0.8336 ± 0.3232	0.0075 ± 0.3264
ocean	-0.3510 ± 0.1219	0.1316 ± 0.1222	-0.7546 ± 0.3728	-0.1708 ± 0.3769
dark vegetation	-0.7939 ± 0.0659	-0.0262 ± 0.0509	-2.1408 ± 0.2955	-1.4830 ± 0.2999
bright vegetation	-0.5011 ± 0.0426	0.2081 ± 0.0436	-1.7529 ± 0.2232	-1.1043 ± 0.2293
dark desert	-0.3485 ± 0.0474	0.4394 ± 0.0520	-1.6432 ± 0.2326	-0.9330 ± 0.2402
bright desert	-0.5794 ± 0.0437	0.2440 ± 0.0464	-1.2364 ± 0.1558	-0.4679 ± 0.1625
Surface type	**Meteosat-4 Before**	**Meteosat-4 After**	**Meteosat-5 Before**	**Meteosat-5 After**
convective clouds	-2.1375 ± 0.0652	-0.1832 ± 0.0649	-0.8667 ± 0.1033	0.1179 ± 0.1057
ocean	-1.8306 ± 0.1168	0.0407 ± 0.1153	-1.4873 ± 0.1062	-0.6385 ± 0.1413
dark vegetation	-1.1990 ± 0.0880	0.3420 ± 0.0958	-1.1213 ± 0.1158	-0.4815 ± 0.1169
bright vegetation	-1.3130 ± 0.0733	0.2756 ± 0.0812	-1.0542 ± 0.0922	-0.3321 ± 0.0926
dark desert	-1.5212 ± 0.0881	0.2430 ± 0.0939	-0.6019 ± 0.0894	0.2502 ± 0.0903
bright desert	-1.7410 ± 0.0822	0.1453 ± 0.0868	-0.7289 ± 0.0708	0.2000 ± 0.0717
Surface type	**Meteosat-6 Before**	**Meteosat-6 After**	**Meteosat-7 Before**	**Meteosat-7 After**
convective clouds	-0.9775 ± 0.6855	1.0503 ± 0.6779	-1.8838 ± 0.0293	-0.1016 ± 0.0261
ocean	-2.2195 ± 0.7879	-0.3318 ± 0.7890	-2.0222 ± 0.0297	-0.3107 ± 0.0268
dark vegetation	-1.5746 ± 0.6235	-0.3872 ± 0.6344	-1.4012 ± 0.0221	-0.1232 ± 0.0201
bright vegetation	-1.5382 ± 0.4842	-0.1884 ± 0.5002	-1.4073 ± 0.0215	-0.0281 ± 0.0201
dark desert	-1.3293 ± 0.5439	0.2368 ± 0.5553	-1.5427 ± 0.0226	0.01731 ± 0.0236
bright desert	-1.0094 ± 0.2533	0.7208 ± 0.2620	-1.6924 ± 0.0195	-0.0026 ± 0.0209

ter agreement is observed, but it does not solve everything. Another important issue is the pre-launch characterisation of the SR curves of these instruments. If this characterisation was not done accurately enough, it could explain the lower ocean and vegetation time series of Meteosat-2 and -3. However, the investigation is difficult due to the loss of information in the signal quantification of 6 bits. In the next chapter, a study is performed on the Meteosat-7 VIS SR curve at launch, where evidence is shown of a similar, though probably much smaller, problem with the pre-launch characterisation. For the newer satellites (Meteosat-4 till -7), only the dark desert time series of Meteosat-6 is still lower than the others, which is due to the fact that it is difficult to find the right parameters for this satellite.

The overall standard deviation is computed for each scene type to check the long-term stability of the time series. The values are shown in Table 5.6. In the first column, only the data of Meteosat-4 up to 7 are used, as these have the least differences from one satellite to another. The stability ranges here between about 0.9 and 1.6%. Adding Meteosat-2 and -3, leads to values between 0.9 and 6%, with

Table 5.6: The standard deviation of the time series for the Meteosat-4 up to 7 satellites in the first column, and for the Meteosat-2 up to 7 satellites in the second column.

Surface type	Meteosat-4 – 7 (17 yrs)	Meteosat-2 – 7 (24 yrs)
convective clouds	0.0123	0.0239
ocean	0.0167	0.0611
dark vegetation	0.0140	0.0437
bright vegetation	0.0120	0.0266
dark desert	0.0142	0.0230
bright desert	0.0098	0.0099

the largest ones for the dark scenes (ocean and dark vegetation), for all the reasons explained before. Again, the time periods where the eruptions of El Chichón and Pinatubo affect the data most, have not been used in these computations.

As a final step here, the SSCC method is applied to the same targets, in the same way as was done before in Section 4.3.3, where the ocean data are corrected for aerosols. Figure 5.19(d) shows the SSCC corrected time series. The difference for the Meteosat-7 time series is most clearly visible, as explained before: there is a slight bending in the time series corrected using the SSCC model, which is removed by the exponential decay of the spectral ageing model, and the ocean time series decrease more strongly in the SSCC corrected version. The latter is most clearly the case for both Meteosat-6 and -7. Overall, the ocean time series of the Meteosat-4 to -7 satellites are also more connected at about the same reflectance ratio value in Figure 5.19(c), which supports the need of a spectral ageing model.

Chapter Six

Pre-launch characterisation problem of the Meteosat-7 visible spectral response curve

The previous chapters have demonstrated a method to correct the Meteosat First Generation (MFG) visible (VIS) data for spectral degradation by modelling the decrease in time of the pre-launch spectral response (SR) curve in a non-uniform way. As the spectral ageing model is based on this pre-launch SR curve, it is assumed that the characterisation has been done accurately, and is thus trustworthy enough to build a model on. However, the first MFG satellites have been designed already in the seventies, using the at-that-time-available techniques to measure the SRs of the three channels of the Meteosat Visible and Infrared Imagers (MVIRIs). Over the past years, doubts have arisen on the precision of these measurements, leading to the need for further investigations. In this chapter, a first step is taken by comparing the VIS Meteosat-7 data to the more recently and accurately characterised high resolution visible (HRV) Meteosat-8 data. The results shown in this chapter have been published in Decoster et al. (2013b).

6.1 INTRODUCING THE IDEA

As explained in Chapter 1, one way to do vicarious calibration of the VIS channel of a space-born instrument that has no on-board calibration system, is to compare the observed digital count (DC) of a site with a simulation of the radiance that instrument would measure of that same site through that same VIS channel (Koepke 1982*b*, Moulin et al. 1996, Govaerts et al. 2001). To simulate the radiance of an instrument in a specific spectral channel, the SR curve of that instrument's channel needs be taken into account as shown in Eq. (2.5). The precision of the calibration coefficient that is calculated this way, is thus dependent on the

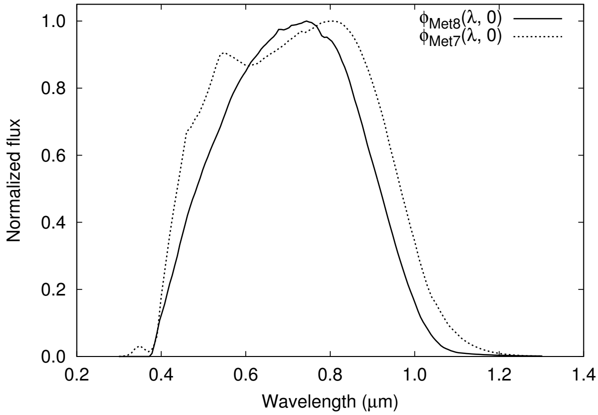

Figure 6.1: The SR curves of the Meteosat-8 HRV channel and the Meteosat-7 VIS channel.

precision of the SR measurement. Govaerts (1999) showed that the pre-launch characterisation of the SR of the Meteosat-5 and -6 VIS bands leads to different calibration coefficients for targets reflecting different amounts of solar radiation. As the Meteosat radiometer responds linearly to the incoming radiance intensity, at time $t = 0$, there should not be such a calibration difference. Since the Meteosat-5 to -7 instruments have similar telescope optics, their silicon detectors were produced in the same batch, and improved techniques were used to measure the Meteosat-7 SR, Govaerts (1999) suggested to use the Meteosat-7 SR curve for the characterisation of the VIS bands of Meteosat-5 and -6 also, as done in the previous chapter. There is even more doubt about the correctness of the pre-launch characterisations of the SRs of the Meteosat-2 to -4 imagers as they were built even earlier than Meteosat-5 and -6.

In the second half of the nineties, the Meteosat Second Generation (MSG) instruments were assembled. The Spinning Enhanced Visible and Infrared Imager (SEVIRI) was built with 4 visible channels, of which 3 are very narrow and 1 is broader. The latter is called the HRV channel and was designed as the successor of the MFG VIS channel. Even though similar telescope optics and silicon detectors were used, the measured SR curves of the Meteosat-8 HRV and the Meteosat-7 VIS channels still look different, especially in the blue part of the spectrum (see Figure 6.1). In Section 1.2.2, it was already mentioned that only part of the MFG VIS channels were characterised by the manufacturers be-

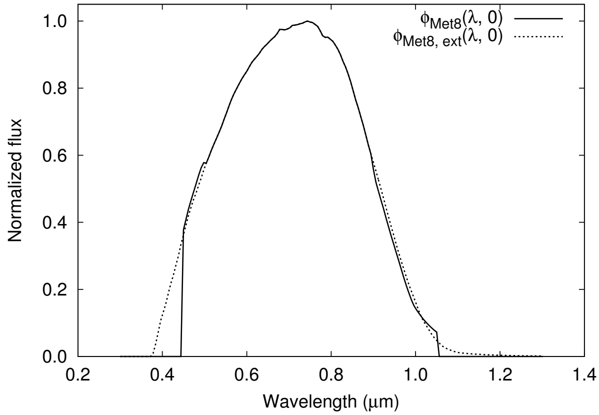

Figure 6.2: The original pre-launch characterised SR curves of the Meteosat-8 HRV channel and the extrapolated version.

fore launch, while the rest was empirically extrapolated. The same is true for the HRV channel of Meteosat-8 and -9, where the measured interval only goes from 0.45 μm to 1.05 μm. Luckily, this was discovered before Meteosat-10 was launched and it was still possible to characterise the SR for the full spectral region (0.378 μm – 1.302 μm). As all MSG detectors were made in the same batch, it was possible to use the HRV SR curve of Meteosat-10 to extrapolate the ones of Meteosat-8 and -9. Figure 6.2 shows the difference between the original and the extrapolated SR curves for the Meteosat-8 HRV channel.

In this chapter, the HRV channel of the first of the MSG series, Meteosat-8, is used as reference to validate the SR curve of the VIS channel of the last of the MFG series, Meteosat-7. There are several reasons why the HRV curve is used to compare with. First of all, as already said before, the MSG HRV channel is the follow-up of the MFG VIS channel, with similar optics and detectors. According to Govaerts et al. (2001), the MSG visible channels have also been significantly better characterised (mean relative uncertainty of about 1%) than the VIS band of the MFG radiometers. On top of that, as Meteosat-7 was part of the transition program between the first and second generation of Meteosat instruments, an overlap was established between Meteosat-7 and -8, leading to 2 years of simultaneous observations when Meteosat-7 was operational at 0° longitude and Meteosat-8 at 3.4° W. Finally, requirements were put on the MSG instrument stability, where the long-term drift of the VIS channels should not exceed 2 % of the maximum dynamic range (Govaerts & Clerici 2003). The limited ageing that is present for Meteosat-8 is expected to still be linear during the first 2 years of operations, and is accounted for as explained hereafter.

6.2 HRV DATA SELECTION

To validate the Meteosat-7 VIS SR curve with the one of the HRV channel of Meteosat-8, the time series of both instruments are compared over the same targets. The Meteosat-7 and -8 observations used, are the 1200 Universal Time Convention (UTC) images for the overlap period when both instruments were operational (February 2004 – July 2006). The Meteosat-7 data are treated in the same way as before (Chapter 4), and similar steps are taken for the Meteosat-8 HRV dataset. This conversion from original DC images to reflectance ratio time series is briefly repeated here for the latter.

In Section 2.2, it was explained how the MFG VIS images were reduced from the original size of 5000×5000 pixels to 2500×2500 by taking the mean value in boxes of 2×2 pixels. This means that the sampling distance at nadir was rescaled from 2.5 km to 5 km. The original HRV images, with a size of 11136×5568 pixels, were reduced to 2500×1250 pixels[1] by averageing out the HRV pixels spatially to the closest VIS pixel. These rescaled HRV images are first converted from DC to radiance L. For Meteosat-8, the calibration coefficient and offset value of each image can be found in its header. These values were changed over time by the European Organization for the Exploitation of Meteorological Satellites (EUMETSAT) to adjust the data for ageing effects. In this study, the calibration coefficient and offset values are kept constant, equal to the ones at launch. Next, the radiance images are converted into reflectance ρ. The filtered solar irradiance (FSI) used in this conversion is calculated in the same way as in Section 2.3, by integrating the product of the solar spectral irradiance $S(\lambda)$ and the HRV SR curve $\phi(\lambda)$:

$$\mathrm{FSI} = \int_{\mathrm{HRV}} S(\lambda)\phi(\lambda)\mathrm{d}\lambda, \tag{6.1}$$

where the integration is done over the full spectral range of the HRV channel.

Based on the Meteosat-8 reflectance images, cloudy and clear-sky targets are selected for both Meteosat-7 and -8. As the HRV images only contain half of the normal Meteosat FOV (see Figure 6.3), only half of the usual pixels is available now. Using the 2 years of HRV images, 219 clear-sky sites are found, which are also shown in Figure 6.3. This means that, for the 2 years of data available for

[1] The HRV field–of–view (FOV) is only half as wide as the normal Meteosat FOV, as shown in Figure 6.3.

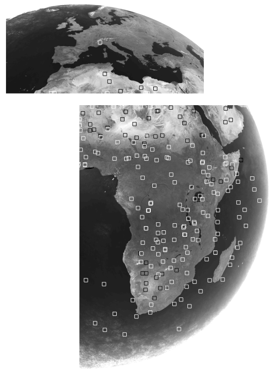

Figure 6.3: The position of the 219 clear-sky targets in the 1200 UTC HRV FOV.

both Meteosat-7 and -8, 220 reflectance time series are created (219 clear-sky + 1 deep convective cloudy). The Meteosat-7 time series are converted from reflectance ρ to reflectance ratio r as shown in Section 2.6, correcting them for ageing using the spectral ageing model and the model parameters from Table 4.2. The Meteosat-8 time series are also converted into reflectance ratio using the exact same simulations in the unfiltering, but without applying the spectral ageing model, i.e. the SR curve is kept fixed at the pre-launch characterised one. By comparing the unfiltered versions of the time series instead of the filtered ones, it is possible to compare time series which are independent of their SR filters. The step from unfiltered reflectance ρ_u to reflectance ratio r for Meteosat-8 is the same as for Meteosat-7 (see Eq. (2.7)), using the same angular distribution models (ADMs) to divide ρ_u with.

6.3 COMPARISON BETWEEN METEOSAT-7 AND -8

Figure 6.4(a) shows the 6 VIS reflectance ratio time series of Meteosat-7, while Figure 6.4(b) shows the HRV time series of Meteosat-8. In the latter some ageing is visible, mainly in the two desert time series. Assuming this ageing is approximately linear over the first few years of operation, to correct for this, a linear first order fit is made through each of the 6 time series. The intercept of this fit at the beginning of operation (February 2004) is the mean value the time series would have if there would be no ageing present. The value of the intercept of each time

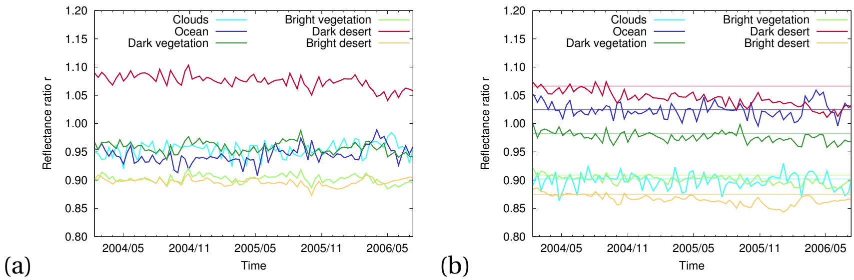

Figure 6.4: Reflectance ratio time series for the 2 years of overlap for (a) Meteosat-7 after ageing correction, and for (b) the original Meteosat-8 time series.

series is indicated in Figure 6.4(b) through horizontal lines[2], each in the colour of the corresponding scene type. It is the value of each of these intercepts that is used as a reference for the Meteosat-7 time series in this chapter. By allowing different slopes for each scene type, the possibility of spectral ageing effects in the HRV channel of Meteosat-8 is taken into account. The Meteosat-8 intercepts are referred to as $\tilde{r}_{\mathrm{M8}}$ in the rest of this chapter. Similar linear first order fits are made through the Meteosat-7 time series, where the intercepts of the fits are written as $\tilde{r}_{\mathrm{M7}}$ and the slopes are very close to zero as the time series are already corrected for ageing. The standard deviation $s(\tilde{r})$ on each intercept is calculated through Eq. (A-1) in the Appendix.

As these intercepts represent the mean value of the non-degrading time series, the comparison study of the Meteosat-7 VIS and Meteosat-8 HRV SR curves, is based on the intercepts of the corresponding time series of both instruments as explained in the following.

6.3.1 RELATIVE INTERCEPT DIFFERENCES

For each different scene type, the relative intercept difference $\Delta\tilde{r}/\tilde{r}$ and its standard deviation, are calculated as

$$\frac{\Delta\tilde{r}}{\tilde{r}} \pm s\left(\frac{\Delta\tilde{r}}{\tilde{r}}\right) = \frac{\tilde{r}_{\mathrm{M7}}-\tilde{r}_{\mathrm{M8}}}{\tilde{r}_{\mathrm{M8}}} \pm \frac{\tilde{r}_{\mathrm{M7}}-\tilde{r}_{\mathrm{M8}}}{\tilde{r}_{\mathrm{M8}}}\sqrt{\left(\frac{s(\tilde{r}_{\mathrm{M7}})}{\tilde{r}_{\mathrm{M7}}}\right)^2+\left(\frac{s(\tilde{r}_{\mathrm{M8}})}{\tilde{r}_{\mathrm{M8}}}\right)^2} \qquad (6.2)$$

[2]Be careful, these are not fits, they just indicate the mean value the time series would have without ageing.

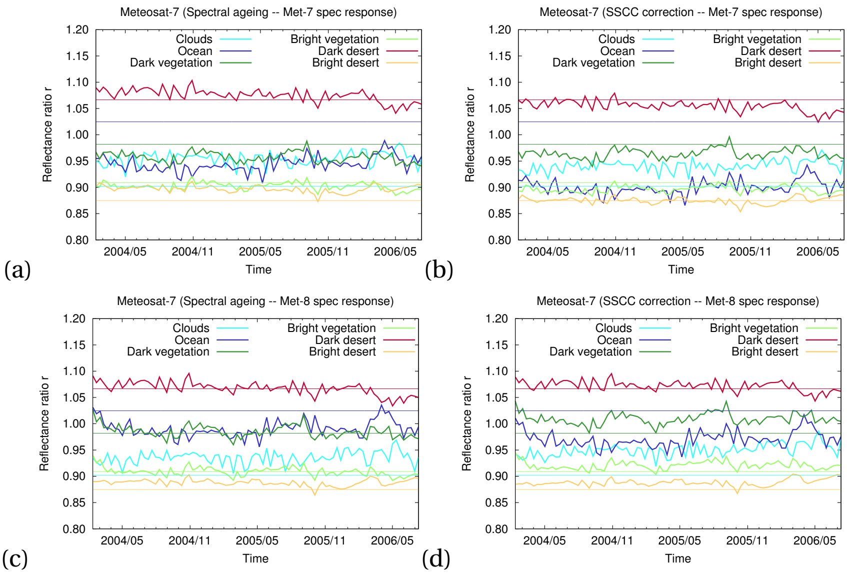

Figure 6.5: The Meteosat-7 time series expressed in reflectance ratio. The horizontal lines show the value of the intercept of the Meteosat-8 time series, used as reference. (a) Meteosat-7 SR curve with spectral ageing. (b) Meteosat-7 SR curve with SSCC correction. (c) Meteosat-8 SR curve with spectral ageing. (d) Meteosat-8 SR curve with SSCC correction.

where $s(\tilde{r}_{\mathrm{M7}})$ and $s(\tilde{r}_{\mathrm{M8}})$ are the standard deviations on the intercepts of the linear fits through respectively the Meteosat-7 and -8 time series of that scene type, again calculated using Eq. (A-1).

In Figure 6.5(a), the same Meteosat-7 reflectance ratio time series are shown as in Figure 6.4(a), but this time together with the horizontal lines from Figure 6.4(b), indicating the reference intercept values of Meteosat-8. From Figure 6.5(a), the intercept differences are clearly visible for each different scene type. The $\Delta\tilde{r}/\tilde{r}$ values are given in the second column of Table 6.1 for all 6 scene types, together with their standard deviations. It can be seen that the discrepancies between Meteosat-7 and -8 lie between +5.3% (for the deep convective clouds) and -8.7% (for clear ocean). For land surface, the difference in reflectance ratio remains lower than 3%. In Table 6.1, also the mean bias $1/n\sum_{i=1}^{n}\Delta\tilde{r}_i/\tilde{r}_i$, mean absolute bias $1/n\sum_{i=1}^{n}|\Delta\tilde{r}_i/\tilde{r}_i|$, and root mean square (RMS) of the intercept differences $\sqrt{1/n\sum_{i=1}^{n}(\Delta\tilde{r}_i/\tilde{r}_i - \text{mean bias})^2}$ are given, with n the number

Scene type	$(\Delta\tilde{r}/\tilde{r})_{s7}$	$(\Delta\tilde{r}/\tilde{r})_{g7}$	$(\Delta\tilde{r}/\tilde{r})_{s8}$	$(\Delta\tilde{r}/\tilde{r})_{g8}$
Clouds	$5.29 \pm 2\times10^{-2}$	$3.57 \pm 1\times10^{-2}$	$3.14 \pm 1\times10^{-2}$	$4.16 \pm 1\times10^{-2}$
Ocean	$-8.67 \pm 3\times10^{-2}$	$-12.7 \pm 4\times10^{-2}$	$-3.69 \pm 1\times10^{-2}$	$-5.71 \pm 2\times10^{-2}$
Dark vegetation	$-2.09 \pm 5\times10^{-3}$	$-2.02 \pm 5\times10^{-3}$	$1.01 \pm 3\times10^{-3}$	$2.62 \pm 7\times10^{-3}$
Bright vegetation	$-0.43 \pm 8\times10^{-4}$	$-1.46 \pm 3\times10^{-3}$	$0.61 \pm 1\times10^{-3}$	$1.24 \pm 3\times10^{-3}$
Dark desert	$2.04 \pm 4\times10^{-3}$	$-0.15 \pm 3\times10^{-4}$	$1.41 \pm 3\times10^{-3}$	$1.23 \pm 2\times10^{-3}$
Bright desert	$2.80 \pm 5\times10^{-3}$	$0.01 \pm 2\times10^{-5}$	$1.70 \pm 3\times10^{-3}$	$1.11 \pm 2\times10^{-3}$
Mean bias	$-0.18 \pm 6\times10^{-3}$	$-2.14 \pm 7\times10^{-3}$	$0.65 \pm 3\times10^{-3}$	$0.73 \pm 4\times10^{-3}$
Mean absolute bias	$3.55 \pm 6\times10^{-3}$	$3.34 \pm 7\times10^{-3}$	$1.88 \pm 3\times10^{-3}$	$2.63 \pm 4\times10^{-3}$
RMS difference	$4.46 \pm 1\times10^{-2}$	$5.05 \pm 2\times10^{-2}$	$2.10 \pm 5\times10^{-3}$	$3.09 \pm 9\times10^{-3}$

Table 6.1: Relative intercept differences, expressed in %, together with their standard deviations. First column: using the Meteosat-7 SR curve and spectral ageing. Second column: using the Meteosat-7 SR curve and the SSCC correction. Third column: using the Meteosat-8 SR curve and spectral ageing. Fourth column: using the Meteosat-8 SR curve and SSCC correction.

of time series. While the mean bias is almost equal to zero, the mean absolute bias is equal to 3.5% and the root mean square to 4.5%.

In a second step, as a validation of the spectral ageing model, the Meteosat-7 data are now corrected for ageing using the SSCC method of Govaerts et al. (2004) instead of the spectral ageing model. This is done in the same way as was explained in Section 4.3.3. The resulting Meteosat-7 time series are shown in Figure 6.5 (b), again with the Meteosat-8 intercepts as reference on top of it. In Section 4.3.3 it was already shown that the ocean time series are not corrected well enough using the SSCC correction. This is clear here too, as the difference between the Meteosat-7 ocean time series and the Meteosat-8 reference is even bigger when corrected with the SSCC method instead of the spectral ageing model. In the third column of Table 6.1, the values for these intercept differences for the SSCC corrected time series are shown, together with their standard deviations. Comparing the bias and RMS values from the first and second columns shows that the use of the spectral ageing model leads to a better agreement between Meteosat-7 and Meteosat-8. The higher values using the SSCC method are explained both by the fact that a linear decrease in signal is assumed instead of an exponential one, and by the non-correction of the spectral component of the ageing. Whichever ageing correction method is used, however, the ocean and the cloud signal are clearly lower and higher, respectively, than the corresponding Meteosat-8 values. This could be an indication of an overestimation of the instrument's sensitivity in the shortest wavelengths (explaining the negative ocean difference) and an underestimation in the middle of the VIS band (explaining the positive cloud difference). As the Meteosat-7 SR curve has only been characterised in the 0.5 – 0.9 μm interval, and the rest has been extrapolated, it is not surprising that this extrapolation might not be correct and could be the cause of the strong differences between Meteosat-7 and -8 in the blue part of the spectrum.

The Meteosat-7 VIS channel and Meteosat-8 HRV channel were built very similarly. For that reason, the Meteosat-7 VIS SR curve is now replaced by the Meteosat-8 HRV curve to see if this improves the results. As the Meteosat-8 SR curve is narrower than the one of Meteosat-7, the calibration coefficient is multiplied by the ratio of the band integrated solar irradiation for both filters (0.85). This means that the FSI using the Meteosat-8 HRV SR curve is divided by the FSI using the Meteosat-7 VIS SR curve at launch. The resulting time series are shown in Figure 6.5(c) and 6.5(d), where the Meteosat-7 data have been corrected for ageing using the spectral ageing model and the SSCC correction method, respectively. The intercept differences and their standard deviations are given in the fourth and fifth column of Table 6.1. Replacing the Meteosat-7 SR curve with the one of Meteosat-8, clearly improves the consistency between the two instruments. For the spectral ageing model, the replacement decreases the RMS from

4.5% to 2.1%. A similar improvement is observed for the mean absolute bias. Over the 6 scene types, the discrepancy between Meteosat-7 and 8 is now in the range of +3.1% to -3.7%. Using the SSCC method, replacing the Meteosat-7 SR curve with the Meteosat-8 curve leads to the same improvement, though slightly less. Interestingly, it can be seen from Figure 6.2 that the pre-launch SR curve of the Meteosat-7 VIS channel presents a higher sensitivity in the blue (around 0.4 μm) and a lower sensitivity in the center of the channel (0.6 – 0.8 μm) when compared to the curve of the Meteosat-8 HRV channel, which confirms the idea of a possible overestimation of the pre-launch Meteosat-7 SR curve at the shortest wavelengths and an underestimation in the middle of the curve.

6.3.2 CALCULATION OF METHOD UNCERTAINTY

The four major sources contributing to the uncertainty on $\Delta\tilde{r}/\tilde{r}$ are: i) an uncertainty ϵ_{u} introduced by the unfiltering, ii) the relative standard deviation on the relative intercept differences, ϵ_{r}, iii) the uncertainty on the Meteosat-8 HRV SR curve, ϵ_{s}, and finally, iv) the uncertainty ϵ_{a} due to the ageing method used to correct the Meteosat-7 data.

First of all, the relative uncertainty ϵ_{u}, introduced by the conversion from filtered to unfiltered radiances (Eq. (2.4)), is calculated. The conversion itself introduces uncertainties of about 4% for both Meteosat-7 and -8. This is calculated as follows. To be able to find the unfiltering coefficients a and b in Eq. (2.4), filtered and unfiltered radiances are computed from simulations (Eqs. (2.5) and (2.6)), where the filtered radiances take into account the SR curve of both instruments. These simulated radiances are converted into reflectances, and then for both Meteosat-7 and -8, the regressions are fitted to get the (a_7, b_7) and (a_8, b_8) coefficients respectively. The uncertainty on the conversion is then the difference between the simulated unfiltered radiances (ρ_{u}) used to do the fitting, and the calculated unfiltered radiances for both Meteosat-7 and -8 ($\rho_{\mathrm{u},7}$ and $\rho_{\mathrm{u},8}$), computed from the observations using the fitted (a_7, b_7) and (a_8, b_8) coefficients. This results in:

$$\sigma_7 = \sqrt{\frac{1}{m}\sum_{i=1}^{m}(\rho_{i(\mathrm{u},7)} - \rho_{i(\mathrm{u})})^2} \qquad (6.3)$$

$$\sigma_8 = \sqrt{\frac{1}{m}\sum_{i=1}^{m}(\rho_{i(\mathrm{u},8)} - \rho_{i(\mathrm{u})})^2} \qquad (6.4)$$

where σ_7 is the standard deviation calculated for the Meteosat-7 VIS data, σ_8 is the standard deviation calculated for the Meteosat-8 HRV data, and m is the number of data points used, which is the same for both time series. The values of the relative uncertainties $\epsilon_{\mathrm{u}7}$ and $\epsilon_{\mathrm{u}8}$ (divided by the mean of the calculated

Scene type	ϵ_{u7}	ϵ_{u8}	ϵ_u	ϵ_s
Clouds	3.66	3.78	0.17	0.35
Ocean	2.71	3.46	0.87	0.94
Dark vegetation	3.46	3.46	0.75	0.45
Bright vegetation	4.27	4.18	1.26	0.24
Dark desert	4.59	4.67	0.74	0.20
Bright desert	4.15	4.18	0.53	0.27
Mean	3.81	3.95	0.72	0.42

Table 6.2: The relative standard deviations on the different sources of uncertainty in this method, expressed in percentage.

Meteosat-7 unfiltered reflectances) are given in columns 2 and 3 of Table 6.2 for the different scene types. In this chapter, however, it is not the reflectance itself that is being used, but the difference between the Meteosat-7 and -8 values. As the uncertainties of both instruments are highly correlated because their SR curves are so alike, only about 0.7% of standard deviation remains in the difference in reflectance ratio $\Delta\tilde{r}/\tilde{r}$, calculated as

$$\sigma_{78} = \sqrt{\frac{1}{m}\sum_{i=1}^{m}(\rho_{i(\mathrm{u},7)} - \rho_{i(\mathrm{u},8)})^2} \tag{6.5}$$

where σ_{78} is the standard deviation on the difference of the Meteosat-7 and -8 reflectance values. The relative standard deviation ϵ_u (σ_{78} / $\langle\rho_{i(\mathrm{u},7)}\rangle$) is given in the fourth column of Table 6.2 for the 6 different time series.

The relative standard deviations on the intercepts of Meteosat-7 and -8 were already computed before and shown in Table 6.1. These values were computed with Eq. (A-1), leading to the values $s(\tilde{r}_{M7})$ and $s(\tilde{r}_{M8})$ for Meteosat-7 and -8 respectively. Using Eq. (6.2), these standard deviations are converted into the relative standard deviation ϵ_r on the relative intercept difference. As these uncertainties are small compared to the other contributions, the maximum value is used in this uncertainty budget, $\epsilon_r = 0.04\%$.

An extra uncertainty ϵ_s is introduced by the Meteosat-8 HRV SR characterisation. Govaerts et al. (2001) gives the uncertainty on the 4 SEVIRI VIS channels, including the HRV. This shows that there is a maximum uncertainty of 2% on the HRV SR curve. The effect on $\Delta\tilde{r}/\tilde{r}$ is calculated by adding this uncertainty to the HRV SR curve and comparing the results with the original one. The uncertainty is added to the SR curve by multiplying the left half of the curve with 1.02 and the right half with 0.98. This way, for bright desert (the target used for the calibration), the same amount of energy is observed, but the calibration does not annihilate the effect of adding the uncertainty. To find the uncertainty this introduces for the relative intercept difference, the filtered radiances are simulated for both the original HRV SR curve (L_f) and the one with the added uncertainty of 2% ($L_\mathrm{f+unc}$). The unfiltering then leads to different a and b coefficients for both versions of the SR curves, and thus the observed filtered reflectances will be converted into different unfiltered reflectances: ρ_u for the original SR curve and $\rho_\mathrm{u+unc}$ for the one with the added uncertainty. This difference then results in the standard deviation σ

$$\sigma = \sqrt{\frac{1}{m}\sum_{i=1}^{m}(\rho_{i(\mathrm{u})} - \rho_{i(\mathrm{u+unc})})^2} \tag{6.6}$$

where m is the number of data points. The relative uncertainty values ϵ_s are given in the fourth column in Table 6.2 for each different time series.

Finally, from the fifth and sixth columns of Table 4.1, it can be seen that the residual drift of the Meteosat-7 time series is evaluated as better than 0.17% yr^{-1} for the spectral ageing model, and 0.62% yr^{-1} for the SSCC correction. This means that the maximum uncertainty ϵ_a due to the spectral ageing model is about 1% after 6 years and for the SSCC correction about 3.7%.

The four uncertainty sources are combined using the root square ($\epsilon = \sqrt{\epsilon_\mathrm{u}^2 + \epsilon_\mathrm{r}^2 + \epsilon_\mathrm{s}^2 + \epsilon_\mathrm{a}^2}$), and are shown in Table 6.3. The combined uncertainty, approximately 1.4% using the spectral ageing model, and 3.8% using the SSCC correction, represents the total uncertainty on the methodology used in this chapter. When using the spectral ageing model in the comparison, the RMS of the relative intercept differences are still higher than the total uncertainty of 1.4%, so that the observed differences between the Meteosat-7 and -8 time series must be attributed to the pre-launch Meteosat-7 SR characterisation $\phi(\lambda, 0)$. The same is valid using the SSCC method.

6.3.3 SENSITIVITY TO SCENE TYPE DEFINITION

As an additional verification, the 219 clear-sky targets are regrouped into 10 time series, representing 10 of the 17 surface types from the International Geosphere / Biosphere Programme (IGBP). The relative intercept differences between Meteosat-7 and 8 for these 10 clear-sky + 1 cloudy time series are provided in Table 6.4, where the exact same process was done as before, switching between the spectral ageing model and the SSCC correction and using the Meteosat-7 VIS SR curve and the Meteosat-8 HRV SR curve. The same cloudy time series was used as before, and, as the clear-sky targets are still the same and there is only one type of ocean in the IGBP system, the ocean time series also has not changed. The RMS differences are all slightly smaller than they were us-

Scene type	spectral ageing model	SSCC method
Clouds	1.07	3.72
Ocean	1.63	3.91
Dark vegetation	1.33	3.80
Bright vegetation	1.63	3.92
Dark desert	1.26	3.78
Bright desert	1.16	3.75
Mean	1.35	3.81

Table 6.3: The total uncertainty on the method, expressed in percentage, for both the spectral ageing model and the SSCC method.

ing the Clouds and Earth's Radiant Energy System (CERES) subdivision, which might point to the fact that 5 clear-sky surface types are not enough to represent the Meteosat FOV.

Scene type	$(\Delta\tilde{r}/\tilde{r})_{s7}$	$(\Delta\tilde{r}/\tilde{r})_{g7}$	$(\Delta\tilde{r}/\tilde{r})_{s8}$	$(\Delta\tilde{r}/\tilde{r})_{g8}$
Clouds	$5.29 \pm 2\times10^{-2}$	$3.57 \pm 1\times10^{-2}$	$3.14 \pm 1\times10^{-2}$	$4.16 \pm 1\times10^{-2}$
Ocean	$-8.67 \pm 3\times10^{-2}$	$-12.7 \pm 4\times10^{-2}$	$-3.69 \pm 1\times10^{-2}$	$-5.71 \pm 2\times10^{-2}$
Evergreen broadleaf forest	$-1.03 \pm 3\times10^{-3}$	$-0.83 \pm 2\times10^{-3}$	$1.95 \pm 5\times10^{-3}$	$3.67 \pm 1\times10^{-2}$
Closed shrublands	$-1.89 \pm 7\times10^{-3}$	$-3.16 \pm 1\times10^{-2}$	$0.37 \pm 1\times10^{-3}$	$0.80 \pm 3\times10^{-3}$
Open shrublands	$1.00 \pm 2\times10^{-3}$	$-0.84 \pm 2\times10^{-3}$	$1.05 \pm 2\times10^{-3}$	$1.14 \pm 2\times10^{-3}$
Woody savannas	$-1.29 \pm 3\times10^{-3}$	$-1.58 \pm 3\times10^{-3}$	$1.22 \pm 3\times10^{-3}$	$2.51 \pm 6\times10^{-3}$
Savannas	$-0.34 \pm 7\times10^{-4}$	$-1.24 \pm 3\times10^{-3}$	$0.93 \pm 2\times10^{-3}$	$1.69 \pm 4\times10^{-3}$
Grasslands	$0.76 \pm 2\times10^{-3}$	$-0.86 \pm 2\times10^{-3}$	$0.83 \pm 2\times10^{-3}$	$1.06 \pm 2\times10^{-3}$
Croplands	$0.83 \pm 2\times10^{-3}$	$-0.45 \pm 1\times10^{-3}$	$1.43 \pm 4\times10^{-3}$	$1.88 \pm 5\times10^{-3}$
Cropland/natural vegetation mosaic	$-0.51 \pm 1\times10^{-3}$	$-1.18 \pm 3\times10^{-3}$	$1.07 \pm 3\times10^{-3}$	$2.04 \pm 5\times10^{-3}$
Barren or sparsely vegetated	$2.51 \pm 5\times10^{-3}$	$-0.04 \pm 3\times10^{-5}$	$1.44 \pm 3\times10^{-3}$	$1.04 \pm 2\times10^{-3}$
Mean bias	$-0.30 \pm 3\times10^{-3}$	$-1.76 \pm 4\times10^{-3}$	$0.89 \pm 2\times10^{-3}$	$1.30 \pm 2\times10^{-3}$
Mean absolute bias	$2.19 \pm 3\times10^{-3}$	$2.41 \pm 4\times10^{-3}$	$1.56 \pm 2\times10^{-3}$	$2.34 \pm 2\times10^{-3}$
RMS difference	$3.27 \pm 1\times10^{-2}$	$3.79 \pm 1\times10^{-2}$	$1.60 \pm 4\times10^{-3}$	$2.45 \pm 6\times10^{-3}$

Table 6.4: Relative intercept differences, expressed in %, together with their standard deviations for IGBP surface classification. First column: using the Meteosat-7 SR curve and spectral ageing. Second column: using the Meteosat-7 SR curve and SSCC correction. Third column: using the Meteosat-8 SR curve and spectral ageing. Fourth column: using the Meteosat-8 SR curve and SSCC correction.

Chapter Seven

Conclusions and future prospects

7.1 CONCLUSIONS

Validation of the official SEVIRI Solar Channel Calibration (SSCC) of the visible (VIS) channel of the Meteosat Visible and Infrared Imagers (MVIRIs) onboard the Meteosat First Generation (MFG) satellites, has proven the need of a spectral component for the in-flight degradation correction. This work presents a spectral ageing model which simulates the degradation induced decrease of the spectral response (SR) of these imagers. Based on 3 parameters, the model allows the SR curve, as it was characterised before launch, to decrease exponentially in time and linearly in wavelength, with a stronger component in the short wavelengths than the longer ones. The model parameters quantify for each satellite how strong the degradation is. To find the values of these parameters, a large amount of time series with different spectral characteristics are used. Each of these time series is created for a target, selected in the Meteosat field–of–view (FOV), with a low variability in time. The best set of model parameters then allows the spectral ageing model to explain the degradation of the VIS MVIRI data.

A theoretical comparison study is done for Meteosat-7, based on simulations, showing the difference between the spectral ageing model and the current official SSCC method for five different essential climate variables (ECVs). The difference between both degradation correction methods is largest for the retrieval of background aerosol optical depth (AOD) over ocean, land surface albedo over vegetation and broadband radiances over clear-sky land and ocean surfaces. For these ECVs, biases were estimated between 2 and 5% after 8 years of in-flight degradation. The three main conclusions coming out of this study are the following. First of all, the effect of using one method instead of the other is opposite over clear ocean than clear land due to the presence (or absence) of the spectral component in the spectral ageing correction (or SSCC correction). A second effect is introduced by the difference in degradation rate for both methods, leading to an overall bias for scene types reflecting over the full VIS wavelength range (clouds and clear-sky land). Finally, the use of variables where the effect of clear-sky radiances has been subtracted from, results in a decrease of bias (e.g. cloud cover index).

Next, the model is applied to the full VIS MFG database (Meteosat-2 till 7). Some additional problems were encountered during the process, e.g. the volcanic eruptions of El Chichón (Meteosat-2) and Pinatubo (Meteosat-4), and the 6-bit digitisation and saturation for Meteosat-2 and -3. The effect of volcanic aerosols over ocean was partly compensated for using the AOD dataset from the Global Aerosol Climatology Project (GACP). Except for Meteosat-6, the Powell minimisation method was able to find model parameters for all MFG satellites, even though for Meteosat-2 and -3 it was not possible to quantify the spectral degradation. For Meteosat-6, parameters were found by comparing the time series to the ones of Meteosat-5 and -7 instead. The resulting long-term stability in the corrected time series is equal to about 1–2% for Meteosat-4 up to -7, but increases up to 6% when adding the Meteosat-2 and -3 time series. The reason for this increase is a combination of the signal digitisation on only 6 bits, which affected the offset and thus the time series of the darkest scene types, and a pre-launch SR characterisation with a significantly larger uncertainty, affecting the ocean and/or cloudy time series. As long as the 6-bit digitisation problem and the saturation are not corrected, it is not recommended to use the Meteosat-2 and -3 time series in fundamental climate data records (FCDRs) and thematic climate data records (TCDRs) for the VIS channel. Preliminary investigations have been done for the digitisation problem by adjusting the offset of these two satellites. This shows that it is possible to improve the results this way, but that it is not sufficient, probably due to the lack of a good SR characterisation.

Finally, a side-track was taken to investigate a possible future study on the accuracy of the pre-launch characterised SR curves of the VIS channel of the MVIRI instruments. The simultaneous observation time series (2004–2006) of the Meteosat-7 VIS and Meteosat-8 high resolution visible (HRV) channels have been compared to validate the Meteosat-7 VIS SR curve. Although the overall agreement is good, differences are observed when looking at individual scene types. Using the official pre-launch characterised SR curve of Meteosat-7 and the SSCC calibration, the root mean square (RMS) of the difference is 5.2% between the two satellites. Using the spectral ageing model instead, this RMS decreases to 4.5%. Given that the comparison methodology uncertainty is about 1.4% for the spectral ageing model, this indicates that there is a problem with the pre-launch characterisation of the Meteosat-7 SR curve. Better agreements are obtained when replacing the Meteosat-7 SR curve by the one of Meteosat-8. In this case, the RMS is reduced to 2.1% with the spectral ageing model. This indicates that the SR of the Meteosat-7 VIS band could be better represented by the SR curve of the Meteosat-8 HRV channel.

7.2 FUTURE PROSPECTS

7.2.1 GENERATE TCDRS AND FCDR

The spectral ageing model can be used to derive FCDRs and TCDRs from the Meteosat data in different ways. In this work, the unfiltering has been done using a SR curve equal to 1 over the full wavelength region. This is useful for the top of the atmosphere (TOA) radiation TCDR of the full MVIRI VIS dataset. Instead of doing a theoretical unfiltering using simulations, it is also possible to empirically derive the unfiltering relation from the unfiltered Geostationary Earth Radiation Budget (GERB) shortwave (SW) data and the (filtered) Meteosat-7 VIS data for the overlap period from 2004 until 2006. This empirical unfiltering will be used in the near future to create the MVIRI TCDR for the Climate Monitoring Satellite Application Facility (CM SAF). Another way to use the model could be to do the unfiltering using a reference SR curve like, for example, the Meteosat-7 prelaunch characterised SR, or the Meteosat-8 HRV SR curve. This will create a stable record of Meteosat images. As, with respect to the original level 1.5 images, the ageing corrections will be small, in this case it might be better to express the TCDRs of TOA radiation in reflectance ρ instead of digital count (DC). This way, the discretisation effect will disappear, and the ageing correction will be done in floating point. Finally, the spectral ageing model can also be provided in its raw format, with the right model parameters for each satellite. Even though this is more complicated for the user, the model can be applied to create look-up tables (LUTs) that vary in time for ECV retrieval of, for example, aerosol properties, or cloud properties where the full corrected images are not necessary (see Section 4.4).

7.2.2 IMPROVE THE METEOSAT-2 AND -3 RESULTS

From the conclusions it was clear that several problems hamper the use of the original version of the VIS Meteosat-2 and -3 dataset (digitisation, saturation, SR characterisation). The digitisation problem is worst for the darkest scenes (i.e. ocean and dark vegetation), which makes it difficult to derive, for example, AOD over ocean. The TOA radiation product of CM SAF is less sensitive to this dark signal, so in an iterative process the offset will be tuned to get the best overall agreement and the most stable dataset. As this product will be delivered as daily and monthly means, the effect of the digitisation will probably be significantly reduced. The saturation problem could be dealt with by correcting the saturated pixel values for the calibration difference (see Section 5.1.4).

7.2.3 IMPROVE PRE-LAUNCH SR CURVE CHARACTERISATION

When creating climate data records, for now, it is suggested for Meteosat-7 to replace the pre-launch SR curve with the one of the Meteosat-8 HRV channel to have a better interpretation of the Meteosat-7 data record and to improve the consistency with Meteosat-8. It would, however, be better to actually correct the pre-launch SR curve of Meteosat-7. For this, the SCanning Imaging Absorption spectrometer for Atmospheric CHartographY (Sciamachy) could be used as a reference source. This spectroradiometer takes spectra of the Earth in a polar orbit through 8 channels. Sciamachy was operational between 2002 and 2012, and so it could be used to check the SR curves of Meteosat-5 and -6 (using Indian Ocean data coverage (IODC) data) and Meteosat-7. This could be done in the following way. For a certain site,

$$L_{\mathrm{Sc}} = \int L_{\mathrm{Sc}}(\lambda)\,\phi_{\mathrm{MFG}}(\lambda, t)\,d\lambda \tag{7.1}$$

could be compared with the observed MVIRI radiance L_{MFG}. In this equation, $L_{\mathrm{Sc}}(\lambda)$ is the spectral radiance derived from the Sciamachy measurements and $\phi_{\mathrm{MFG}}(\lambda, t)$ is the spectral degradation model. Any differences between these values, must come from the SR curve used in Eq. (7.1), and this way an optimisation of the shape of the SR could in theory be feasible. Such a study could either be based on a set of SR curves for similar instruments like Geostationary Operational Environmental Satellites (GOES), Meteosat Second Generation (MSG)HRV channel, etc., or on a gaussian shape by adjusting some parameters.

Appendix

To determine how strong a time series is degrading in time, residual or original, a least squares fit is made. As the degradation can be approximated by a linear function, these fits have the form

$$f(t) = a + b\,t$$

where a is the intercept of the fit and b is the slope (yr^{-1}). What is most interesting to know about degrading time series is their relative slope. Expressed in percentage per year, the relative slope of $f(t)$ is equal to

$$\Delta f(t) = \frac{100 \times b}{a}.$$

To know the precision of $\Delta f(t)$, its standard deviation is calculated through the standard deviations of a and b. Following Kutner et al. (2005), the standard deviation on the intercept and slope are given by

$$\sigma(a) = \sigma\sqrt{\frac{1}{n} + \frac{\bar{X}^2}{\sum_{i=1}^{n}\left(X_i - \bar{X}\right)^2}} \tag{A-1}$$

$$\sigma(b) = \frac{\sigma}{\sqrt{\sum_{i=1}^{n}\left(X_i - \bar{X}\right)^2}} \tag{A-2}$$

respectively, where σ is the standard deviation of the fit through the time series, n is the number of data points in the time series, and i runs over the n data points. Through the rules of error propagation of a division, the standard deviation of $\Delta f(t)$ is equal to

$$\sigma(\Delta f(t)) = \Delta f(t)\sqrt{\left(\frac{\sigma(a)}{a}\right)^2 + \left(\frac{\sigma(b)}{b}\right)^2} \tag{A-3}$$

by filling in Equations (A-1) and (A-2).

Bibliography

Aristotle (350 BC), *Μετεωρολογικων*, Vol. Book 1, Part 1, Translated by E. W. Webster, Ancient Greece.

Arriaga, A. & Schmetz, J. (1999), 'Calibration of the Meteosat-5/-6 VIS channels with help of modelled radiances', *Contributions to atmospheric physics* **72**(2), 133–139.

Baldridge, A. M., Hook, S. J., Grove, C. I. & Rivera, G. (2009), 'The ASTER spectral library version 2.0', *Remote Sensing of Env.* **113**, 711–715.

Bertrand, C., Clerbaux, N., Ipe, A., Dewitte, S. & Gonzalez, L. (2006), 'Angular distribution models anisotropic correction factors and sun glint: a sensitivity study', *Int. J. Remote Sensing* **27**(9), 1741–1757.

Bremer, J. C., Baucom, J. G., Vu, H., Weinreb, M. P. & Pinkine, N. (1998), Estimation of long-term throughput degradation of GOES-8 & 9 visible channels by statistical analysis of star measurements, *in* 'Proceedings of SPIE', Vol. 3439, SPIE, San Diego, California, pp. 145–154.

Brohan, P., Kennedy, J. J., Harris, I., Tett, S. F. & Jones, P. D. (2006), 'Uncertainty estimates in regional and global observed temperature changes: A new data set from 1850', *Journals of Geophysical Research: Atmospheres (1984–2012)* **111**(12).

Brooks, D. R., England, C. F., Hunt, G. E. & Minnis, P. (1984), 'An intercalibration of Meteosat-1 and GOES-2 visible and infrared measurements', *J. Atmos. Oceanic Technol.* **1**(3), 283–286.

Bugliaro, L., Zinner, T., Keil, C., Mayer, B., Hollman, R., Reuter, M. & Thomas, W. (2011), 'Validation of cloud property retrievals with simulated satellite radiances: a case study for SEVIRI', *Atmospheric Chemistry and Physics* **11**, 5603–5624.

Burroughs, W. J. (2007), *Climate change: a multidisciplinary approach*, 2nd edn, Cambridge University Press, Cambridge, UK.

Cabot, F., Dedieu, G. & Maisongrande, P. (1994), Monitoring NOAA/AVHRR and Meteosat shortwave bands calibration and inter calibration over stable areas, *in* 'Physical Measurements and Signatures in Remote Sensing Proc. 6th ISPRS Symp', ISPRS, Val d'Isère, France, pp. 41–46.

Cano, D., Monget, J. M., Albuisson, M., Guillard, H., Regas, N. & Wald, L. (1986), 'A method for the determination of the global solar radiation from meteorological satellite data', *Solar Energy* **37**(1), 31–39.

Chin, M., Chu, A., Levy, R., Remer, L., Kaufman, Y., Holben, B., Eck, T., Ginoux, P. & Gao, Q. (2004), 'Aerosol distribution in the northern hemisphere during ACE-Asia: Results from global model; satellite observations, and Sun photometer measurements', *Journal of Geophysical Research* **109**(D23S90).

Clerbaux, N., Dewitte, S., Bertrand, C., Caprion, D., Paepe, B. D., Gonzalez, L., Ipe, A., Russell, J. E. & Brindley, H. (2008), 'Unfiltering of the geostationary earth radiation budget (GERB) data. part i: Shortwave radiation', *J. Atmos. Oceanic Technol.* **25**(7), 1087–1105.

Darmont, A. (2009), 'Spectral response of silicon image sensors', *White Paper* .

De Paepe, B. & Dewitte, S. (2009), 'Dust aerosol optical depth retrieval over desert surface, using the SEVIRI window channels', *Advances in Space Research* **26**, 704–718.

Decoster, I., Clerbaux, N., Baudrez, E., Dewitte, S., Ipe, A., Nevens, S., Blazquez, A. V. & Cornelis, J. (2013), 'Modeling the aging effects of Meteosat-7 visible band', *JAOT* **30**(3), 496–509.

Decoster, I., Clerbaux, N., Govaerts, Y. M., Baudrez, E., Dewitte, S., Ipe, A., Nevens, S., Blazquez, A. V. & Cornelis, J. (2013b), 'Evidence of pre-launch characterization problem of Meteosat-7 visible spectral response curve', *Remote Sensing Letters* **4**(10), 1008–1017.

Delwart, S., Preusker, R., Bourg, L., Santer, R., Ramon, D. & Fischer, J. (2006), MERIS in-flight spectral calibration, *in* 'Proc. of the Second Working Meeting on MERIS and AATSR Calibration and Geophysical Validation', ESA, Frascati, Italy.

Dewitte, S., Gonzalez, L., Clerbaux, N., Ipe, A., Bertrand, C. & Paepe, B. D. (2008), 'The geostationary earth radiation budget edition 1 data processing algorithms', *Advances in Space Research* **41**(11), 1906–1913.

Doelling, D. R., Hong, G., Morstad, D., Bhatt, R., Gopalan, A. & Xiong, X. (2010), The characterization of deep convective cloud albedo as a calibration target using MODIS reflectances, *in* 'Proc. SPIE 7862, Earth Observing Missions and Sensors: Development, Implementation, and Characterization', SPIE, Incheon, Republic of Korea, pp. CD–ROM.

Doelling, D. R., Nguyen, L. & Minnis, P. (2004), On the use of deep convective clouds to calibrate AVHRR data, *in* 'Proc. of SPIE', Vol. 5542, SPIE, Gran Canaria, Spain.

Dooling, D. & Finckenor, M. M. (1999), Material selection guidelines to limit atomic oxygen effects on spacecraft surfaces, Nasa/tp-1999-209260, NASA.

Dozier, J. (1989), 'Spectral signature of Alpine snow cover from the Landsat thematic mapper', *Remote Sensing of Env.* **28**, 9–22.

Eastman, R., Warren, S. G. & Hahn, C. J. . (2011), 'Variations in cloud cover and cloud types over the ocean from surface observations, 1954–2008', *Journal of Climate* **24**(22), 5914–5934.

Edwards, D. P., Emmons, L. K., Hauglustaine, D. A., Chu, D. A., Gille, J. C., Kaufman, Y. J., Petron, G., Yurganov, L. N., Giglio, L., Deeter, M. N., Yudin, V., Ziskin, D. C., Warner, J., Lamarque, J.-F., Francis, G. L., Ho, S. P., Mao, D., Chen, J., Grechko, E. I. & Drummond, J. R. (2004), 'Observations of carbon monoxide and aerosols from the Terra satellite: Northern hemisphere variability', *Journal of Geophysical Research* **109**(D24202).

Eidenshink, J. C. & Faundeen, J. L. (1994), 'The 1 km AVHRR global land data set: first stages in implementation', *Int. J. Remote Sensing* **15**(17), 3443–3462.

EUMETSAT (2011), EUMETSAT satellites history, Eum/ops/doc/08/4698, EUMETSAT.

Frink, M., Folkman, M. & Darnton, L. (1992), Photodeposition of molecular contaminants with a vacuum ultraviolet solar illumination lamp, *in* 'Proc. of SPIE', Vol. 1754, SPIE, San Diego, CA.

Geogdzhayev, I. V., Mishchenko, M. I., Rossow, W. B., Cairns, B. & Lacis, A. A. (2002), 'Global two-channel AVHRR retrievals of aerosol properties over the ocean for the period of NOAA-9 observations and preliminary retrievals using NOAA-7 and NOAA-11 data', *Journal of the Atmospheric Sciences* **59**, 262–278.

Goldberg, M., Ohring, G., Butler, J., Cao, C., Datla, R., Doelling, D., Gärtner, V., Hewison, T., Iacovazzi, B., Kim, D., Kurino, T., Lafeuille, J., Minnis, P., Renaut, D., Schmetz, J., Tobin, D., Wang, L., Weng, F., Wu, X., Yu, F., Zhang, P. & Zhu, T. (2011), 'The global space-based inter-calibration system', *Bull. Amer. Meteor. Soc.* **92**(4), 467–475.

Govaerts, Y. M. (1999), Exploitation of the Meteosat archive for climate monitoring: Expectations and limitations, *in* 'Proc. 1999 EUMETSAT Meteorological Satellite Data Users' Conf.', EUMETSAT, Copenhagen, Denmark, pp. 255–266.

Govaerts, Y. M., Arriaga, A. & Schmetz, J. (2001), 'Operational vicarious calibration of the MSG/SEVIRI solar channels', *Advances in Space Research* **28**(1), 21–30.

Govaerts, Y. M. & Clerici, M. (2003), 'Evaluation of radiative transfer simulation accuracy over bright desert calibration sites', *Advances in Space Research* **32**(11), 2201–2210.

Govaerts, Y. M., Clerici, M. & Clerbaux, N. (2004), 'Operational calibration of the Meteosat radiometer VIS band', *IEEE Trans. Geosci. Remote Sensing* **42**, 1900–1914.

Govaerts, Y. M. & Lattanzio, A. (2007), 'Retrieval error estimation of surface albedo derived from geostationary large band satellite observations: Application to Meteosat-2 and Meteosat-7 data', *Journal of Geophysical Research: Atmospheres (1984–2012)* **112**, 262–278.

Hansen, J., Sato, M. & Ruedy, R. (1997), 'Radiative forcing and climate response', *Journal of Geophysical Research: Atmospheres (1984–2012)* **102**(6), 6831–6864.

Harries, J. E., Russell, J. E., Hanafin, J. A., Brindley, H., Futyan, J., Rufus, J., Kellock, S., Matthews, G., Wrigley, R., Last, A., Mueller, J., Mossavati, R., Ashmall, J., Sawyer, E., Parker, D., Caldwell, M., Allan, P. M., Smith, A., Bates, M. J., Coan, B., Stewart, B. C., Lepine, D. R., Cornwall, L. A., Corney, D. R., Ricketts, M. J., Drummond, D., Smart, D., Cutler, R., Dewitte, S., Clerbaux, N., Gonzalez, L., Ipe, A., Bertrand, C., Joukoff, A., Crommelynck, D., Nelms, N., Llewellyn-Jones, D. T., Butcher, G., Smith, G. L., Szewczyk, Z. P., Mlynczak, P. E., Slingo, A., Allan, R. P. & Ringer, M. A. (2005), 'The geostationary earth radiation budget project', *Bulletin of the American Meteorological Society* **86**(7), 945–960.

Ipe, A., Clerbaux, N., Bertrand, C., Dewitte, S. & Gonzalez, L. (2003), 'Pixel-scale composite top-of-the-atmosphere clear-sky reflectances for Meteosat-7 visible data', *J. Geophys. Res.* **108**(19), 4612.

Ipe, A., Clerbaux, N., Bertrand, C., Dewitte, S. & Gonzalez, L. (2004), 'Validation and homogenisation of cloud optical depth and cloud fraction retrievals for GERB/SEVIRI scene identification using Meteosat-7 data', *Atmospheric Research* **72**, 17–37.

Key, J. R., Yang, P., Baum, B. A. & Nasiri, S. L. (2002), 'Parameterization of shortwave ice cloud optical properties for various particle habits', *J. Geophys. Res.* **107**, doi:10.1029/2001JD000742.

Knapp, K. R., Ansari, S., Bain, C. L., Bourassa, M. A., Dickinson, M. J., Funk, C., Helms, C. N., Hennon, C. C., Holmes, C. D., Huffman, G. J., Kossin, J. P., Lee, H.-T., Loew, A. & Magnusdottir, G. (2011), 'Globally gridded satellite observations for climate studies', *Bulletin of the American Meteorological Society* **92**(7), 893–907.

Knapp, K. R., Frouin, R., Kondragunta, R. & Prados, A. (2005), 'Toward aerosol optical depth retrievals over land from GOES visible radiances: determining surface reflectance', *International Journal of Remote Sensing* **26**(18), 4097–4116.

Knapp, K. R., Haar, T. H. V. & Kaufman, Y. J. (2002), 'Aerosol optical depth retrieval from GOES-8: Uncertainty study and retrieval validation over South America', *Journal of Geophysical Research: Atmospheres (1984–2012)* **107**(7).

Koepke, P. (1982*a*), 'Calibration of the VIS-channel of Meteosat-2', *Advances in Space Research* **2**(6), 93–96.

Koepke, P. (1982*b*), 'Vicarious satellite calibration in the solar spectral range by means of calculated radiances and its application to Meteosat', *Applied Optics* **21**(15), 2845–2854.

Kondratyev, K. Y. & Galindo, I. (1997), *Volcanic activity and climate*, 1st edn, A. Deepak Publishing, Virginia, VA.

Kriebel, K.-T. & Amann, V. (1993), 'Vicarious calibration of the Meteosat visible channel', *J. Atmos. Oceanic Technol.* **10**(2), 225–232.

Kummerow, C., Barnes, W., Kozu, T., Shiue, J. & Simpson, J. (1998), 'The tropical rainfall measuring mission (TRMM) sensor package', *J. Atmos. Oceanic Technol.* **15**, 809–817.

Kutner, M. H., Nachtsheim, C. J., Neter, J. & Li, W. (2005), *Applied Linear Statistical Models*, Einstein's Legacy, 5th edn, McGraw-Hill, New York, NY.

Lambin, E. F., Geist, H. J. & Lepers, E. (2003), 'Dynamics of land-use and land-cover change in tropical regions', *Annual review of environment and resources* **28**(1), 205–241.

Lambin, E. F., Turner, B. L., Geist, H. J., Agbola, S. B., Angelsen, A., Bruce, J. W., Coomes, O. T., Dirzo, R., Fischer, G., Folke, C., George, P. S., Homewood, K., Imbernon, J., Leemans, R., Li, X., Moran, E. F., Mortimore, M., Ramakrishnan, P. S., Richards, J. F., nes, H. S., Steffen, W., Stone, G. D., Svedin, U., Veldkamp, T. A., Vogel, C. & Xu, J. (2001), 'The causes of land-use and land-cover change: moving beyond the myths', *Global Environmental Change* **11**(4), 261–269.

Li, X. & Gao, S. (2012), *Precipitation Modeling and Quantitative Analysis*, 1st edn, Springer, Netherlands.

Loeb, N. G. & Kato, S. (2002), 'Top-of-atmosphere direct radiative effect of aerosols over the tropical oceans from the clouds and the earth's radiant energy system (CERES) satellite instrument', *Journal of climate* **15**, 1474–1484.

Loeb, N. G., Manalo-Smith, N., Kato, S., Miller, W. F., Gupta, S. K., Minnis, P. & Wieliki, B. A. (2003), 'Angular distribution models for top-of-atmosphere radiative flux estimation from the clouds and the earth's radiant energy system instrument on the tropical rainfall measuring satellite. part i: Methodology', *J. Appl. Meteor.* **42**(2), 240–265.

Loveland, T. R. & Belward, A. S. (1997), 'The IGBP-DIS global 1 km land cover data set, DISCover: first results', *Int. J. Remote Sensing* **18**(15), 3289–3295.

Matthews, G., Priestley, K. J., Spence, P., Cooper, D. & Walikainen, D. (2005), Compensation for spectral darkening of short wave optics occurring on the cloud's and the Earth's radiant energy system, *in* 'Proc. of SPIE', Vol. 5882, SPIE, Bruge, Belgium.

Mayer, B. & Kylling, A. (2005), 'Technical note: The libRadtran software package for radiative transfer calculations - description and examples of use', *Atmos. Chem. Phys. Discuss.* **5**, 1319–1381.

Mei, L., Xue, Y., Wang, Y., Hou, T., Guang, J., Li, Y., Xu, H., Wu, C., He, X., Dong, J. & Chen, Z. (2011), Prior information supported aerosol optical depth retrieval using FY2D data, *in* 'Geoscience and Remote Sensing Symposium (IGARSS)', IEEE, Vancouver, Canada, pp. 2677–2680.

Mishchenko, M. I., Geogdzhayev, I. V., Cairns, B., Rossow, W. B. & Lacis, A. A. (1999), 'Aerosol retrievals over the ocean using channel 1 and 2 AVHRR data: A sensitivity analysis and preliminary results', *Applied Optics* **38**, 7324–7341.

Moulin, C., Lambert, C. E., Poitou, J. & Dulac, F. (1996), 'Long term (1983–1994) calibration of the Meteosat solar (VIS) channel using desert and ocean targets', *Int. J. Remote Sensing* **17**(6), 1183–1200.

Mueller, R., Trentmann, J., Träger-Chatterjee, C., Posselt, R. & Stöckli, R. (2011), 'The role of the effective cloud albedo for climate monitoring and analysis', *Remote Sensing* **3**(11), 2305–2320.

Murat, D., Roca, R., Cracknell, G. & Clavaud, R. (2008), *Climate change & satellites*, 1st edn, Thales Alenia Space, France.

Pagliaro, M., Cirminna, R. & Palmisano, G. (2008), 'Flexible solar cells', *ChemSusChem* **1**, 880–891.

Papayannis, A., Amirdis, V., Mona, L., Tsaknakis, G., Balis, D., Bösenberg, J., Chaikovski, A., Tomasi, F. D., Grigorov, I., Mattis, I., Mitev, V., Müller, D., Nickovic, S., Pérez, C., Pietruczuk, A., Pisani, G., Ravetta, F., Rizi, V., Sicard, M., Trickl, T., Wiegner, M., Gerding, M., Mamouri, R. E., D'Amico, G. & Pappalardo, G. (2008), 'Systematic lidar observations of Saharan dust over Europe in the frame of EARLINET (2000–2002)', *Journal of Geophysical Research: Atmospheres (1984–2012)* **113**(10).

Peltoniemi, J. I., Manninen, T., Suomalainen, J., Hakala, T., Puttonen, E. & Riihelä, A. (2010), 'Land surface albedos computed from BRF measurements with a study of conversion formulae', *Remote Sensing* **2**(8), 1918–1940.

Posselt, R., Müller, R. W., Stöckli, R. & Trentmann, J. (2012), 'Remote sensing of solar surface radiation for climate monitoring – the CM-SAF retrieval in international comparison', *Remote Sensing of Environment* **118**, 186–198.

Powell, M. J. D. (1964), 'An efficient method for finding the minimum of a function of several variables without calculating derivatives', *The Computer Journal* **7**(2), 155–162.

Prospero, J. M. & Carlson, T. N. (1972), 'Vertical and areal distribution of saharan dust over the western equatorial North Atlantic Ocean', *Journal of Geophysical Research* **77**(27), 5255–5265.

Qian, C., Fu, C. & Wu, Z. (2011), 'Changes in the amplitude of the temperature annual cycle in China and their implication for climate change research', *J. Climate* **24**, 5292–5302.

Reuter, M., Thomas, W., Mieruch, S. & Hollmann, R. (2010), 'A method for estimating the sampling error applied to CM-SAF monthly mean cloud fractional cover data retrieved from MSG SEVIRI', *Geoscience and Remote Sensing* **48**(6), 2469–2481.

Ricchiazzi, P., Yang, S., Gautier, C. & Sowle, D. (1998), 'SBDART: A research and teaching software tool for plane-parallel radiative transfer in the earth's atmosphere', *Bull. Amer. Meteor. Soc.* **79**, 2101–2114.

Roebeling, R. A., Feijt, A. J. & Stammes, P. (2006), 'Cloud property retrievals for climate monitoring: Implications of differences between spinning enhanced visible and infrared imager (SEVIRI) on METEOSAT-8 and advanced very high resolution radiometer (AVHRR) on NOAA-17', *Journal of Geophysical Research: Atmospheres (1984–2012)* **111**(D20210).

Schmetz, J., Pili, P., Tjemkes, S., Just, D., Kerkmann, J., Rota, S., ... & Ratier, A. (2002), 'An introduction to Meteosat second generation (MSG)', *Bulletin of the American Meteorological Society* **83**(7), 977–992.

Schulz, J., Thomas, W., Müller, R., Behr, H., Caprion, D., Deneke, H., ... & Werscheck, M. (2009), 'Operational climate monitoring from space: the EUMETSAT satellite application facility on climate monitoring (CM-SAF)', *Atmospheric Chemistry and Physics* **9**(5), 1687–1709.

Snel, R. (2001), In-orbit optical path degradation: GOME experience and SCIAMACHY prediction, *in* 'Proceedings of the ERS-ENVISAT Symposium', Vol. SP-461 (on CD ROM), Nordwijk, The Netherlands.

Staylor, W. F. (1990), 'Degradation rates of the AVHRR visible channel for the NOAA-6, 7, and 9 spacecraft', *Journal of Atmospheric and Oceanic Technology* **7**, 411–423.

Stewart, T. B., Arnold, G. S., Hall, D. F., Marvin, D. C., Hwang, W. C., Owl, R. C. Y. & Marten, H. D. (1990), Photochemical spacecraft self-contamination: Laboratory results and systems impacts, Aerospace report no. tor-0090(5470-01)-3, Chemistry and Physics Laboratory - Laboratory Operations.

Trenberth, K. E., Fasullo, J. T. & Kiehl, J. (2009), 'Earth's global energy budget', *Bulletin of the American Meteorological Society* **90**, 311–323.

Tribble, A. C., Boyadjian, B., Davis, J., Haffner, J. & McCullough, E. (1996), Contamination control engineering design guidelines for the aerospace community, Nasa contractor report 4740, Rockwel International Corporation.

Wagner, S., Govaerts, Y. M., Lattanzio, A. & Watts, P. (2007), Optimal estimation applied to the retrieval of aerosol load using MSG/SEVIRI observations, *in* 'Remote sensing of clouds and the atmosphere XII', SPIE, Florence, Italy.

Wielicki, B. A., Barkstrom, B. R., Harrison, E. F., Lee, R. B., Smith, G. L. & Cooper, J. E. (1996), 'Clouds and the earth's radiant energy system (CERES): An earth observing system experiment', *Bulletin of the American Meteorological Society* **77**(5), 853–868.

WMO (2006), Implementation plan for the global observing system for climate in support of the UNFCC, WMO/TD 1338, WMO.

Xiong, X., Eplee Jr., R. E., Sun, J., F. S. Patt, A. A. & McClain, C. R. (2009), Characterization of MODIS and SeaWiFS solar diffuser on-orbit degradation, *in* 'Proc. of SPIE', Vol. 7452, SPIE, Berlin, Germany.

Yang, J., Gong, P., Fu, R., Zhang, M., Chen, J., Liang, S., Xu, B., Shi, J. & Dickinson, R. (2013), 'The role of satellite remote sensing in climate change studies', *Nature Climate Change* **3**(10), 875–883.

List of publications

Climate monitoring with Earth radiation budget measurements
S. Dewitte, N. Clerbaux, A. Ipe, A. Velazquez, E. Baudrez, S. Nevens, I. Decoster
AIP Conf. Proc. ***1531****, 612; doi: 10.1063/1.4804844 (2012).*

The climate monitoring SAF TOA radiation GERB datasets
N. Clerbaux, E. Baudrez, I. Decoster, S. Dewitte, A. Ipe, S. Nevens, A. Velazquez Blazquez
AIP Conf. Proc. ***1531****, 652; doi: 10.1063/1.4804854 (2012).*

Modeling the aging effects of Meteosat-7 visible band
I. Decoster, N. Clerbaux, E. Baudrez, S. Dewitte, A. Ipe, S. Nevens, A. V. Blazquez, and J. Cornelis
Journal of Atmospheric and Oceanic Technology, ***30(3)****, 496–509 (2013).*

Evidence of pre-launch characterization problem of Meteosat-7 visible spectral response curve
I. Decoster, N. Clerbaux, Y. M. Govaerts, E. Baudrez, S. Dewitte, A. Ipe, S. Nevens, A. V. Blazquez and J. Cornelis
Remote Sensing Letters, ***4(10)****, 1008–1017 (2013).*

Spectral ageing model applied to Meteosat First Generation visible band
I. Decoster, N. Clerbaux, E. Baudrez, S. Dewitte, A. Ipe, S. Nevens, A. V. Blazquez and J. Cornelis
Accepted in the special issue "Calibration and Verification of Remote Sensing Instruments and Observations" in Remote Sensing (2013).